

VIBRATION-INDUCED DROPLET ATOMIZATION
AND DROPWISE CONDENSATION

By

ADAM K. ROBINSON

A THESIS PRESENTED TO THE GRADUATE SCHOOL
OF THE UNIVERSITY OF FLORIDA IN PARTIAL FULFILLMENT
OF THE REQUIREMENTS FOR THE DEGREE OF
MASTER OF SCIENCE

UNIVERSITY OF FLORIDA

2005

Copyright 2005

by

Adam K. Robinson

This document is dedicated to my mother, Lorraine L. Parker.

ACKNOWLEDGMENTS

I thank my advisor, Dr. Jacob N. Chung, without whom the project would not have been possible. I also am grateful to Dr. James Klausner and Dr. William Lear for their input on my committee. Dr. Wei Shyy and Dr. Mark Sheplak gave valuable input in the early stages of the project.

Dr. Louis Cattafesta gave much appreciated advice on data acquisition and signal conditioning. Dr. David W. Hahn gave excellent counsel on modeling heat conduction. Dr. Bojan Vukasinovic, of the Georgia Institute of Technology, graciously granted copyright permission along with copies of some figures from his dissertation on Vibration Induced Droplet Atomization.

Several of my colleagues have given valuable input relating to their experience in different areas of this project including Ryan Avenall, Venkat Chandrasekaran, Quentin Gallas, Ryan Holman, Stephen Horowitz, Landon Tully, Chris Velat, Renqiang Xiong, and Kun Yuan. Their advice undoubtedly saved weeks of effort.

I am very grateful to Ron Brown for his indispensable help and advice in fabrication of the experimental apparatus. Becky Hoover, Pam Simon, and Teresa Mathia provided crucial help and were always pleasant in helping me to navigate administrative requirements.

Several professionals outside of the university system have also been remarkably helpful in completing this project. Pam Bishop, from MTI Instruments, was especially prompt and courteous in helping me to learn about optical position sensing. Richard

Brooks and Jeff Zahnd from American Piezo Corporation provided crucial insights on the function of their piezoelectric products, advice on signal processing, and development samples. Doug Hand from Thales-Optem, Inc. gave excellent advice on optics. John Vickers from Watlow Heating products also gave crucial advice in the early stages of this project.

Finally, but most importantly, I thank my Mother for her years of support.

TABLE OF CONTENTS

	<u>page</u>
ACKNOWLEDGMENTS	iv
LIST OF TABLES	viii
LIST OF FIGURES	ix
LIST OF EQUATIONS	xii
NOMENCLATURE	xiii
ABSTRACT.....	xvi
 CHAPTER	
1 INTRODUCTION	1
2 LITERATURE SURVEY	5
Droplet Ejection.....	5
Filmwise Condensation (FWC).....	10
Dropwise Condensation (DWC).....	11
Main Theory	11
Functional Behavior of Rose Theory	17
Competing Models	27
Droplet Size Distribution.....	33
Effect of Maximum Droplet Size	34
General Results on Drop-wise Condensation (DWC).....	35
Constriction Resistance	38
Drop-wise Condensation (DWC) Promotion	40
Effects of Non-Condensable Gases (NCG).....	44
Heat Transfer with Vibration.....	49
Piezoelectric Droplet Ejection with Heat Transfer	53
3 THEORETICAL ANALYSIS	54
4 APPARATUS	63
Equipment.....	73
Additional Testing	80

5	PROCEDURE.....	84
6	RESULTS AND DISCUSSION.....	88
	Initial Testing.....	88
	Intermediate testing	92
	Final testing	101
	Data Summary and Comparison with Theory	119
	Additional Testing.....	123
7	UNCERTAINTY.....	131
	Main Study.....	131
	Additional Testing.....	133
8	CONCLUSIONS	135
	Main Study.....	135
	Trend Explanation	136
	Additional Testing.....	137
	Improvements	138
	Apparatus.....	138
	Procedure.....	140
APPENDIX		
A	MATLAB CODES	142
	DWC_HTC.m.....	142
	Dropwise_Condensation_Model.m	144
	Theoretical_Heat_Rate_Grid.m.....	146
	DWC_Behavior.m	146
	Get_Theoretical_THR_and_r_eff.m.....	149
	Heat_Rate_Archive.m	150
	PROPS.m.....	159
	exp_profile.m.....	162
	simpsons_rule.m	163
B	TOTAL HEAT RATE TABLES	165
C	DETAIL DRAWINGS	170
	LIST OF REFERENCES.....	178
	BIOGRAPHICAL SKETCH	186

LIST OF TABLES

<u>Table</u>	<u>page</u>
6-1 Experimental and theoretical data for THR.	123
6-2 Data summary from Additional Testing.....	129
7-1 Uncertainty in measured values.	132
B-1 Theotretical THR with theoretical maximum departing droplet size.....	166
B-2 Theotretical THR with 4 mm maximum departing droplet size.	166
B-3 Theotretical THR with 2 mm maximum departing droplet size.	167
B-4 Theotretical THR with 1 mm maximum departing droplet size.	167
B-5 Theotretical THR with 0.5 mm maximum departing droplet size.	168
B-6 Theotretical THR with 0.25 mm maximum departing droplet size.	168
B-7 Theotretical THR with 0.1 mm maximum departing droplet size.	169
B-8 Theotretical THR with 0.01 mm maximum departing droplet size.	169

LIST OF FIGURES

<u>Figure</u>	<u>page</u>
2-1 Dimensionless critical acceleration vs. dimensionless drop diameter	7
2-2 Droplet atomization by frequency modulation.....	8
2-3 Heat transfer coefficient vs. saturation temperature.....	18
2-4 Heat transfer coefficient vs. subcooling.....	19
2-5 Heat flux vs. saturation temperature	20
2-6 Heat flux vs. subcooling.....	21
2-7 Heat transfer coefficient vs. maximum departing droplet radius for $T_{\text{sat}} = 380\text{K}$	22
2-8 Heat transfer coefficient vs. maximum departing droplet radius	23
2-9 Heat transfer coefficient vs. maximum departing droplet radius for $T_{\text{sat}} = 280\text{K}$	24
2-10 Heat flux vs. maximum departing droplet radius for $T_{\text{sat}} = 380\text{K}$	24
2-11 Heat flux vs. maximum departing droplet radius at $\Delta T = 1\text{K}$	25
2-12 Heat flux vs. maximum departing droplet radius for extreme parameters.....	26
2-13 Smallest thermodynamically viable droplet radius vs. T_{sat}	27
3-1 Assumed radial surface temperature distribution.....	56
3-2 Radial HTC and HF distributions.....	57
3-3 Block diagram of iterative loop to determine theoretical THR.....	59
3-4 Theoretical THR vs. maximum droplet radius.....	62
4-1 Corner view of experimental apparatus.	66
4-2 Sectioned view of experimental apparatus.....	67
4-3 Insulation applied to and removed from diaphragm frame	68

4-4	Exploded view of experimental apparatus.	69
4-5	Diaphragm clamp, lower face	70
4-6	Schematic of equipment setup with labels	75
4-7	Schematic of vacuum apparatus adjustments for Additional Testing.	81
4-8	Placement of surface thermocouples on the piezoelectric diaphragm	82
6-1	Video frames of DWC without (left) and with (right) VIDA	89
6-2	Temperature data from 1/26	89
6-3	Total heat rate data from 1/26	90
6-4	Temperature data from 2/17	92
6-5	Total heat rate data from 2/17	94
6-6	Two frames taken from videos on 2/17	95
6-7	Temperature data from 2/24	97
6-8	Total heat rate data from 2/24	99
6-9	Typical droplet distribution for DWC on the test diaphragm without VIDA	100
6-10	Video frames of typical droplet distribution for DWC with VIDA	100
6-11	Temperature data from 3/4	102
6-12	Total heat rate data from 3/4	103
6-13	Temperature data from 3/13	104
6-14	Total heat rate data from 3/13	105
6-15	Temperature data from 3/14	106
6-16	Total heat rate data from 3/14	107
6-17	Temperature data from 3/15-16	108
6-18	Total heat rate data from 3/15-16	109
6-19	Droplet departure and regeneration in DWC without VIDA, 3/15-16.	110
6-20	Video frames of VIDA onset, front view.	113

6-21	Calibration curve for peak-to-peak displacement vs. input voltage.....	115
6-22	Peak-to-peak displacement vs. frequency for used driver.....	116
6-23	Video frames of VIDA process, corner view	118
6-24	Experimental THR vs. theoretical THR	120
6-25	Total heat rate vs. maximum subcooling	122
6-26	Temperature data from 5/21	124
6-27	Comparison of 5/21 surface temperature data.....	127
6-28	Comparison of 5/21 VIDA and non-VIDA temperature data for shim surface	128
C-1	Bottom Cover detail drawing.	171
C-2	Cooler Barrel detail drawing.	172
C-3	Diaphragm Clamp detail drawing.	173
C-4	Diaphragm Frame detail drawing.....	174
C-5	Optical Probe Guide detail drawing.....	175
C-6	Optical Probe Seal detail drawing.....	176
C-7	Top Cover detail drawing.....	177

LIST OF EQUATIONS

<u>Equation</u>	<u>page</u>
2-1 Nusselt correlation for FWC on a vertical flat plate	10
2-2 Modified heat of vaporization for Nusselt correlation.....	10
2-3 Thermal resistance in a droplet due to conduction	13
2-4 Thermal resistance in a droplet due to interphase matter transfer resistance	14
2-5 Finite temperature drop required for equilibrium	14
2-6 Heat flux through a drop	14
2-7 Fraction of condenser surface area covered by drops larger than r	15
2-8 General expression for fractional area coverage of condenser surface.....	15
2-9 Specific expression for fractional area coverage of condenser surface	15
2-10 Average heat flux over an isothermal surface undergoing DWC (Rose Theory)..	16
2-11 Maximum departing droplet radius.....	16
2-12 Minimum thermodynamically viable droplet radius.....	16
2-13 Empirical relation for DWC.....	16
2-14 Interfacial mass transfer resistance	27
2-15 Theoretical HTC accounting for constriction resistance	28
3-1 Heat conduction equation in cylindrical coordinates.....	55
3-2 Assumed exponential form of radial temperature distribution	56
6-1 Energy equation	91

NOMENCLATURE

A	area
B	a constant
C	a constant
$c_{P,f}$	mass specific heat of fluid state
dr	differential radius
E	energy
\dot{E}	time rate of energy change
f	fraction of condenser surface coverage
g	acceleration of gravity
h	convection coefficient
h_{fg}	heat of vaporization
K	a constant
k	thermal conductivity
L	characteristic length
n	droplet size distribution exponent
q''	heat flux
R	gas constant
R''	thermal resistance
r	droplet radius
\hat{r}	maximum departing droplet radius

\tilde{r}	smallest thermodynamically viable droplet radius
T	temperature
t	temperature in Celsius

Greek Letters

ΔT	difference between saturation and condenser surface temperatures
Δt	change in time
ρ	density
γ	specific heat ratio
σ	surface tension
μ	absolute viscosity
ν	kinematic viscosity
π	pi

Subscripts

avg	average
CV	control volume
$cond$	conduction
f	fluid
g	gas
gen	generation
in	in
L	length
$mattertransfer$	interphase matter transfer
out	out
s	surface (condenser)

sat

saturation

Operators

∂

partial differential

Abstract of Thesis Presented to the Graduate School
of the University of Florida in Partial Fulfillment of the
Requirements for the Degree of Master of Science

VIBRATION-INDUCED DROPLET ATOMIZATION
AND DROPWISE CONDENSATION

By

Adam K. Robinson

December 2005

Chair: Jacob N. Chung

Major Department: Mechanical and Aerospace Engineering

This thesis studied the process of dropwise condensation (DWC) of water vapor on a non-isothermal condenser surface. Specifically, the object was to quantify the effects of Vibration Induced Droplet Atomization (VIDA) on this process. The working fluid was water vapor in the saturation temperature range from 24 to 48°C (75 to 118°F), corresponding to 3.0 to 11.2 kPa (0.89 to 3.30 in-Hg). The condenser surface was the clean metal side of a brass shim, of 19 mm (0.75 in) diameter and 0.4 mm (0.016 in) thickness. A piezoelectric ceramic disk was attached to the other side of this shim. The resonance frequency of this arrangement in a clamped edge boundary condition ranged from 2.1 to 4.0 kHz with the temperature of the disc. The driving voltage signal was a sinusoidal wave form of about 35 Vp-p.

Theoretically, any reduction in the maximum aggregate size reached by the drops of condensate should result in an increase in the heat transfer coefficient, or HTC. If vibration was applied to a sessile droplet in a certain range of frequency and amplitude,

the droplet surface developed capillary waves. Given enough intensity of vibration, these waves outstretched the viscous forces holding the drop together and the drop disintegrated into hundreds of small drops. These small drops then moved away from the original, static drop surface at roughly perpendicular trajectories.

Direct case-by-case comparison of the effects of VIDA on DWC was not possible. The control model assumed an exponential radial temperature distribution in the diaphragm. Direct surface temperature measurements of the diaphragm during application of vibration indicated that the assumed profile did not apply. The area above the piezoelectric patch on the back of the diaphragm was found to have a higher temperature than the saturated vapor. Therefore the active heat transfer area of the VIDA case was smaller than that of the non-VIDA case. However, the acceptable data points from the former set still showed comparable to improved overall HT rates over the latter. Therefore some advantage was shown, but it could not be quantified.

Maximum peak-to-peak displacement of the diaphragm was as high as 40 μm for a new driver, while for an old driver may have been about 10 μm . Edge temperature readings for the shim ranged from 6 to 19°C (43 to 66°F) with coolant inlet temperatures near 4°C (40°F). The bulk of the original data showed much lower than predicted overall heat transfer rates, or THR. This was due to the extreme sensitivity of low pressure DWC to the presence of non-condensable gases, or NCG, namely air. A final round of testing was able to clear up this problem enough to clearly examine VIDA effects on DWC.

CHAPTER 1 INTRODUCTION

Heat dissipation has been a major barrier to increases in processor speed and decreases in length scale of electronic devices. The Semiconductor Industry Association report of 2001 [1] projected cooling loads that would be necessary in the near future for new generations of electronic devices. At the time of their study, 40 W/cm^2 was given as a typical required heat flux (HF) for the high performance electronics category, which included for example military avionics. This cooling requirement, projected to the year 2016, more than doubled to 93 W/cm^2 .

The difficult aspect of dissipating this level of heat flux for cooling electronic devices was that it had to be accomplished over a relatively small temperature difference, since the maximum temperature of the electronic devices must stay safely below 85°C , the melting point of the silicon substrate, which leaves at most only about a 40 to 50°C window between the temperature of the heat source to the ambient atmosphere.

Mudawar, in 2001 [2], examined strategies for dissipating high heat fluxes. He compared the reported heat transfer coefficients (HTC) for the three most common coolant fluids from literature, air, water, and fluorochemical liquids. The three heat transfer (HT) regimes examined were natural convection, single-phase forced convection, and pool boiling. The former two methods are currently the most common and easily implemented methods of electronics cooling. However, only the latter method was capable of reaching the needed 100 W/cm^2 over a temperature difference on the order of

10°C. However, boiling presents a problem in steady cooling due to temperature shocks that accompany the formation and departure of vapor bubbles.

Significantly higher HTC's were reported for more involved cooling scenarios such as forced convection boiling, spray, and jet cooling, however these methods also added significant complexity, weight, and reliability issues to the overall design of a given device. Still, the main conclusion of the paper was that a two phase cooling solution was the most likely choice for higher levels of heat dissipation, but that this would likely add significant complexity to the devices. Thus a problem has emerged of how to integrate a two-phase, high heat flux cooling scheme into electronic devices of ever decreasing length scale, while not greatly increasing the complexity.

Francois, Shyy, and Chung, in 2000 [3], offered a potential solution for such a two phase cooling device. They proposed a theoretical model of a MEMS (micro-electro-mechanical-systems) device, completing a vapor compression cooling cycle with a fluorinert chemical as the working fluid. The proposed system was to be driven by a piezoelectric diaphragm that would also act as the condensing surface. This would allow for surface tension control of the drops of condensate. This step was taken so that the device would not be gravity dependent. This analysis presumed dropwise condensation (DWC) on the diaphragm surface, which has been shown to offer HTC an order of magnitude higher than filmwise condensation (FWC). The relationship between maximum droplet size and HTC for DWC will be explicitly examined after the introduction of the theory. Since the length scale of this device was very small, the droplets involved were also very small and therefore very high HF was anticipated.

In Francois, 2002 [4], a numerical simulation looked in detail at the droplet impact on a heated wall and HT aspects of the evaporative side of the proposed device.

However, analysis of the condensation side of the cell was left as an assumption that DWC would offer a certain order of magnitude of HF. Detailed consideration of this process was left for further studies.

This model assumed bulk ejection of the condensate droplet from the membrane, a significant obstacle considering the increasing dominance of surface tension over body force with a decrease in length scale, although an energy balance model was offered for the energy required for ejection. Friedman and Chung, in 2001 [5], made an initial investigation into the droplet ejection process. The device used was in the meso-length scale since the piezoelectric driver had about a $\frac{3}{4}$ inch diameter. The prefix meso refers to a characteristic length scale in the range of 1 mm to 1 m. Primary droplet volumes investigated ranged from 1 to 5 μL . Even at this relatively large scale of 30 to 150 times the volume of the largest drop considered in the current study, they still encountered significant difficulty achieving droplet detachment from the diaphragm surface. When detachment was achieved, most often the primary droplet divided into several smaller drops. The difficulty in drop detachment was due to the high surface tension forces with respect to the momentum forces of the fluid mass. It was because of these surface tension related problems that good repeatability was not attained. Thus, further work was needed to determine an appropriate method of droplet ejection from a piezoelectric membrane surface.

This project was undertaken to study the process of condensation and subsequent droplet ejection of coolant vapor on a vibrating piezoelectric disk. This effort was

needed to clear up the cooling side of the device proposed in [3]. The following criteria were set as goals for the development of the investigation:

- Meso length scale for ease of study.
- Dropwise Condensation mode for its expected high HF.
- Water as the working fluid for its high heat of vaporization. However, this would necessitate sub-atmospheric working pressures in order to lower the saturation temperature below 85°C.
- Piezoelectric disc for both the droplet ejection mechanism and condensing surface.
- Some form of droplet ejection would be used to remove condensate

CHAPTER 2 LITERATURE SURVEY

Droplet Ejection

A literature search for droplet ejection methods involving piezoelectric devices yielded several potential methods. Percin et al., in 1997 [6], tested a piezoelectric droplet ejector. The piezoelectric diaphragm had a small hole at the center, 50 to 100 μm in diameter. It supported a reservoir of liquid. The hole was small enough that the surface tension of the liquid across the hole kept it from leaking out. Droplet ejection occurred when the oscillation frequency and amplitude caused the momentum of the fluid to overcome the surface tension. Flow rates of up to 100 mL/s and ejection frequencies of up to 32 kHz were cited. The device was roughly 8 mm in diameter, 8 mm in length, and operated on a 32 Vp-p sinusoidal voltage. The working fluid was a special, low-viscosity ink. Higher viscosity fluids were tested, requiring voltages up to 200 Vp-p. This design was promising for the purposes of this study, except that the orientation of the liquid surface had to be away from the direction of ejection, not leaving much surface area available for removing the heat that would induce condensation on the liquid surface.

Zhu and Kim, in 1998 [7], reported a MEMS device which achieved significant fluid mixing using loosely focused acoustic waves from a piezoelectric diaphragm. The diaphragm bore ceramic patches arranged specifically to accomplish the focusing by constructive interference. The focal length was designed to be just above the liquid/vapor interface. The device was small enough, 1.5 x 1.5 x 0.5 mm, that the top could be open and still be insensitive to gravity effects because of the surface tension. The authors

reported negligible heating of the fluid from driver operation. This device showed much promise for fluid motivation on a micro-scale but lacked the droplet ejection required for the present device.

In 2001, Huang and Kim [8] used a similar arrangement to [7] to achieve droplet ejection. Moving the surface of the fluid a little higher, to coincide with the focal point of the acoustic waves, was the main difference between the two devices. These waves were again created by a specially patterned piezoelectric ceramic. The ejected droplet velocity, caused by constructive interference, was found to be between 2 and 3 m/s, with operating frequencies up to 10 kHz. Droplet diameter was reportedly around a few microns with uniform size and direction. The device was less than 2 mm in diameter and 0.5 mm in length. The ejection characteristics and the length scale of this device appear well suited for the needs of the proposed HT cell. The limitation here was the conduction resistance of the fluid bulk. At this point, it was assumed that DWC would provide more intense cooling than could be achieved by direct contact condensation, due to the relatively slow conduction of heat through the liquid phase.

Szita et al., in 2001 [9], reported the development of a micropipettor, using the capacitance of one piezoelectric disc for feedback information to very precisely control the dispensed volume and another disc for pumping force. Volume control was in the sub- μL range. This design however, lacked the sufficient velocity of ejected droplets desired for the current application. This velocity was required to break through a vapor layer on the hot surface of the proposed HT cell.

The most promising method of droplet ejection that came up in the literature search was Vibration Induced Droplet Atomization (VIDA) [10]. A horizontal piezoelectric disc

with diameter on the order of 1 inch was used as the supporting base for a single drop of water placed at its center. As the perpendicular vibration of the diaphragm approached resonance, standing waves developed on the surface of the sessile droplet. A critical acceleration and frequency existed for a given drop of fluid, above which the momentum of the fluid in these standing waves overcame the surface tension. This caused the droplet to effectively burst. The order of the critical acceleration was given as roughly 20 times standard-earth gravity. The length of time of the bursting event ranged from

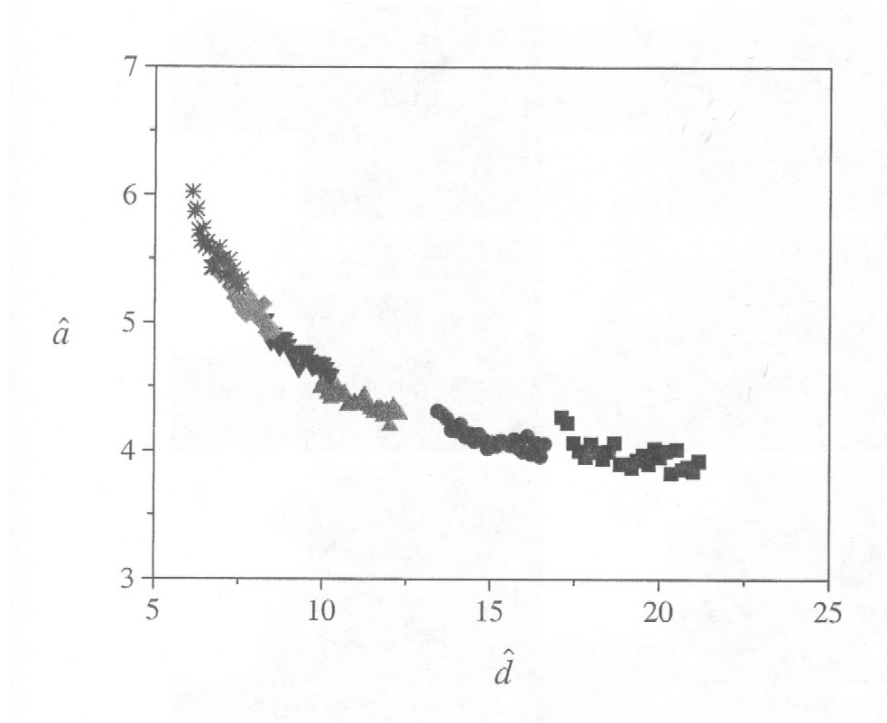


Figure 2-1. Dimensionless critical acceleration vs. dimensionless drop diameter.

Acceleration was determined by $\hat{a} = af^{4/3}/(\sigma/\rho)^{1/3}$ and diameter by $\hat{d} = df^{2/3}/(\sigma/\rho)^{1/3}$. Used with permission from [10].

essentially instantaneous for a large step input change in either amplitude or frequency to up to a minute for small changes in these parameters. Excellent correlation was found for the dimensionless critical acceleration versus dimensionless drop diameter involving the fluid properties and the frequency of oscillation (Figure 2-1).

Note the inverse exponential manner in which the dimensionless critical acceleration required for atomization increases as the droplet diameter decreases. This implies an effective lower size limit for achievable atomization events. Primary droplet diameters used in this study ranged from 10 to 150 μL while the resonant frequencies of the drivers used were 1, 3, 5, 7, 9, and 15 kHz. Generally the larger the diameter or the thickness of the piezoelectric disc driver, the lower the resonant frequency.

When the amplitude of the input signal to the drive was fixed and the frequency incrementally increased from 0 towards resonance, the atomization process had roughly three steps (Figure 2-2). When vibrations commenced at low frequency, standing lateral

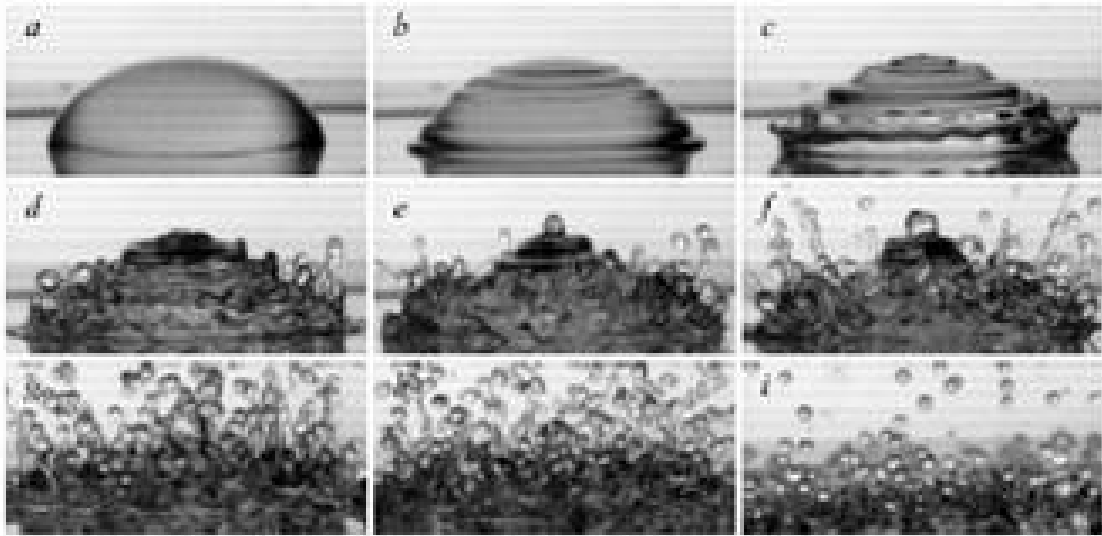


Figure 2-2. Droplet atomization by frequency modulation, 0.1 mL drop. Used with permission from [10]. a) No applied acceleration. b) Lateral standing waves develop on drop surface. c) Lateral standing waves grow in amplitude. d) Axial waves become visible over lateral waves, creating a cross-hatch pattern. Wave momentum begins to overcome surface tension, as drops begin to issue from the outer wave peaks. e) Amplitude of oscillations grows, more drops issue from primary drop. f) Drop ejections increase in number and intensity. g) Primary drop no longer visible due to number of secondary drop ejections. h) Ejections of secondary drops continue. i) Primary drop mostly dissipated and secondary droplet ejection complete.

waves appeared around the circumference of the sessile droplet. As the frequency approached the resonant frequency of the driver-drop system, axial waves also appeared, making a cross-hatched pattern with the lateral waves. As input frequency came closer still to resonance, the peak of the wave oscillations began to overcome the surface tension forces keeping the primary drop intact, causing secondary drops to pinch-off from the wave peaks. Near the resonant frequency and still with fixed amplitude of the input signal to the driver, the pinching-off of secondary droplets became much more intense. As this process progressed, the primary drop became depleted until there was only a small fraction of it left.

The diameter of the ejected droplets was reported to be relatively independent of both the time during the atomization event and the volume of the primary droplet. The ejected velocity was said to range from 0.2 to 2.0 m/s. The droplet velocity was measured by a particle tracking velocimetry algorithm, developed by the investigator, and digital video images. A peak in ejection velocity was found at the onset of atomization. This quantity then decreased to be roughly equivalent to the velocity of the resonating diaphragm, just below the point of issuance.

The trajectory of the ejected droplets was roughly perpendicular to the surface of the undisturbed primary drop at the given location, and, on average, was axisymmetric. Viscosity and surface tension were also slightly varied to probe for an effect on the atomization process, though no major quantitative change was found.

On the operation of the piezoelectric diaphragms, Vukasinovic [10] noted that the resonance frequency was extremely sensitive to temperature as well as mass loading of

the diaphragm, both of which would no doubt be important considerations in any application of VIDA to DWC.

Filmwise Condensation (FWC)

Filmwise condensation is the default mode of condensation and has therefore been taken as the design assumption in industrial design. Filmwise condensation will indicate the failure of the DWC mode, due to several possible factors including contamination of the vapor, contamination of the condenser surface, too large of a contact angle for the working fluid with the condenser surface, or too high HF leading to flooding of the condenser surface.

Nusselt provided the most successful correlations for FWC on a vertical flat plate in a pure vapor (Eq. 2-1) [11]. This correlation used a modified heat of vaporization, which accounted for subcooling of the condenser surface (Eq. 2-2) [11].

$$Nu_{L_{avg}} = \frac{h_L L}{k_f} = 0.943 \left[\frac{\rho_f g (\rho_f - \rho_g) h'_{fg} L^3}{\mu_f k_f (T_{sat} - T_s)} \right], \quad 2-1$$

$$h'_{fg} = h_{fg} + 0.68 c_{p,f} (T_{sat} - T_s), \quad 2-2$$

In this Nusselt correlation, h is the HTC, L is the length of the plate, g is the acceleration of gravity, ρ is density, μ is the dynamic viscosity, k is the thermal conductivity, T is temperature, and c_p is the constant pressure mass specific heat of the condensate. The subscript f denotes fluid, sat is for saturated, s is for surface, and g is for gas. One of the seminal investigators of DWC, Dr. John Rose, commented on the remarkable accuracy of the Nusselt theory for FWC in an address on developments in condensation theory, in 1988 [12]. He said that further tweaking of this Nusselt relation

for FWC was essentially “an academic exercise,” since this theory was correct to within a few percent for most cases.

Dropwise Condensation (DWC)

For decades now, researchers have sought to master the process of DWC. The high HF values attainable with this mode of condensation offered attractive potential increases in efficiency for industrial HT processes. However, this phenomenon has proven quite resistant to efforts at precise characterization. The main performance difference in DWC and FWC is generally accepted as a potential order of magnitude increase in HTC. This holds possibly dramatic cost savings in many applications including power plants that run steam turbines as well as seawater desalination plants. These cost savings would exist specifically in terms of lower capital and maintenance costs for a given output capacity.

Main Theory

Early investigations, however, showed widely ranging trends of relationship of heat flux (HF) to degree of subcooling of the condenser surface, $T_{\text{sat}} - T_s = \Delta T$. This variation in reported results was so significant that, the first authors to offer a viable theory on DWC HT, said they were, “of very little use even as a check,” [13]. These investigators asserted that the massive variance in the reported trends in DWC HT as due to the presence of non-condensable gases (NCG) in the test vapor. In most cases, this non-condensable species was air. To prove this theory, these authors chose to study DWC of steam near 1 atm. They used an isothermal copper block as a condensing surface and a heat flux meter. Some of the main efforts undertaken to control the influence of NCG on the experimental results were as follows:

- Careful attention was paid to the vacuum integrity of the apparatus.

- Long blow-off periods were employed prior to taking data, usually 3-4 hours, to allow sufficient degassing of the supply water and of the walls of the stainless steel apparatus. For these periods the boilers ran at full power and the vessel was vented to atmosphere in a controlled manner, to prevent backflow.
- A small vent tube was placed near the condenser surface. Different rates of steam venting were tested for effect on temperature changes of the condensing surface and also for visual disturbance of the condensate. A venting rate was then chosen based on a balance between these competing considerations.
- The authors also took extreme care to minimize uncertainty in temperature measurement, which they had also noted as a major source of error in previously published studies. Several temperature measurements were taken along the centerline of a copper block to determine the heat flux and then the gradient extrapolated to the condensing surface. A summary of their key findings follows:
- NCG had the significant effect of depressing the surface temperature for a given HF and saturation temperature, in other words, increasing ΔT .
- Significant difference was noted in effectiveness of the four promoters used, though the underlying surface of polished copper and the cleaning regimen remained constant.
- No dependence of HF on plate height was found. This quantity was measured 1 inch and 4 inch from the top of the test surface with no discernable difference in the data.
- Sweeping frequency and maximum drop size did not affect HTC in the range studied.

The first finding helped cement the notion that NCG had an important effect on condensation HT. The second became important later in the debate over the effect of surface thermal conductivity on overall HT in DWC, which will be discussed at length in the Constriction Resistance section of the literature survey. The third finding of no height dependence has also been contentious, as several other researchers have noted a height dependence, for example, Koch, Kraft, and Leipertz, in 1998 [14] and in the much more extreme cases studied by Yamali and Merte, 1999 and 2000 [15,16]. There were several contemporary studies of Le Fevre and Rose that found similar magnitude HF, and these will be discussed further in the General Trends section below. For now, consider

the theory offered by the same pair of researchers the following year, Le Fevre and Rose, 1966 [17]. The theory has been republished numerous times, though in its most compact form in Rose, 1988 [12]. Some corrections and coefficient values were suggested in a 2002 presentation [18].

The Rose theory, as it will henceforth be referred to, was based on the assumption that all the HT in DWC effectively occurred on the surface of the liquid droplets rather than the bare condenser surface between drops. The theory assumed only three significant thermal resistances, with each represented by a temperature difference. The first was conduction through the liquid of the sessile droplet. The second was interfacial matter transfer resistance. The third assumed-significant thermal resistance in DWC was the finite decrease in saturation temperature required for equilibrium of a saturated vapor with the curved surface of a liquid drop. From these resistances, an expression was derived for the HF through a given drop of radius r . This expression for HF, based on fluid-vapor properties and drop radius, was then weighted by an assumed distribution of drop sizes. The weighted HF was then integrated over a range of drop sizes from the minimum thermodynamically viable drop radius to the maximum. The maximum drop radius was determined from dimensional analysis and experiment.

The thermal resistance due to heat conduction through the drop was calculated by neglecting internal circulation or convection (Eq. 2-3). K_1 is a shape factor for the ratio of surface areas between the base and the top of a hemispherical drop. r is a given drop radius. k_f is the thermal conductivity of the condensate.

$$R''_{cond} = K_1 \frac{r}{k_f}, \quad 2-3$$

The expression for interfacial matter transfer resistance was calculated as a thermodynamic function (Eq. 2-4). K_2 is a constant, experimentally determined and relatively constant for different fluids. ν_g is the kinematic viscosity. T is the saturation temperature of the vapor. R is the gas constant of the vapor. γ is the specific heat ratio of the vapor. h_{fg} is the heat of vaporization of the working fluid.

$$R''_{mattertransfer} = K_2 \frac{\nu_g T}{h_{fg}^2} \left(\frac{RT}{2\pi} \right)^{\frac{1}{2}} \left(\frac{\gamma + 1}{\gamma - 1} \right), \quad 2-4$$

Finite temperature drop associate with a saturated liquid and vapor in equilibrium at the curved surface of a drop was also a thermodynamically derived quantity (Eq. 2-5). σ is the surface tension of the fluid.

$$\Delta T_{curve} = \frac{2\sigma T_{sat}}{r\rho_f h_{fg}}, \quad 2-5$$

The thermal resistances in (Eq. 2-3,4,5) were then combined with the temperature difference between the condenser surface and the saturated vapor to form an expression for the HF through a single drop of radius r (Eq. 2-6). The correction factor in the interphase matter transfer resistance term was offered as a correction for the polyatomicity of water.

$$q''(r) = \frac{\Delta T - \frac{2\sigma T_{sat}}{r\rho_f h_{fg}}}{\frac{K_1 r}{kT} + K_2 \left(\frac{0.627}{0.664} \right) \frac{T_{sat}}{\rho_g h_{fg}^2} \left(\frac{\gamma + 1}{\gamma - 1} \right) \left(\frac{RT}{2\pi} \right)^{1/2}}, \quad 2-6$$

Now a statistical distribution for drop sizes, and limits on those sizes had to be chosen in order to integrate over all drop sizes to obtain the total HF for the surface. Le Fevre and Rose chose the distribution in (Eq. 2-7), based on an expression for the fraction

of the condenser surface that was covered by drops larger than r . This fraction went to 1 as the given radius went to zero and went to 0 as r went to the maximum radius, r_{\max} . In other words, all of the surface was covered by drops larger than zero, and none of the surface was covered by drops larger than r_{\max} . When differentiated with respect to r , (Eq. 2-7) gives the area covered by a differential drop radius, dr (Eq. 2-8).

$$f = 1 - \left(\frac{r}{\hat{r}} \right)^n, \quad 2-7$$

$$A(r)dr = n \left(\frac{r}{\hat{r}} \right)^{n-1} \frac{dr}{\hat{r}}, \quad 2-8$$

For the original theory, Le Fevere and Rose assumed from observations that n was roughly equal to $1/3$, an assumption that was later vitiated by the results of Rose and Glicksman, in 1973 [19]. There has been much discussion of this topic in the literature which will be addressed later in this paper. With $n = 1/3$, (Eq. 2-8) gave (Eq. 2-9).

$$A(r)dr = \frac{1}{3} \left(\frac{r}{\hat{r}} \right)^{-2/3} \frac{dr}{\hat{r}}, \quad 2-9$$

It should be noted that this equation gave an exponent of $-2/3$ as opposed to the $-1/3$ given in [12]. This was decided a typo in the original, since the derivative of (Eq. 2-7) with respect to r , yields the (Eq. 2-9) as given and the expression given for the q''_{avg} in the same reference follows from the value of the exponent used in (Eq. 2-9), which was arrived at when equation (Eq. 2-6) was multiplied by the differential area (Eq. 2-9) and integrated from the minimum to the maximum drop radius. The result was the HF for the entire condensing surface, averaged over all drop radii from the minimum to the maximum (Eq. 2-10). The maximum droplet radius was determined by dimensional analysis in (Eq. 2-11) [12]. Here K_3 is an empirical constant. The minimum

thermodynamically viable droplet radius was given, finally in a dimensionally correct form, in (Eq. 2-12) [20]. Note: some of the notation above and throughout this paper has been changed to be homogenous with that of this study, but the meaning has been retained. In the same reference, [20], Rose offered an empirical relation for DWC of steam “near and below atmospheric pressure” (Eq. 2-13).

$$q''_{avg} = \frac{1}{3\hat{r}^{2/3}} \int_{\tilde{r}}^{\hat{r}} \left(\frac{\Delta T - \frac{2\sigma T_{sat}}{r\rho_f h_{fg}}}{K_1 \frac{r}{k} + K_2 \frac{T_{sat}}{\rho_f h_{fg}^2} \left(\frac{\gamma+1}{\gamma-1} \right) \left(\frac{RT_{sat}}{2\pi} \right)^{1/2}} \right) r^{-2/3} dr, \quad 2-10$$

$$\hat{r} = r_{max} = K_3 \left(\frac{\sigma}{\rho g} \right)^{1/2}, \quad 2-11$$

$$\tilde{r} = r_{min} = \frac{2\sigma \nu_f T}{h_{fg} \Delta T}, \quad 2-12$$

$$q'' = t^{0.8} [5\Delta T + 0.3\Delta T^2], \quad 2-13$$

In (Eq. 2-13) q'' is in kW/m² and t and ΔT in °C. No uncertainty was explicitly stated. However, the presented data were claimed to be ‘quite well represented’ by the given relation. A graphical estimation of the quality of this representation gave an uncertainty of $\pm 10\%$. Likewise, no explicit statement of uncertainty for (Eq. 2-10) was given. This was most likely due to the myriad of factors that could potentially yet be proven to be of import to the phenomenon of DWC. A brief listing of these factors follows here, each of which was furthered explored in this literature survey:

- General comments on DWC trends in ΔT , T_{sat} , and r_{max}
- Drop size and Nucleation site density
- Effect of maximum droplet size on overall HF
- Constriction resistance debate
- Promotion methods

- Condensation coefficient, as it affects the interfacial mass transfer resistance term
- Effects of NCG on both DWC and FWC

Functional Behavior of Rose Theory

One main advantage of the Rose theory was that it presented a closed-form relation for HF and surface temperature in a compact form. Most of the competing theories, which will be discussed in the next section, are presented only as numerical simulations, which can be enlightening but also daunting to implement. The following figures examine the behavior of the mathematical function of the Rose theory, specifically in the ranges of parameters relevant to this study, slightly extended to cover most applications of DWC of water vapor.

Mathematical function was emphasized in this section, and therefore only small effort was made to confirm the achievability of the extreme values presented. That is, no consideration for transition to FWC or the existence of corresponding experimental values, as these concepts were addressed in the General Results section. In fact, only the more moderate ranges of saturation temperature and maximum droplet size will be used in this study, for comparison to experimental data. In the many journal presentations of his theory, Rose had yet to offer a quantifiable maximum error for his theory, merely saying often that good or general agreement existed with available experimental data that he considered reliable, as in Stylianou and Rose, 1980 & 1983, and Rose, 1981 [21,22,23], or simply presenting a figure of the theory graphed over the experimental results of several investigations and offering no explicit comment on uncertainty, as in Rose, 1998 & 2002 [24,18]. The farthest Rose has thus far ventured in explicit comments on the accuracy of his theory was in [12], where he noted excellent agreement of data and theory for 380 data points from 5 different investigations of DWC. These 5 different

studies used 8 different promoters on copper and steam near 1 atm. In that figure, the apparent maximum deviation was roughly +1K (30%), in a graph of ΔT vs. HF. The variation appeared well centered about the theory line. This ΔT vs. HF relation has been his preferred method for examination of DWC performance. This choice was due to the large uncertainty in measuring the condensing surface temperature and the consequently much larger uncertainty in HTC since it involves the reciprocal of this quantity.

Additionally, the choice of HF as the independent and the surface subcooling as the dependent variable more accurately represents the experimental circumstances. This topic will be addressed in more detail in the General Trends section. Of particular importance for the following figures was that the theory concerns only an isothermal surface while the current study involves only a condenser surface with a variant temperature distribution over its surface.

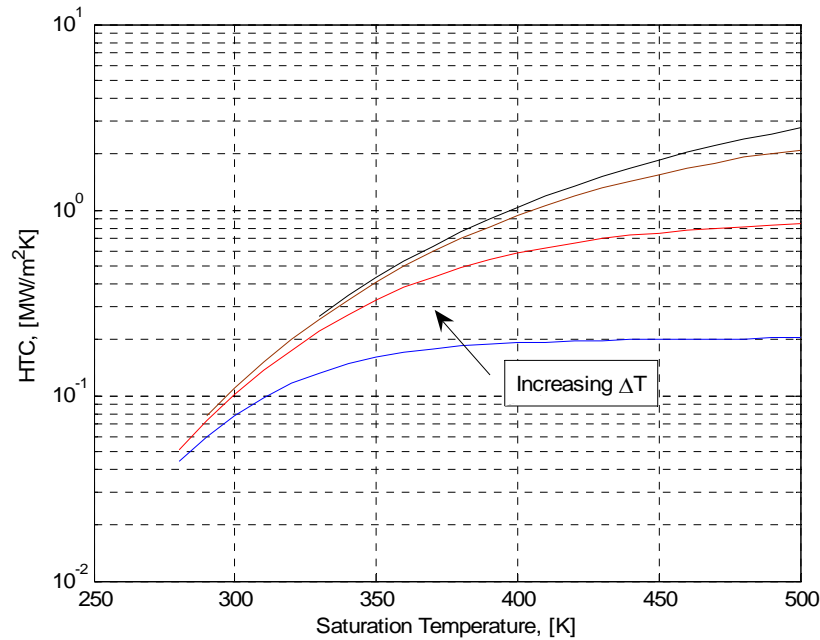


Figure 2-3. Heat transfer coefficient vs. saturation temperature, T_{sat} , for subcooling, $\Delta T = 0.1, 1.0, 10, 50$.

The HTC determined from the Rose theory was somewhat flat relative to increasing saturation temperature and for small surface subcooling (Figure 2-3). However, as surface subcooling increased, the HTC predicted from 300 to 500°C saturation temperature experienced almost a two order-of-magnitude increase. Note that the effects of subcooling are increasingly mitigated for lower vapor pressures/temperatures. Also, as subcooling increases for a given saturation temperature, successive increases in HTC diminish in magnitude.

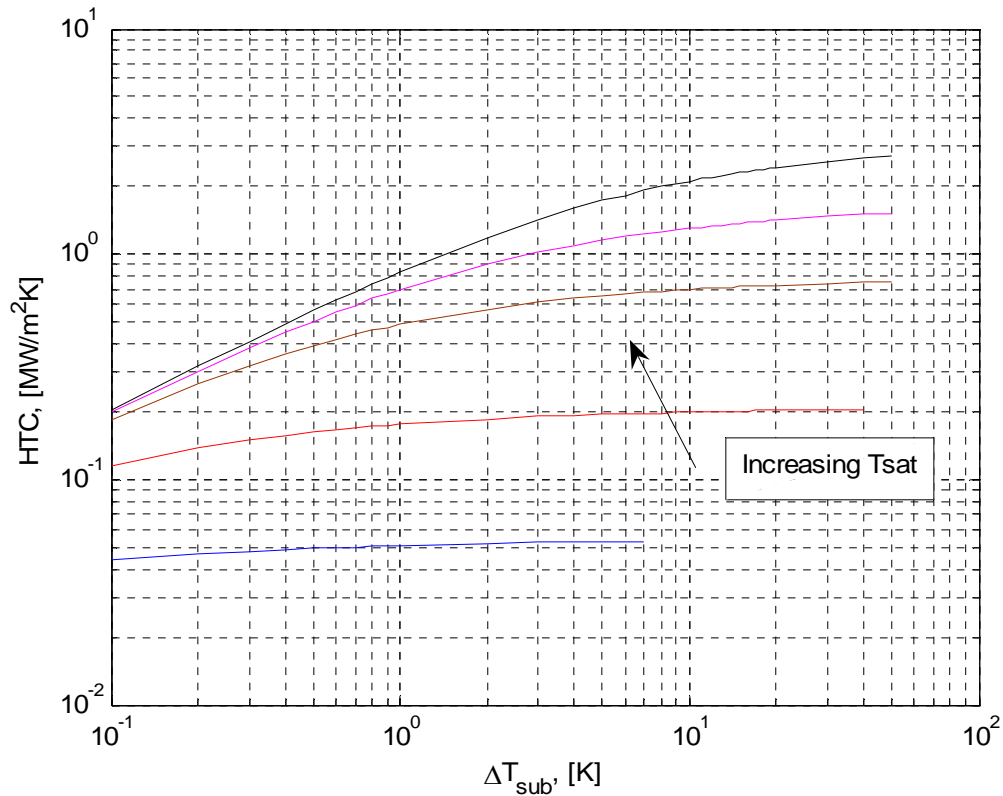


Figure 2-4. Heat transfer coefficient vs. subcooling, ΔT , for saturation temperatures of 280, 320, 380, 430, 500K.

All analyses involving the theory in this study were conducted in MATLAB, and their corresponding code files can be found in appendix A. Specifically, the calculations of (Eq. 2-10,11,12) were accomplished by the subroutine `DWC_HTC.m`, which can be

found on page A-1 of the appendix. The following figures were generated by DWC_behavior.m, page A-9.

For a given subcooling, significant vapor pressure dependence was noted in the subatmospheric saturation pressure range (Figure 2-4). However significant increases in HTC were absent above the 1 atm level. This was the precipitous drop predicted in the original work of HTC with vapor pressure below 1 atm [17]. The subcooling range was of more importance in this study than the saturation temperature. Here the saturation temperature ranged only from about 24 to 49°C but was constant for each data point. The surface subcooling, due to the temperature distribution on the diaphragm, ranged from 0 to as high as 30K across the radius of the diaphragm for each test.

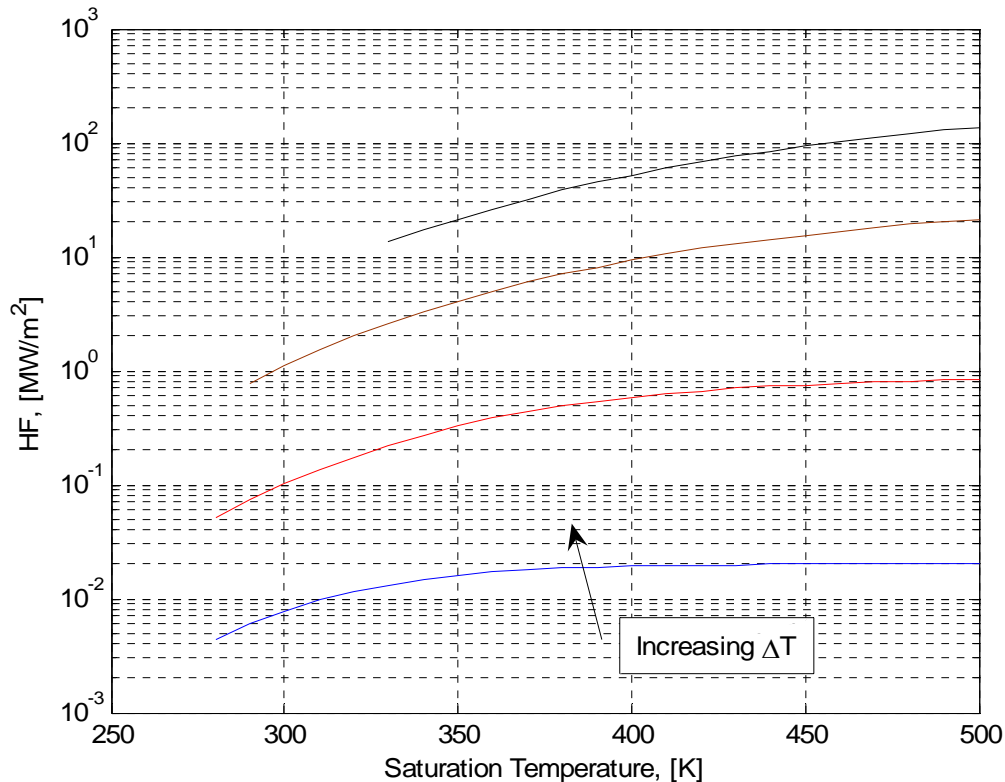


Figure 2-5. Heat flux vs. saturation temperature, T_{sat} , for subcooling, $\Delta T = 0.1, 1.0, 10, 50\text{K}$.

The predicted HF is relatively flat versus saturation temperature for a given surface subcooling (Figure 2-5). However, the relative differences in predicted HF for rising subcooling are roughly order-of-magnitude for order-of-magnitude, at a given saturation temperature (Figure 2-6). These results emphasize the dependence of HF on subcooling, clearly indicating a potential 4 orders-of-magnitude increase from near zero subcool to 50K, the highest considered, with 100 MW/m² peak HF predicted for a T_{sat} of 500K and ΔT of 50K.

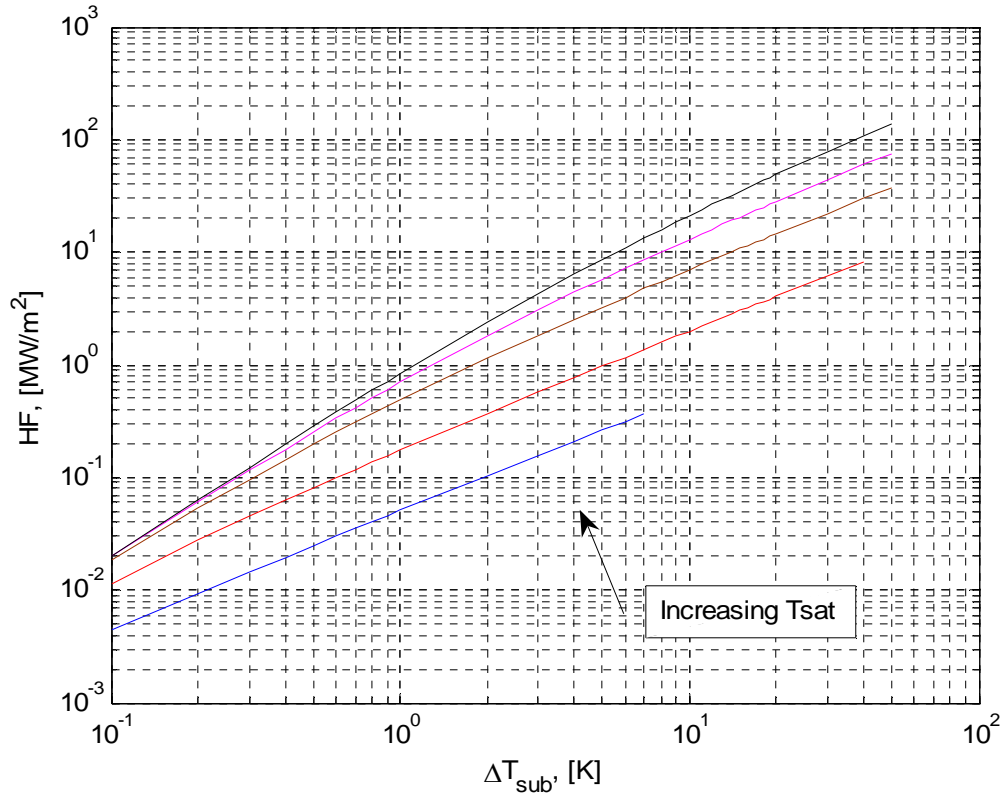


Figure 2-6. Heat flux vs. subcooling, ΔT , for saturation temperatures of 280, 320, 380, 430, 500K.

Heat transfer coefficient showed a tight distribution for subcooling from 0.1 to 50K (Figure 2-7). If it were possible to directly control the maximum droplet size, then further increases in the already high HTC of DWC could be theoretically attained. A few

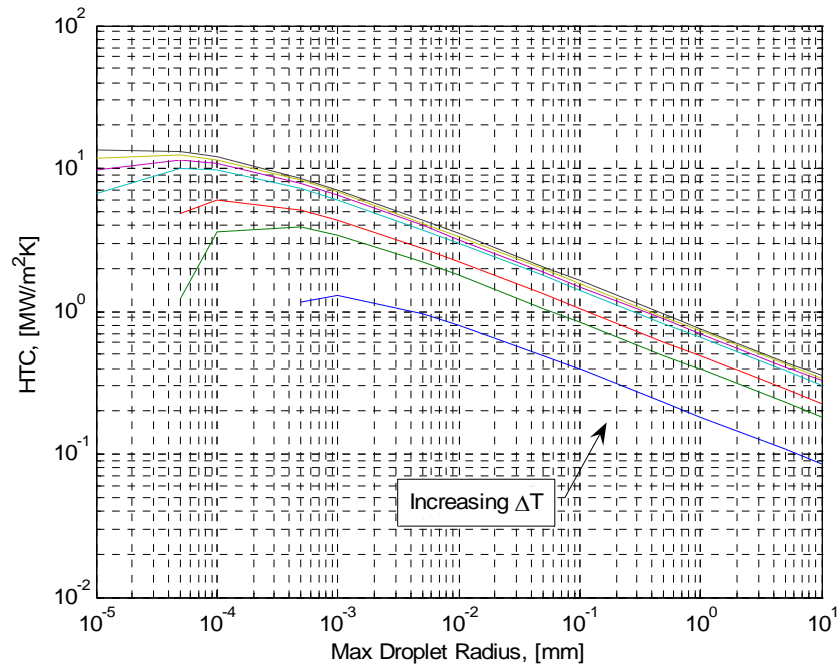


Figure 2-7. Heat transfer coefficient vs. maximum departing droplet radius for $T_{\text{sat}} = 380\text{K}$ and $\Delta T = 0.1, 0.5, 1.0, 5.0, 10, 20, 50\text{K}$.

investigations have used different methods to attempt this, as did the present study. Most of the investigations by Rose have focused on a vertical plate in essentially quiescent vapor. Therefore these studies did not distinctly examine the effect of maximum droplet size. The following studies however have all examined maximum droplet radius effect in one way or another:

- Citakoglu and Rose, 1969 [25] – varied surface inclination
- Tanasawa et al., 1978 [26] – periodic wiper applied to the test surface
- Tanasawa and Utaka, 1983 [27] – shear flow of steam
- Tanaka and Tsuruta, 1984 [28] – shear flow of steam
- Yamail and Merte, 1999 [15] – centripetal acceleration, i.e. body force with high subcooling range

The results of these studies will be examined in relation to the Rose theory in the Departing Droplet Size section of the literature survey.

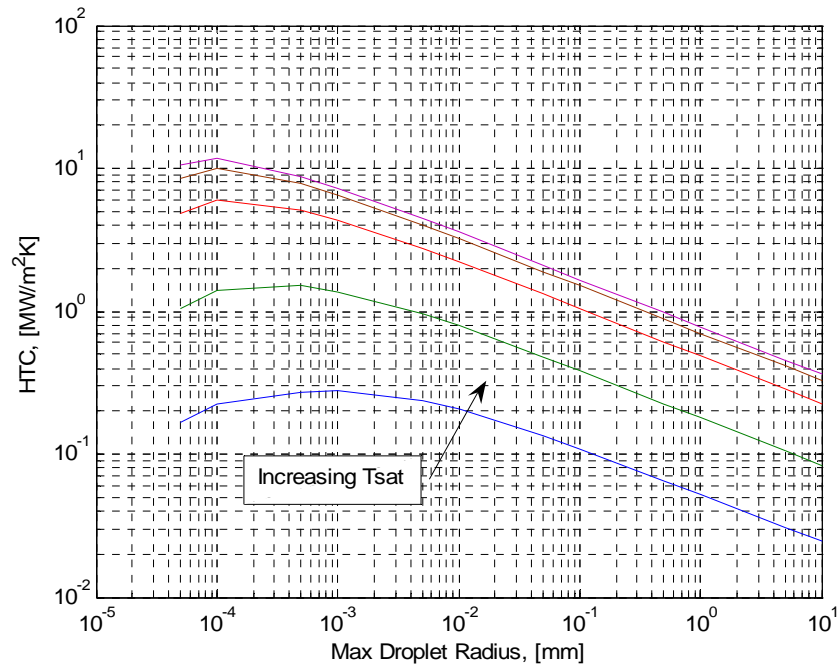


Figure 2-8. Heat transfer coefficient vs. maximum departing droplet radius. Surface subcooling was constant at $\Delta T = 1\text{K}$. Saturation temperatures used were 280, 320, 380, 430, 500K.

Examining the effects of maximum droplet radius (reached by growing drops just prior to departure) for a constant ΔT of 1K again exhibits the dip in HTC and therefore HF for sub-atmospheric pressures (Figure 2-8). Comparing HTC for a given departing droplet radius, over a range of subcooling showed significant dependence on this quantity, as well as on saturation temperature (Figure 2-9). This significant decrease of HTC with pressure was noted by Rose to be primarily due to the increase in the interphase matter transfer resistance. This quantity was the second term in the denominator of the expression for the HF through a single drop (Eq. 2-6).

The Rose theory predicts linear HF, in log-log coordinates, for any practical range of maximum departing droplet radii (greater than 10^{-3} mm) (Figure 2-10). Of course, smaller maximum departing droplet radius yields larger overall HF. Also, many smaller

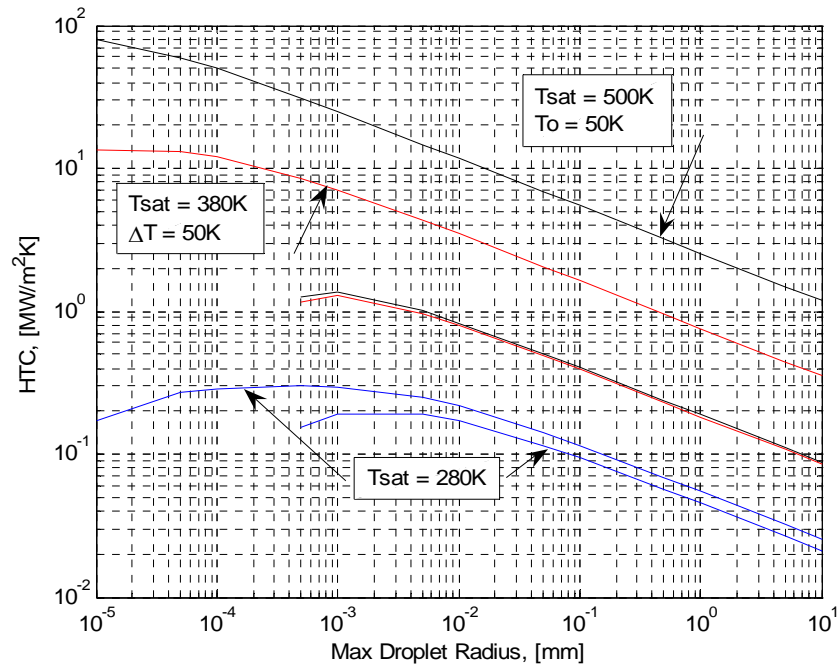


Figure 2-9. Heat transfer coefficient vs. maximum departing droplet radius for $T_{\text{sat}} = 280\text{K}$, subcooling is 0.1 and 5.0K. For T_{sat} of 380 & 500K, subcooling is 0.1 and 50K.

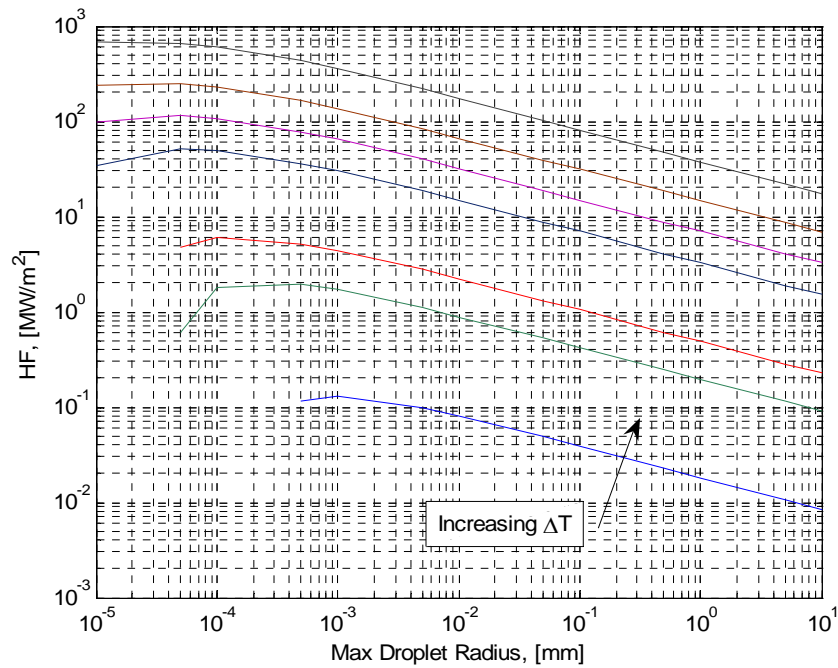


Figure 2-10. Heat flux vs. maximum departing droplet radius for $T_{\text{sat}} = 380\text{K}$ and for $\Delta T = 0.1, 0.5, 1.0, 5.0, 10, 20, 50\text{K}$.

drops provide less conduction resistance and larger total surface area for direct contact condensation than fewer large drops.

When theoretical HF is compared to maximum departing droplet radius for several saturation temperatures, successive increases in T_{sat} have less effect while the linear (in log-log coordinates) trend with droplet size remains for each case (Figure 2-11).

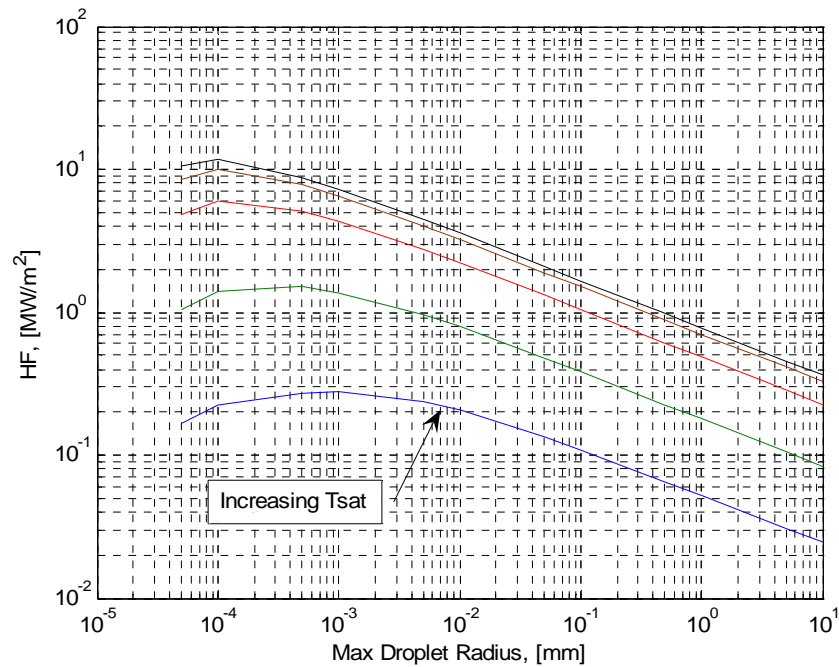


Figure 2-11. Heat flux vs. maximum departing droplet radius at $\Delta T = 1\text{K}$ and for saturation temperatures of 280, 320, 380, 440, and 500K.

Comparing overall HF with maximum departing droplet size (Figure 2-12) gives special emphasis to the dominating effect of surface subcooling. In fact, the overall HF function appears more sensitive to subcooling than either of the other two control factors, maximum departing droplet radius and saturation temperature. To illustrate this, a steady 4 order of magnitude increase over the range of ΔT considered can be observed here for a given maximum droplet radius and for the vapor temperatures considered.

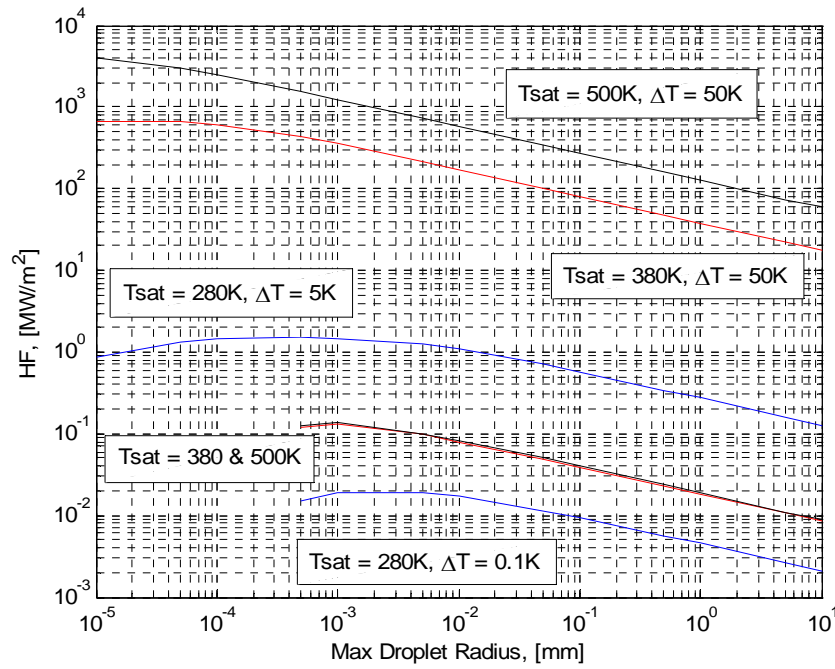


Figure 2-12. Heat flux vs. maximum departing droplet radius for extreme parameters. For T_{sat} of 280K, subcooling is 0.1 and 5.0K. For T_{sat} of 380 and 500K, subcooling is 0.1 and 50K.

The smallest thermodynamically viable droplet (Eq. 2-12) was dependent on fluid properties, saturation temperature, and the condenser surface temperature (Figure 2-13). Note that the scale was in nanometers, an indication of the 10^6 to 10^9 ratio of droplet radii active in the phenomenon of DWC. The range of the maximum departing droplet radius (Eq. 2-11) only changed a fraction from 1.1 mm at 280K to 0.77 mm at 500K. It is indeed the high number of these small drops combined with their small conductive resistance to HT that affects the relatively high HT efficiency of DWC over FWC.

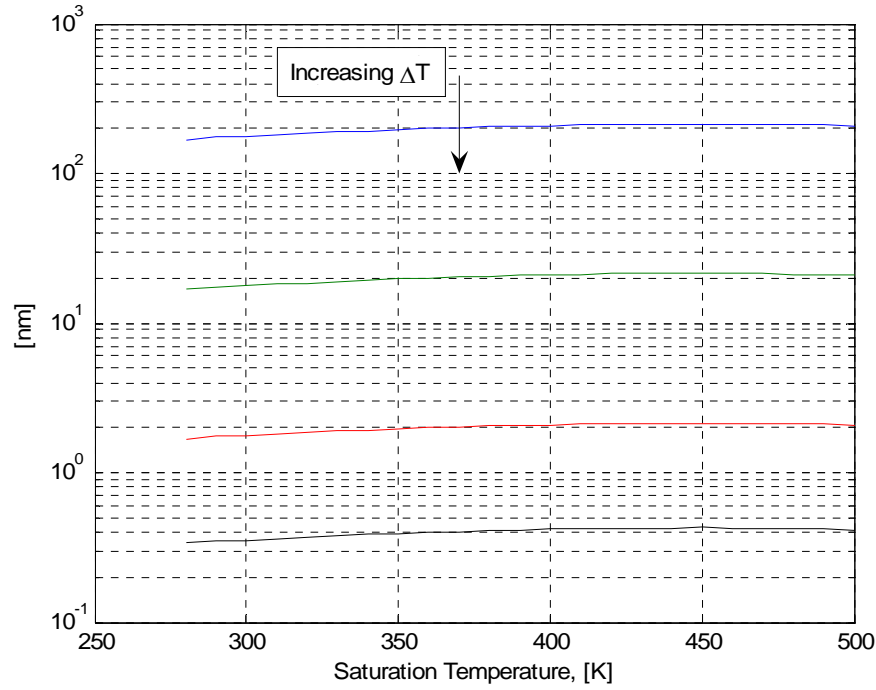


Figure 2-13. Smallest thermodynamically viable droplet radius vs. T_{sat} and for $\Delta T = 0.1, 1.0, 10, 50\text{K}$. Maximum droplet radius essentially constant between saturation temperatures of 280 and 500K, for which it is 1.1 and 0.77 mm, respectively.

Competing Models

Rose's theory was not the only one offered to model the phenomenon of DWC.

Just a few years after his initial publication, in 1969, Mikic [29] offered a theory of DWC HT that attempted to include the effect of condenser surface thermal conductivity. Mikic looked at the distribution of drop sizes qualitatively and took that in conjunction with a general expression for the interfacial mass transfer resistance, h_e , (Eq. 2-14) similar to that considered by Rose (Eq. 2-4).

$$h_e = \left(\frac{2\gamma}{2-\gamma} \right) \left(\frac{g}{2\pi} \right)^{1/2} \frac{h_{fg} P_{\text{sat}}}{R^{3/2} T_g^{5/2}} \left(1 - \frac{r^*}{r} \right), \quad 2-14$$

γ is the condensation coefficient. This quantity represents the fraction of vapor molecules striking the vapor/liquid interface which remain in the liquid. This value has

been a topic of considerable uncertainty until the last decade. g is the acceleration of gravity. h_{fg} is the heat of vaporization. P_{sat} is the saturation temperature. R is the gas constant of the vapor. T_g is the vapor temperature. r^* is the critical drop radius spoken of above. R is a given droplet radius. The author assumed that this expression for the HTC on the surface of a drop was constant over its surface area. He also noted that there was a critical drop radius, r^* , above which the thermal resistance of conduction in the drop dominated the HTC. By considering a drop sufficiently larger than the critical size to be adiabatic along with the relatively high HF in small drops immediately around it, he sought to estimate the resulting lateral temperature gradients in the condenser surface, of a given thermal conductivity, and from that estimation, the effect on overall HTC (Eq. 2-15).

$$\frac{1}{h} = \frac{1}{4\pi k_f} \left[\sum_j \left(\frac{r_j}{1 + \frac{2k_f}{h_e r_j}} \right) / A \right]^{-1} + \frac{\beta^2}{(1 - \beta^2)} \frac{(1 - \beta^{1/2})^{3/2}}{3.7k_s} \left[\frac{\sum_i c_i}{A} \right]^{-1}, \quad 2-15$$

r is the drop radius. k_f is the liquid thermal conductivity. h_e is the interfacial matter transfer resistance (Eq. 2-14). B is the fraction of area covered by visible – those with radius above critical – drops. k_s is the surface thermal conductivity. C is the radius of an inactive drop. A is the total area of the surface. The major assumptions of this theory are as follows:

- Known droplet size distribution, which at that time was only being qualitatively guessed at
- HTC independent of subcooling (contrary to Rose Theory)
- Negligible circulation in the drop
- Negligible drop in saturation temperature due the curved surface of the drop (contrary to Rose theory)

- A pure vapor, i.e. no NCG present

No experimental verification of this theory was offered. In fact, pains were made to note that this relation was not intended to be calculable, merely representative.

However, based on analysis of published results, the author did venture to estimate that the constriction resistance in a stainless steel was about 84% of the total resistance to HT versus 20% for copper.

This theory was not specifically tested in any experimental studies reviewed for this paper. However the topic of constriction resistance continues to be contentious in current discussions of DWC. This topic was addressed in more detail in the Constriction Resistance section of the literature survey.

Few alternatives have thus far been offered to the Rose theory. Subba and Murthy in 1983 [30] offered a model for DWC HT based on the opposite assumption of Rose. They assumed that the drops only served to insulate the surface and therefore all the HT took place on the bare surface between drops. Their investigation was purely analytical. The results were compared to those of Le Fevre and Rose [31], Citakoglu and Rose [32], and one other. The analysis also attempted to predict the effect of NCG on DWC HT. Both of the comparisons were claimed to be good, but again no offer was made of uncertainty. The shape of the curve was adjusted by assuming different functional forms of the condensation coefficient, some dependent on HF and some not, which caused the theoretical trace to alternately bound the data and to cross through it, however, which of the three adjustments gave the best fit was not noted. No other instances of this theory were found in the cited sources for this paper.

Tsuruta and Tanaka, in 1991 [33], presented a numerical simulation somewhat based on the same arguments as [29]. Additionally, they offered a non-dimensional

model that accounted for temporal variation in drop size and departure as well as considering the area underneath large drops as an adiabatic cylinder. Experimental verification of that theory in was offered in [34]. This theory was considerably more complex than the Rose theory, as it attempted to model the temporal variations in surface temperature as well as the overall HT. It was based on the Biot number of the surface and the non-dimensional drop radius. The experiments used thin film resistive thermometers to directly measure the condenser surface temperature of carbon steel, stainless steel, and quartz glass. The investigators found decreasing HTC for decreasing surface thermal conductivity. They also offered a Nusselt number correlation involving only three variables, maximum droplet radius and surface and liquid thermal conductivity ratio. The reported agreement of the correlation with their data and that of Hatamiya and Tanaka, 1987 [35] was $\pm 20\%$. The condenser surface was pure copper. The experimental portion was conducted at low vapor pressure to limit the lower drop radii to a size visible with micro-optics. Results showed condenser surface temperature fluctuations of up to $\pm 3^{\circ}\text{C}$ which increased in magnitude with HF. The troughs and peaks corresponded to a droplet reaching its maximum radius and then departing as confirmed by filming of the surface during test runs. The coldest surface temperatures occurred under large drops, since the surface was insulated. Conversely, the warmest temperatures occurred just after a drop departure or merger exposed bare surface, indicating a spike in HT.

The temperature sensors were deliberately made smaller than the expected drop radius, and were clearly visible as completely covered by a sessile drop on the condenser surface. This study considered only small surface subcooling, between 1.0 and 3.5°C and

assumed no dependence of HTC on subcooling. Comparison with data was limited, though agreement of theory and experiment was demonstrated in the examined parameter range.

Song et al., 1991 [36], asserted that a film of condensate existed between drops, which would contribute to heat transfer. Spectral reflectance measurements taken before and during condensation were purported to prove this existence due to their difference. No estimate of the thickness of this layer was offered, but it was estimated to be on the order of a few monolayers, that is a few times the width of a single condensate molecule. Curiously, spectral measurements were presented, with wavelength on the abscissa, as evidence of the occurrence of a single temporal event, pointing out a loosely repeating spectral pattern as evidence of droplet departure. The fact that the coordinate domain of the analysis was in question somewhat shadows the conclusions.

Gavrish et al., 1993 [37], presented a numerical simulation that modeled the process of DWC considering only the conduction through the drop, surface thermal conductivity, and the effects of sweeping of departing droplets. This therefore neglected both the interfacial matter transfer resistance and the small drop in T_{sat} due to the curved droplet interface considered in the Rose theory. The results, while in agreement with their own data for conductivity vs. HTC, were lower than most of the compared studies. The correlation of data with the model was labeled only as good with no quantitative measure of agreement offered.

Yamali and Merte, in 2002 [16], conducted an involved numerical simulation of DWC, considering high body force (1 to 100g) as a control of maximum droplet diameter and high subcoolings, from 10 to 100K. This followed their experimental study of

similar conditions in 1999 [15]. Their model assumed that most of the HT took place at the edge of the droplets, where the temperature gradient was largest and that furthermore most of the HT also took place through drops of very small radius due to their shorter conduction path and therefore higher gradient in temperature along with their high population numbers. They started with a complex relation for HF through a droplet based on T_{sat} , ΔT , and contact angle and other elements similar to the Rose theory. They then modeled the temporal growth and departure process over the entire condenser surface, accounting for the total volume of condensate flowing down the surface. Most previous studies had assumed that departed drops simply disappeared, a measure largely taken because of computational limitations. They also accounted for coalescence of growing drops and looked at the results of the model with and without the effects of sweeping. They then tracked the overall HT by the total volume of condensate at each step. The result of this simulation was to corroborate several of the trends predicted by Rose, namely that HF quickly reached an asymptotic value as a function of surface length, x , and so was essentially not dependent on this quantity. Another similar conclusion was that HTC was indeed dependent on HF instead of constant, as assumed by all the competing models mentioned above. A unique finding for very large body force (above 50 g), large subcooling (above 70K), and large x , a peak was found in HF that was analogous to a critical heat flux in pool boiling. However, the parametric boundaries for this phenomenon were so high as to not be of much practical concern. The simulation results compared well with the earlier experimental results [15], within $\pm 15\%$.

Droplet Size Distribution

A governing assumption of the Rose theory was existing knowledge of the population distribution of droplet radii. Much work has been done to estimate a sufficiently accurate model of this characteristic since then. The numerical simulation results of Glicksman and Hunt, in 1972 [38], and Burnside and Hadi, in 1999 [39], supported a simple negative exponential relation for the droplet size distribution, with much higher populations for smaller drop sizes. The former offered $-1/3$ as the exponential value, later selected by Rose for application with his theory. Some recent studies have employed more complex methods to model the droplet size distribution, such as the random fractal method [40] and mathematical morphology [41]. The resulting comparison to experiment was not significantly improved over the assumed simple exponential size dependence.

Rose and Glicksman, in 1973 [19], performed a close visual study of the temporal development of the droplet size distribution and had these main conclusions to offer:

- There were distinct generations of drops based on what areas were swept by falling drops.
- Drops of any generation were more or less uniform in size and spacing.
- The density of nucleation sites was independent of droplet size and the same for all generations.

The first assertion was backed up by the findings of Burnside and Hadi, in 1999 [39]. “Nucleation sites” refers to the microscopic surface defects that serve as bases for droplet nucleation. Numerical simulations have estimated them to be closely packed in either square or triangular arrays at a spacing of roughly one minimum thermodynamically viable droplet diameter with good comparison of results with

experimental data. The resulting site density estimates were 10^9 and 10^{11} sites/cm² [38,28].

Wu et al., in 2001 [42], conducted a microscopic study, at several magnifications, of low pressure DWC and found that a self-similar pattern in relative drop sizes existed at all magnifications. That is, that pictures at different magnifications looked almost identical but for different exact positions of drops.

As far as other parameters that might affect the distribution of drop sizes, HT parameters or surface roughness were eliminated [19,35], except for the conclusion that an increasing HTC with increasing subcooling was due to increasing activation of nucleation sites, specifically below 1K subcooling [43].

Rose [23,44] offered some modifications of the bounds of integration in his theory for a better fit to experimental data. Specifically, he suggested replacement of the lower bound of the integral in his theory with $10\tilde{r}$ instead of $1\tilde{r}$. The upper bound adjustment was two part with $1.5\hat{r}$ replacing $1\hat{r}$ below 1 atm while substituting $2\hat{r}$ for pressures near or above atmospheric. However in later issuances of the theory [12,18,20,24,45,46] these suggested adjustments were not repeated.

Effect of Maximum Droplet Size

Overall HT has been found to depend on the maximum, or departing, droplet size [15,27,37,38,39,42,44]. The only citations not to note this dependence were [25,26], however the range of drop sizes in these studies was relatively small (much less than an order of magnitude change). Various methods of controlling the maximum droplet size have been employed, ranging from numerical simulation [38,39] to a periodic wiper on the condenser surface [26] and condenser surface inclination adjustment [25]. However, the clearly dominant method employed was to induce significant vapor shear flow on the

condenser surface, such that the drag on the sessile droplets would limit their maximum size [27,37,47]. This method had the additional benefit of limiting the influence of NCG in the test vapor. Yamali and Merte, in 1999 [15], noted an increase in HTC with body force, but only for very high accelerations (i.e., above 5 g). This dependence was most likely due to a corresponding decrease in maximum droplet size, which was determined by the balance of body force and surface tension on the drop. These authors found a 6-fold increase in HTC for a 100-fold increase in body force.

In support of the idea that smaller droplets are more active than larger ones in HT [28], Tanasawa et al., in 1978 [26], noted a peak HTC of $1 \text{ MW/m}^2\text{K}$ just after the passing of the wiper, which was 2.5 to 3.5 times the time averaged value. This peak then decreased linearly until the next wiper passing. In a numerical simulation [39], a peak HTC of $2 \text{ MW/m}^2\text{K}$ was found. These high peak HTC values indicate the potential benefit of controlling maximum drop size in order to induce more intense HT than standard DWC.

General Results on Drop-wise Condensation (DWC)

Lorenz and Mikic, in 1970 [48], offered a numerical simulation of internal thermocapillary circulation in a liquid drop involved in DWC. The results showed that, for the applicable size range, internal circulation in the droplets was negligible. This finding justified one of the main assumptions of the Rose theory. Another main assumption of the Rose theory – that promoter thermal resistance was negligible – was confirmed by several other studies [17,23,49,50]. Two other studies found no dependence of DWC HT on tilt angle of the condenser surface for small deflections from vertical [25,31]. Neither of these two studies or [17,19] found any dependence on surface height for HTC. However, surface height dependence of HTC for DWC was noted [14]

merely by using a rectangular condenser surface for a series of results, then rotating the apparatus 90° about its central, horizontal axis and finding different results. It was unclear whether the orientation of the steam flow remained the same relative to the condenser surface or not, which may have accounted for the difference in results between the two cases. The condensation coefficient, contained in an empirical constant in the Rose theory, was defined as the fraction of vapor molecules striking the liquid surface which remain in the liquid phase, was the subject of much contention in the early decades of DWC research. Prior to 1985, most estimates of this fraction ranged from 0.45 to 1 [28,51,52], which left a considerable gap in the understanding of the process. Roughly after this date, reported results coalesced to unity [20,24,53].

Dr. Rose often argued that distinct differences existed between the DWC performance of various promoter methods and chemicals [13,21,31], which was corroborated by the work of others [54,55]. This assertion was fundamental to his argument against most of the evidence presented for a dependence of DWC HTC and HF on the condenser surface thermal conductivity, or constriction resistance, which will be discussed below.

An observed result of the efforts of Le Fevre and Rose to minimize the presence of NCG in the test apparatus was that HTC increased with increasing HF, or, less precisely, with subcooling [31]. This trend has been reported elsewhere [15,32,45,54]. Necmi and Rose noted [56], however, that for DWC of mercury, HTC was essentially independent of HF, due to the high thermal conductivity of the condensate. In [31,43] this trend was specifically labeled as an indicator of the NCG content of the test vapor. If HTC increased with HF, then NCG was termed sufficiently minimized. If, however, the

opposite were found true, then this would indicate poor control of NCG in the test apparatus. The latter assertion made sense, since the concentration gradient set up by the presence of NCG in the condensing saturated vapor, would tend to be exacerbated by greater relative concentration of NCG. This problem will be discussed in more detail in a section dedicated to the effects of NCG on condensation. However, some results have asserted HTC to be independent of HF [4,35]. It should be noted that studies making this case often tested only over a short range of HF or subcooling. With such small parameter ranges, a linear relation might be easily inferred between these primary variables. Those experiments covering large subcooling ranges, cited above, along with other theories [16,17], did show this trend.

The high HF and HTC values reported for DWC [31] were reported in a range of 0.3 to 1.8 MW/m² at 1 atm, with a maximum HTC of 0.3 MW/m²K. Tanasawa and Utaoka, in 1983 [27], reported HF from 0.5 to 10.0 MW/m² at subcooling from 0.8 to 50K, near 1 atm. As predicted by the Rose theory, a decrease in HTC with decrease in saturation pressure was reported by [17,18,24,35,55,56]. This decrease was noted to be up to 6-fold for DWC of steam at the lowest saturation pressures, as compared to atmospheric saturation pressure [35,55]. Rose, in 1998 [24], attributed this behavior to an increase in the interphase matter transfer resistance between the decreasingly dense vapor phase and the liquid phase. Significantly lower HTC was also noted at lower pressures [28,47]. For comparison to FWC, the results for DWC HT range from just 2 to 3 times higher [57], to a range of 5 to 10 times [37], to very high values of 20 to 30 times the FWC, as found in experiment and agreement with Nusselt correlation (Eq. 2-1)

[58,59]. The lowest DWC HF values were attributed by Rose to poor quality DWC promotion.

Some unique findings were those of Koch et al., in 1998 [14], that partial condenser surface coverage (of only 20%DWC/80%FWC) produced almost 90% of the full DWC coverage value of HF. Also, Citakoglu and Rose, in 1969 [25], used their surface inclination dependent measurements of DWC HTC to conjecture that the average HTC for a horizontal circular tube would be about 80% of a vertical plate under the same conditions. Finally, a point of note in all of the presentations which involved Rose, the HTC was only plotted as a function of HF and not surface subcooling. This distinction was made because of the error inherent in measuring this often small difference between the vapor saturation temperature and the surface temperature and then relying on its reciprocal for the HTC. For the same reason, he advocated only plotting subcooling on the abscissa or y co-ordinate and the HF on the ordinate or x axis for graphs comparing the two quantities [12,13,17,18,20–25,31,32,45, 46,52,53,56].

Constriction Resistance

There has been considerable contention, in the discussion of DWC, over whether the overall HT was at all dependent on the thermal conductivity of the condenser surface, that is whether a constriction thermal resistance existed or not. The Rose theory [17,24, 45], employed in the present work, assumed any dependence of HF on this property to be negligible, and obtained “excellent” agreement with experimental data for an array of promoters and for a few different surfaces. One contention of Rose, stemming from the observed differences in promoter effectiveness [31,60], was that surface chemistry was critical to the performance of any DWC scheme and might easily be the contributing factor in those studies which claimed affirmative evidence of such a dependence [21].

The authors used a thin, on the order of a few microns, copper layer on a stainless steel condenser block and compared the results for DWC with a solid copper block, finding a difference in HTC only on the order of magnitude of the uncertainty in this value. The thin copper layer on the steel block was assumed to offer identical surface chemistry to solid copper block, which was the key to Rose's argument that surface chemistry was the actual critical factor and not the substrate thermal conductivity.

Over the decades of research on this topic, various researchers have found their results to indicate a dependence of overall HT in DWC on the condenser surface thermal conductivity. Most did not account for potential differences in surface chemistry [33,34,37,50,54,61]. The latter pair of references offered a Nusselt correlation for DWC dependent only on thermal conductivity of the substrate and condensate and on the given non dimensional droplet radius that agreed within $\pm 20\%$ of the accompanying experimental data. The same two studies also noted an increased importance of constriction resistance at sub-atmospheric pressures. Two other studies [14,43] found a significant constriction resistance while controlling for surface chemistry. However, discussion of these findings did not include any mention of the inherent uncertainty in the small temperature difference measurements and the resulting implications when used in the denominator of the HTC. Mikic offered a theory including a constriction resistance [29] and then a study looking further at this theoretical dependence [62]. He then compared the theory to experiment [61], with visually agreeable results. However, the discussion of uncertainty, as mentioned above, was also omitted from this presentation.

In his 1998 address on the topic of DWC, Rose reiterated his opposition to the importance of a potential constriction resistance, while still acknowledging the existence

of debate on the topic [24]. In 2002, he went further to offer that it may be significant, in an additional ΔT of 1 to 2K, but only for very low conductivity surfaces and low HF, less than about 0.1 MW/m^2 , and small condenser surface lengths, less than about 10 mm [18]. In that talk, and also [21], he dispatched the findings of most of the studies cited above, which had all found evidence of a constriction resistance. He did this by questioning their methods of surface temperature estimation in relation to uncertainty and the magnitude of the difference in HT supposedly caused by the constriction resistance. Another issue he cited to question their assertions on constriction resistance was surface chemistry differences, which none had addressed.

Thus the literature was still quite divided on the existence and importance of constriction resistance. However, the author of the main theory, the investigator most often invited to speak on the topic of DWC, maintained that the potential importance of constriction resistance need only be considered under certain, limited conditions.

Drop-wise Condensation (DWC) Promotion

For most applications of DWC, some sort of promotion method was necessary to effectively reduce the wettability of the condenser surface, in other words to decrease the contact angle of the vapor-liquid-solid interface or contact line. Three main modes of surface preparation were used in the literature:

1. Direct application of organic or other compounds to the condenser surface
2. Addition of these same promoters to the bulk liquid reservoir supplying the steam to the condenser surface
3. Physical or electro-chemical manipulation of the surface makeup

Organic promotion, as the first group will be referred to, yielded the highest HTC values. This promotion mode was durable but only under clean laboratory conditions.

This was the mode most often employed in the study of DWC phenomenon itself.

However, this method later fell out of use due to its sensitivity to contamination usually present in industrial conditions. The substances employed in organic promotion included montan wax [55], montanic acid [55], dioctadecyl disulfide [31,55], oleic acid [21,25,32, 63], and stearic acid [64]. Self assembled organic monolayers of 1-octadecanethiol and 16-mercaptohexadecanoic acid were also tested [65], but the lifetime of DWC promotion was only on the order of a few hours. Tanasawa et al., in 1978 [26], employed a silicon resin with some success as a promoter.

Some of the same substances were applied by addition to the bulk liquid reservoir, by simply dropping a few ounces on the liquid surface, as was done with dioctadecyl disulfide [61], 2-ethyl-1-hexanol [66], and with partially-fluorinated carbon disulfide [37]. The latter case was tested with several condenser surface substrate materials. The investigators reported lifetimes of up to 4200 h. Furthermore, with this promoter the DWC promotion regenerated simply by adding more of it to the reservoir. This regeneration however could only be induced for a few cycles before disassembly and cleaning were required. The bulk addition was also coupled with the direct surface application of the organic promoter with good results by other researchers [55].

According to Dr. Rose, in 2002 [18], durable promotion of DWC still remains a “key barrier to commercial implementation.” Modification of the physical makeup of the condenser surface has been the focus of most of the work in recent years pursuing this goal. A thin plating of noble metals has shown durable results in a laboratory environment using gold [15,35] and silver [67]. The latter showed a considerable 2400 h lifetime. The effectiveness of these noble metals as promoters has been attributed to their

adsorption of trace organic elements from the air, as their promotion ability was notably absent when air exposure was not allowed between cleaning and testing.

Chromium was studied as an alternative to the noble metals for a condenser surface [35,63]. The best results came from a powder formed chromium condenser block, vacuum impregnated with oleic acid. This surface preparation showed a 3000 h life of DWC, under laboratory conditions.

Koch et al., in 1998 [14], used amorphous hydrogenated carbon films, described as a diamond-like coating. The physical toughness of these layers was held to offer potential for a durable promotion method, though no lifetime tests were conducted. Contact angle was also purportedly controllable in a small range, through the processing conditions of the coating.

What was described as a Langmuir-Blodgett (L-B) film showed much promise for a durable promotion method [59]. Several monolayers of barium stearate were overlaid on the condenser surface in such a way that the negative pole of the molecules all pointed away from the surface, resulting in a highly non-wettable surface. DWC heat transfer coefficients were reportedly up to 30 times higher than FWC. The coating was also reported as very physically tough and insoluble in both oil and water. This fact was quite significant since barium stearate was soluble in both when not prepared in this manner. The coating was also reported to be resistant to frictional wear and evaporation in a vacuum. No lifetime tests were conducted.

Dimensional modification of the condenser surface to increase sweeping frequency was employed by cutting vertical half-cylindrical section grooves in the condenser

surface [68]. However the increase in HT was at most 25% and was attributed only to the increase in surface area, despite a noted increase in sweeping frequency.

Teflon coating has been studied as a DWC promoter [47] with propylene glycol as the working fluid. Bochagov and Dorokhov, 1983 [57], induced DWC of steam on a Teflon coating with less success, likely due to presence of NCG in the vapor. More recent studies have employed techniques involving ion implantation, to reduce the wettability of Teflon [69, 70], and copper [58]. The Teflon results were poor due to bad physical bonding of the coating with the substrate, but the copper results showed promise in effectiveness and durability. Here a beam of ions was reflected from a target, made of a given material, onto the condenser surface to be modified, where the reflected ions combined with the metal atoms of the surface to form an ‘amorphous crystalline state’. This amorphous surface had a much lower surface energy than a pure metal surface and therefore showed much lower wettability. Ma, et al. [71], cited a study maintaining that minimization of surface energy was a more reliable method of assessing potential promotion effectiveness than contact angle or wettability. Species tested for implantation were He, Ar, N, and H. The H surface was reportedly the least wettable, with He and Ar next in line and roughly equal, and with N being the most wettable and therefore least effective DWC promoter. The HT results for the tubes used were on the same order of performance as organic promoters such as oleic acid, but with much longer lifetimes and better resilience.

In 1994, Zhao and Burnside [72] conducted the only successful test of a DWC promotion scheme under industrial conditions. An 800 tube bundle, treated in the manner described above, replaced a 1600 tube bundle of similar tube diameter and length

in a power station in China. Cr and O were the elements chosen for implantation in this test on Cu. Over the 15,600 h length of the test, DWC was never lost and the test was purportedly only curtailed due to the primary researcher's graduation. The authors of this study felt secure enough in their results to maintain that they indicated the possibility of permanent and reliable DWC promotion. The processing of the surface coating, however, was as yet prohibitively expensive.

In a review paper in 1999, Rose noted these promising developments [45], but he also noted was the downward trend in HTC with increasing HF. Rose had long held this decrease as an indicator of the presence of NCG in the condensing vapor, its presence thereby calling into question the accuracy of the reported data. By 2002, he had reverted to his contention that, "...reliable means for promoting dropwise condensation has yet to be convincingly demonstrated," [18]. In 2004 [20] he elaborated that more stable promoters had been developed but the reported HTC from these studies were still well short of the order of magnitude increase over FWC expected from monolayer organic promotion.

As a side note on DWC of liquid metals, Rose noted that promotion was often not necessary for these species [24]. He also noted however that the typical advantage of DWC over FWC was greatly reduced due to the very high thermal conductivity of the condensate, relative to a typical working fluid such as water.

Effects of Non-Condensable Gases (NCG)

Condensation is ideally studied with only a pure, saturated vapor supplied to the condenser surface. This state can be quite difficult to achieve in reality, since removal of non-condensable gases, or NCG, usually air, is effectively an asymptotic process rather than a discrete one. At equilibrium, the condensable vapor would have the NCG

molecules evenly distributed through the volume. However, once the process of condensation is initiated, a net mass flow toward the condensing surface is induced. The resulting movement of the bulk sweeps the NCG molecules with the vapor flow toward the surface. However, at the surface, the vapor molecules condense, but the NCG molecules cannot. In this manner, a continuous process builds up the concentration of NCG at the condensing surface [73]. Since pressure is a continuous property, the partial pressures of the two species must add up to the vessel pressure at any point in the vessel volume. Therefore, the increased partial pressure of the NCG at the condenser surface forces a decrease in the partial pressure of the vapor species at the condenser surface. Since, for a saturated liquid-vapor state, pressure and temperature are dependent quantities, the reduced partial pressure of the vapor species at the liquid-vapor interface leads to a decrease in the apparent saturation temperature.

If the driving force of the NCG buildup at the condenser surface were removed, that is, the cooling of the condenser ceased, the NCG molecules would disperse by diffusion, until they were evenly distributed in the vapor bulk again. However, if the cooling of the condenser proceeds at a steady rate and the geometry is 1-dimensional, then an equilibrium partial pressure, higher than that in the bulk of the vapor, will develop. The resulting concentration gradient then drives the diffusion of the NCG molecules against the net mass inflow of vapor. If the geometry of the problem is 2 or 3 dimensional, the NCG build-up and departure causes significant transients in the HT readings.

In 1965, Kroger and Rosenhow [74] modeled the 1-dimensional diffusional resistance problem of FWC in the presence of a non-condensable species, namely

potassium vapor in the presence of He and Ar, separately. Their simple model showed agreement with experiment within 25% for He. Results were less positive for the runs using Ar for the NCG. Steady state was never satisfactorily reached, the theorized reason for which was a periodic buildup and departure of Ar at the condenser surface, which would serve to insulate the condenser surface as they buildup and then allow HT to spike when they depart.

Many simulations of FWC have been conducted, growing from models similar to the diffusional one offered by Kroger and Rosenhow. These studies showed that geometry was a major factor in the sensitivity of a given condensation process to the presence of NCG. For closed channel flow, FWC, reductions in HT from the case with no NCG content of 30% to 60% were reported for simulations of 1% to 10% NCG concentration, respectively [75]. In a similar case to these studies, it was reportedly necessary for NCG concentrations to be as low as 0.1% in order for there to be no discernable effect upon the HT [76]. For FWC in a porous medium, a 50% decrease in HT for 5% NCG concentration was reported [77]. For closed channel flow geometry, only 3.3% NCG reportedly produced the same reduction [78]. A theoretical investigation of FWC on the inside surface of a rotating drum in [79] showed a process much more sensitive to NCG relative to those discussed above. Here a 1% NCG concentration produced an 80% reduction in HT. This increased sensitivity was explained as the centripetal acceleration due to the rotation of the drum increasing the resistance to diffusion of the NCG away from the liquid-vapor interface. The bottom line to all the above findings was that the effect of NCG in the condensing vapor on FWC was to impede the condensation process. Furthermore, this impediment was exacerbated when

geometry of the situation restricted diffusion of the NCG molecules. This conclusion makes sense in light of the diffusional problem described above. Parametric effects noted by these studies were as follows:

- More pronounced effect of NCG at lower pressures [75]
- More pronounced effect of NCG for restrictive geometry [75,77,79]
- Vapor with NCG has lower saturation temperature [76]

Le Fevre and Rose, in their 1965 presentation of experimental results on DWC of steam near 1 atm with organic promoters [31] and also the ensuing presentation of a theory on DWC [17], noted an extreme variance in the reported HT characteristics found for DWC. They attributed this variance to the presence of NCG in the test vapor. While not controlling directly by addition of NCG to the steam flow, the experimental study instituted a “close venting” scheme. This effectiveness of this scheme was demonstrated by varying the venting rate, to simultaneously minimize variation in the recorded surface temperature and raise the recorded surface temperature. These two effects indicated higher HT. In this case the surface temperature was found by extrapolation of the internal temperature distribution of the copper condenser block.

Also in 1965, Tanner et al. [54] studied DWC near 1 atm with the controlled addition of NCG to the steam flow. These investigators reported a strong dependence on HF of the sensitivity of DWC to the presence of NCG and also showed that DWC was significantly more sensitive to NCG than FWC. For example, for an addition of 90 ppm of NCG to the steam flow, or 0.009%, a 50% reduction in HF was noted for 0.1 MW/m^2 . However, for the same addition, but lower HF, 0.03 MW/m^2 , no reduction was noted over the case without added NCG. For the higher concentration of NCG, 500 ppm or 0.05%, still very small relative to those concentrations generating a noticeable reduction

in FWC, a 70% decrease was noted for the higher HF of 0.1 MW/m^2 and 20% decrease for 0.03 MW/m^2 .

In 1968, Tanner et al. again studied the effect of NCG on DWC [55], but this time for reduced saturation pressures from 0.03 to 0.1 bar or 0.8 to 3.0 in-Hg-abs. This pressure range almost precisely coincided with the pressure range of the present investigation. NCG concentration was verified as less than 1 ppm for the inlet steam without addition, and varied up to 15000ppm, or 1.5%. The effect of this controlled NCG addition on HTC was noted. The results showed that lower saturation pressure made the HTC significantly more sensitive to NCG concentration. In some cases, any concentration above 0.1% NCG yielded more than 50% reduction in HTC, clearly showing the following:

- DWC is more sensitive to NCG presence than FWC.
- DWC HTC is more sensitive to NCG for lower saturation pressures.
- DWC HTC is more sensitive to NCG presence for higher HF.

There were several different methods encountered in the literature for controlling NCG concentration in the study of DWC. The close venting strategy used in [13,31] was also employed in [21,22,32,25], all of which involved Dr. Rose. His experience lead him to note in a 2002 review [18] the ‘extreme sensitivity’ of DWC to the presence of NCG, even down to a concentration of a few ppm. The most common method was simply using vapor shear from the excess steam flowing past the condenser surface to sweep away any accumulating NCG [27,28,34,35,37,43,47,54,55,61,63]. A drawback to using vapor shear to control NCG was that, as demonstrated by the cooling curves constructed by Tanasawa and Utaka, in 1983 [27], was that steam velocity had a convective enhancing effect on the HT, impeding a pure analysis of the process of DWC itself.

Some, however, made no effort to control NCG [14,59,67], though most in this case did not indicate any appreciation for the importance of NCG in this process. Yamali and Merte [15] admittedly made no effort to control NCG, but it was estimated that the extreme body forces used in shear on the condenser surface in their study effectively accomplished what vapor shear would, by sweeping away NCG.

Additionally, increased sensitivity of DWC to the presence of NCG for increasing HF was noted [45,47]. Rose asserted that a downward trend in HTC with increasing HF (or subcooling) indicated a significant presence of NCG in the condensing vapor [24,31]. He later employed this assertion as a litmus test for the validity of DWC HT results [45]. This trend was corroborated by the contemporary results of Griffith and Lee [43]. Finnicum and Westwater, in their 1989 study of DWC on chromium [63] noted an important point about verifying the effectiveness of DWC by consideration of the increase in HTC over the FWC case. They noted that, if air was allowed to back up into the test cell, by decreasing the heater input, the appearance of the condensate in the FWC test changed to DWC, however the HTC was even lower than before the allowed lapse.

Heat Transfer with Vibration

Not much study has been made into the effect that vibration in general may have on phase change HT. In fact only one study was found looking specifically at the interaction of vibration with DWC. Some work has been done on vibration and FWC, but mostly in the range of low frequency oscillations, such as would be found in power plant pipes or on an ocean platform. In 1969, Dent offered experimental results of FWC of steam near 1 atm on a horizontal tube, subjected to vertical vibrations [80]. The frequency range was from 20 to 80 Hz with amplitudes up to 0.17 inch. In this case vibration was found to increase HT, but only by a maximum of 15%. That same year, Dent also offered

results for FWC of steam near 1 atm on a vertical tube, subjected to horizontal vibrations in the frequency range from 22 to 98 Hz, with a resonance at 38 Hz. Amplitudes ranged up to 0.5 inch at resonance, which also showed the peak HT increase of 55% over the non-vibrational case [81]. In 1977 Brodov et al. [82] also looked at FWC of steam near 1 atm on a horizontal tube, subjected to vertical vibrations. The frequency investigated was from 0 to 50 Hz, with amplitudes ranging up to 1.5 mm. They found a maximum increase in HT over the non-vibrational case of 20%, and also noted that no change in HT was observed without visually significant disturbance of the condensate film. In 1980, Savel'yev et al. [83] looked at the effect of vertical vibrations on both a horizontal and a vertical tube undergoing FWC of steam near 1 atm. The intensity of the oscillations was given as up to 0.12 m/s, where intensity was calculated from $2\pi fA$, f being the frequency and A being the amplitude of oscillation. The results were notable in that certain intensities showed a significant decrease in HT due to the addition of vibration, up to 40%. This decrease was noted as due to a vibrational anti-node causing the condensate layer to thicken significantly, thereby impeding HT. The maximum increase in HT was noted at 20%, which likewise corresponded to a node in vibrational mode that caused significant thinning of the condensate layer. In 1986, Nishiyama et al. [84] looked at the FWC of R-11 on a vertical tube subjected to oscillations likely to be experienced on an ocean mounted condenser. They looked at 3 modes of oscillation, heave – up and down motion, sway – side to side motion, and roll – pivoting relative to vertical. The frequency range investigated was from 0.1 to 1 Hz. The results showed no significant effect for the first two modes, but up to a 15% increase in HT for the roll case, also described as a pendulum motion of the vertical tube. This significant increase for the roll case was

notably accompanied by thinning of the condensate film due to the centripetal force. This corroborated the findings of Brodov et al., 1977 [82], that significant visual distortion of the condensate film was necessary for significant change in HT. In 1988, Nishiyama [85] used the same apparatus and experimental parameters, this time adding vertical flutes to the tube surface. The author again reported negligible effects on HT in the heave and sway vibration modes and some increase in the roll mode, due to the thinning of the condensate film.

The effect of vibration on phase change was also investigated by Oh et al., in 2002 [86]. This author looked at the influence of ultrasonic vibration on the melting process of solid paraffin wax. In a rectangular block, heated from one side and insulated on all others, the melting time was found to be decreased by up to 2.5 times. This increase in efficiency of the melting process was found not to be due to increased HT from the heater surface, but rather to be the result of acoustic streaming. Acoustic streaming is a phenomenon in which the compression and expansion waves of the vibrations induce the rapid formation and collapse of gas from the liquid, exciting bulk fluid motion which thereby increased mixing of the liquid volume. In 2004, Kim et al. [87] looked at the effect of ultrasonic vibration on pool boiling of FC-72 at 1 atm on a nichrome wire. The results showed an increase of 80% in HT in the natural convection range, 5 to 15% increase in the nucleate boiling range, and 5 to 30% increase in the saturated boiling range. Acoustic streaming was again deemed responsible for the noted increases in HT efficiency. The relatively more significant enhancement in the natural convection regime was explained by the fact that, in the non-vibration case, there was no induced mixing from vapor bubbles, while this effect was present due to cavitation and acoustic

streaming in the vibrational case. Since the nucleate and the saturated boiling regimes already had the vapor bubble induced mixing present, the enhancement of mixing by introduction of the ultrasonic vibration was less intense.

There was one study found, Shiraiwa et al., 2004 [88], which focused on DWC of steam near 1 atm and the effect of perpendicular mechanical vibration of a vertical plate on this process. Promotion was accomplished with oleic acid. The oscillations were driven by an eccentric crank mechanism from 0 to 15 Hz with a fixed amplitude of 5 mm peak-to-peak. The analysis was limited to three coolant flow rates, in a close cluster, and only a small range of steam pressure. Also, no mention was made of the surface temperature of the condenser plate or the material, leaving important ambiguity in the analysis of the quality of the DWC occurring in the test. No specific attempt was made to control NCG in the apparatus, a fact which showed in the low HTC attained of 11.7 kW/m²K. To attain a HTC this low, the Rose theory would require a surface subcooling much less than 0.1°C, and much lower than any probable uncertainty in the calculated quantity. This discrepancy between the Rose theory and the results of this study imply a significant, depressing influence of NCG on HT in these experimental results. Despite this discrepancy, the results clearly showed an increase in HTC of up to 40% due to the application of mechanical vibration, while noting a measurable decrease in the maximum droplet size and accompanying increase in sweeping frequency. An attempt at a numerical model was made, based on several simplistic assumptions of proportionality between maximum droplet diameter, growth time, and HTC, which predicted a much smaller increase in HTC than actually found, and relied on the measured HTC as a base. In sum, a positive increase in DWC HTC was shown in this study, but the quality of the

DWC was very low, asserted by comparison here to the Rose theory, and therefore the magnitude of the effect was questionable. Also of note in this study was a finding that temperatures at 15, 45, and 75 mm from the top of the vertical condenser plate were essentially equal for all the vibrations, corroborating a central assumption of the Rose theory, that HTC for DWC on a vertical plate is independent of surface height.

Piezoelectric Droplet Ejection with Heat Transfer

Some noted attempts have been made to establish a HT cell using a piezoelectric disc as the driving force to create a spray which then cools a heated surface. Heffington et al. [89,90] described a method of droplet ejection using a piezoelectric diaphragm which created a spray of water droplets by using a cover plate with holes in it which acted like nozzles. By using this setup for spray creation and direct contact condensation on a large pool of liquid, they authors achieved a HF greater than 100 W/cm^2 with a heater surface temperature of 85°C and a sink at room temperature. The design was highly gravity dependent to collect the liquid reservoir and keep the proper liquid level so that the driver cover was not flooded with liquid.

Xia, 2002 [91] also used a piezoelectric driver with a cover as a nozzle array. In this study, the nozzles were etched in the cover material in order to create jets of water to cool a target surface. The nozzle array was fed by pump and the liquid reservoir was subcooled. The frequency of driver operation was chosen such that a new droplet arrived as soon as the previous one had finished spreading on the heated surface. Especially of note in this case was the extremely high HF achieved of 1 kW/m^2 .

CHAPTER 3

THEORETICAL ANALYSIS

The theoretical analysis of this study was based on the Rose theory for DWC. The two main arguments of this function are saturation temperature, T_{sat} , and surface subcooling, ΔT . The theory assumes a simplified thermal circuit of the HT through a single drop of radius r , with direct contact condensation occurring only on the curved surface of the drop. Then a statistical distribution of the drop population by radius is assumed. This distribution is then used to weight the expression for thermal resistance of a given drop of radius r . Finally, the weighted expression is integrated over the assumed distribution of drop sizes, yielding a theoretical prediction for the average HF of a surface undergoing DWC of a pure vapor.

Manipulation of the upper bound of the integral, maximum departing droplet radius (r_{max}), was used to estimate an effective maximum droplet radius for the measured experimental conditions. A comparison of this value for r_{max} was then used to assess the effects of NCG on that particular experimental run and also the effects of the presence or absence of VIDA on HT. This section details the process used in the theoretical analysis of experimental data.

Since the intent of the design was to direct all HT absorbed by the heat sink through the brass shim of the piezoelectric diaphragm, the temperature gradients in this thin piece of metal would likely be significant. In fact, with a nominal 1K subcooling, the Biot number for the driver is on the order of 100 for the radial direction, also implying significant temperature gradients. Since the Rose theory depended on the

surface subcooling, it would then require an estimate of the surface temperature distribution in order to determine the theoretical HF distribution.

So initially, a boundary value problem was constructed to model the heat conduction in the brass shim. Axisymmetric heat conduction, cylindrical coordinates, and steady state conditions were assumed. Then the Heat Conduction Equation (Eq. 3-1) was solved using the following boundary conditions for a cylinder of brass with radius b and thickness c .

$$\frac{\partial^2 T}{\partial r^2} + \frac{1}{r} \frac{\partial T}{\partial r} + \frac{\partial^2 T}{\partial z^2} = 0, \quad 3-1$$

1. $T(r)$ as $r \rightarrow 0$ is finite
2. $T(r = b) = T_o$, the measured edge temperature
3. $\left. \frac{\partial T}{\partial z} \right|_{z=0} = 0$, insulated condition at rear surface of driver
4. $\left. \frac{\partial T}{\partial z} \right|_{z=c} = -\frac{q''_{avg}}{k}$, assumed average HF at front surface of driver

This assumption of average HF over the face of the driver greatly overestimated the actual temperature gradients. The input average HF had to be lowered to around 1W in order to lower the center temperature of the diaphragm to anything in the realm of the study. Even with this significant overestimate of the temperature gradient in the shim, the greatest temperature difference in the vertical direction was less than 1°C, an amount considered negligible in the face of a maximum difference between the center and edge temperatures of almost 40°C.

Armed with justification for neglecting the temperature gradient in the z direction, different functional forms were assumed for the likely radial surface temperature distribution of the shim. An exponential relation was deemed most likely to satisfy the

experimental conditions due to the implied zero slope at the origin (central axis) and ability to fix the slope at the edge (heat flux). The distribution was then defined with the following form (Eq. 3-2) and boundary conditions.

$$T(r) = Cr^n + B, \quad 3-2$$

1. $T(r = b) = T_o$
2. $T(r = 0) = T_{atm}$
3. $\left. \frac{\partial T}{\partial r} \right|_{r=c} = -\frac{q''}{k} = \frac{THR}{k \cdot 2\pi bc}$

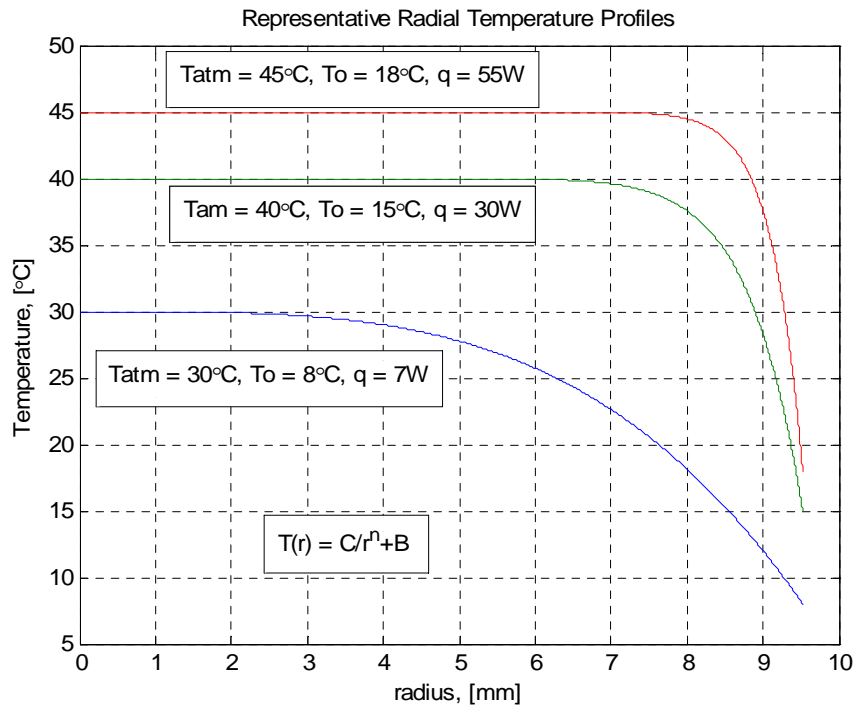


Figure 3-1. Assumed radial surface temperature distribution. Distributions based on three sets of experimental parameters representing a low, middle, and high HF case.

A theoretical HF distribution on the shim surface was estimated for each set of experimental parameters. First a radial-exponential temperature distribution was determined from a MATLAB subroutine, `exp_profile.m` (Appendix A) (Figure 3-1). For low overall HT rates (e.g., 7 W) the radial temperature distribution smooth and gradual.

However, for higher HT rates (e.g., 30 W) the temperature gradient at the edge of the shim was steep, and the majority of the shim surface area was near to the assumed atmospheric temperature, meaning that this portion of the surface would be relatively inactive in the DWC process.

Next, the assumed temperature distribution was fed into a MATLAB function that would determine the corresponding HF distribution, `DWC_HTC.m` (Appendix A), using the Rose theory (Figure 3-2). For the higher HF considered (e.g., 55 W), the majority of the diaphragm surface was relatively inactive in the HT. The higher the THR was the smaller the predicted active area of HT on the diaphragm surface. This was most evident from the HTC distribution in the top section of the figure, which clearly shows that the

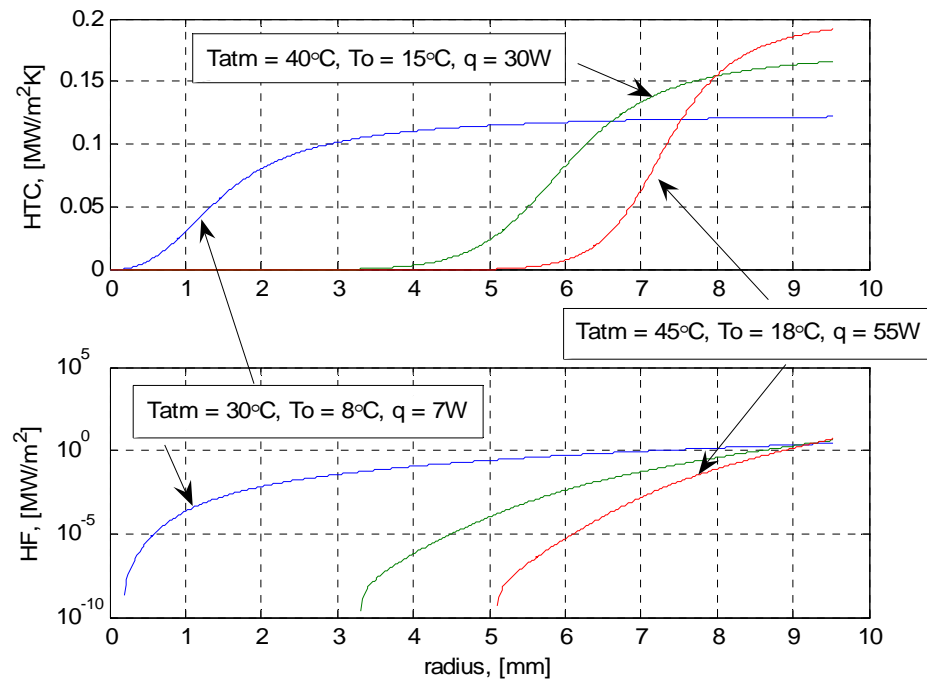


Figure 3-2. Radial HTC and HF distributions to follow the assumed temperature distributions.

higher HF-case HTC was more than an order of magnitude less than the peak value for about 95%, 60%, and 40% of the radius for the 7, 30, and 55 W cases, respectively.

The calculated radial HF distribution was next numerically integrated over the surface of the diaphragm, using a Simpson's Rule algorithm, `simpsons_rule.m` (Appendix A). The resulting value was the theoretical THR based on the inputs. This theoretical THR was then fed back into the temperature profile determination step to create an iterative scheme (Figure 3-3). Convergence of this scheme was quite slow and dependent on the initial guess for the THR input. Therefore a step was added after the determination of the theoretical THR which averaged the current iteration value with the value from the last iteration. The result of this additional step was that the number of iterations required for convergence to the desired error was reduced by a factor of about 20 and the dependence on initial guess was effectively eliminated from the scheme. This adjustment to the iteration was evaluated for accuracy by comparison to an actual converged result. Also a relaxation factor was added, which varied from 1 to 0. Using a relaxation factor equal to 1 resulted in the original scheme, without relaxation. While using a relaxation factor of 0 resulted in the current scheme. Zero was determined the fastest rate of convergence with no impact on the resulting answer.

Convergence acceleration aside, the computation was still time consuming, taking about 5 minutes of processor time per data value. Thus, for efficiency in determining uncertainty in THR from uncertainty in the measured values, a data table was constructed of theoretical THR values for a grid of saturation temperature and edge temperature values. The function was essentially linear in subcooling, despite the dependence of the lower bound of the HF integral on this value, and only slightly non-linear in saturation temperature for the ranges considered. Because of this, large steps were possible in the table construction. The input values used were T_{sat} of 24 to 50°C, in 2°C increments and

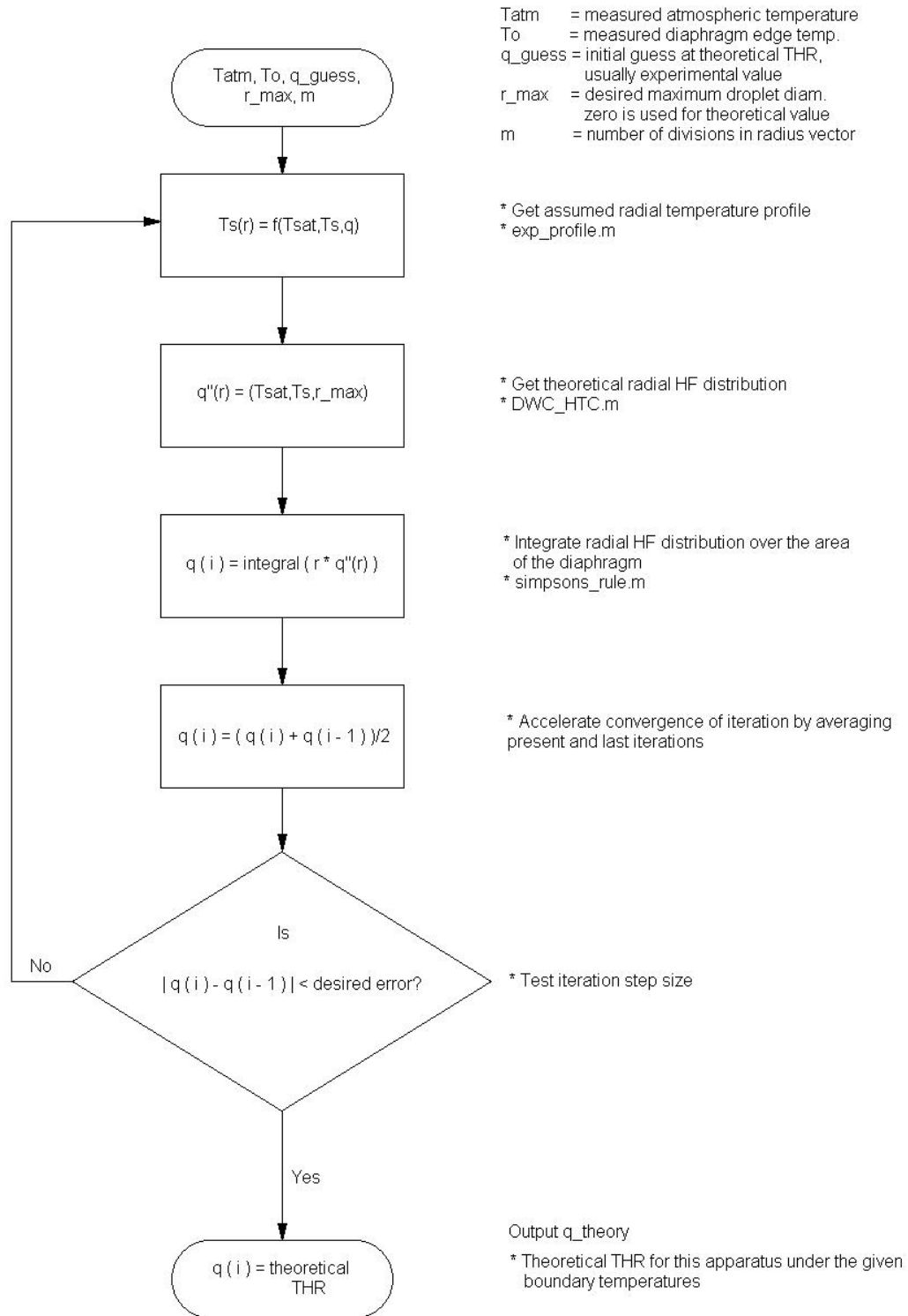


Figure 3-3. Block diagram of iterative loop to determine theoretical THR. A theoretical THR was estimated in this manner for each set of experimental conditions.

edge temperature (T_o) of 4 to 20°C in 4°C increments. One table was constructed assuming the theoretical maximum droplet radius (Eq. 2-11), which was essentially 1.1 mm for the range of T_{sat} used. Seven more tables were then constructed, each assuming a different value for r_{max} , from 0.01 to 4 mm.

For each of these tables of theoretical THR values for the given experimental variables and geometry, linear interpolation was used to determine the THR for the measured parameters of a given data point. This resulted in what was the official, theoretical THR, using the theoretical maximum droplet size from the Rose theory. This value was computed from the first table. Then the experimental parameters were used with the seven other THR tables to predict what would have been the results if the given maximum drop radius value had been in effect (Appendix B).

The seven r_{max} values were then fit to an exponential curve, similar to the one used for the temperature profile, by the least squares method. The least squares method was not able to be directly solved, as would be the case for a polynomial function. Therefore a brute-force method was used, by simply computing the sum of the squares of the error for sets of values that were likely to contain the appropriate coefficients. The minimum sum of the squared errors was chosen. Then several steps of range and increment reduction in the coefficient inputs were made to increase the precision of the coefficient estimates and decrease the overall error of the fit. The fitted curve was extended to a factor of 10 smaller than the lowest r_{max} used and to a factor of 10 larger than the largest r_{max} used.

The experimental THR was then compared to this fitted curve to determine an effective r_{max} for that data point. The effective values were then compared with the

theoretical r_{\max} to infer whether the results of that test had achieved appropriate HT for DWC (i.e., NCG presence was reduced enough that it did not appreciably affect the HT results). For those data points which had an r_{\max} larger than 10 times the largest table value, 0 was assigned and these points were then disregarded. The intent was that those runs with VIDA present would systematically show effective r_{\max} values smaller than those runs without VIDA present. This would result from showing higher THR for the same temperatures. The Data Summary and Comparison with Theory section of Chapter 6 addressed the results of the above theoretical analysis for this study.

Uncertainty was determined in these interpolations by taking the combination of the saturation temperature and edge temperature uncertainties that would produce the largest difference from nominal. These limiting values were then interpolated from the tables. The difference between these extreme theoretical THR values the nominal one, determined from experimental conditions, was reported as the uncertainty in theoretical THR. For the effective r_{\max} uncertainty, the uncertainty in the experimental THR was used in the same manner discussed above to calculate the high and low values, then the difference reported.

For example, the best data point attained from the experimental results was put through this process, and the results follow. For T_{sat} of $24.70 \pm 0.17^\circ\text{C}$, T_o of $13.8 \pm 0.2^\circ\text{C}$, and an experimental THR of 33 ± 2 W, the theoretical THR returned was 21.7 ± 0.8 W and the effective r_{\max} was 0.08 ± 0.04 mm. An exponential curve fit to the range of theoretical THR values, determined from the considered range of possible maximum departing droplet radii, shows an excellent fit (Figure 3-4). The square root of the sum of the squares of the residual error to this fit was 0.24 W, or about 1% of the theoretical THR.

Total estimation errors from using the tables could be expected to be of similar magnitude for all other experimental data points. This data was discussed further in the Data Summary and Comparison to Theory section of Chapter 6. The MATLAB programs used for this interpolation and curve fitting process were called `Get_Total_Heat_Rate_and_r_eff.m` and `Heat_Rate_Archive.m` (Appendix A).

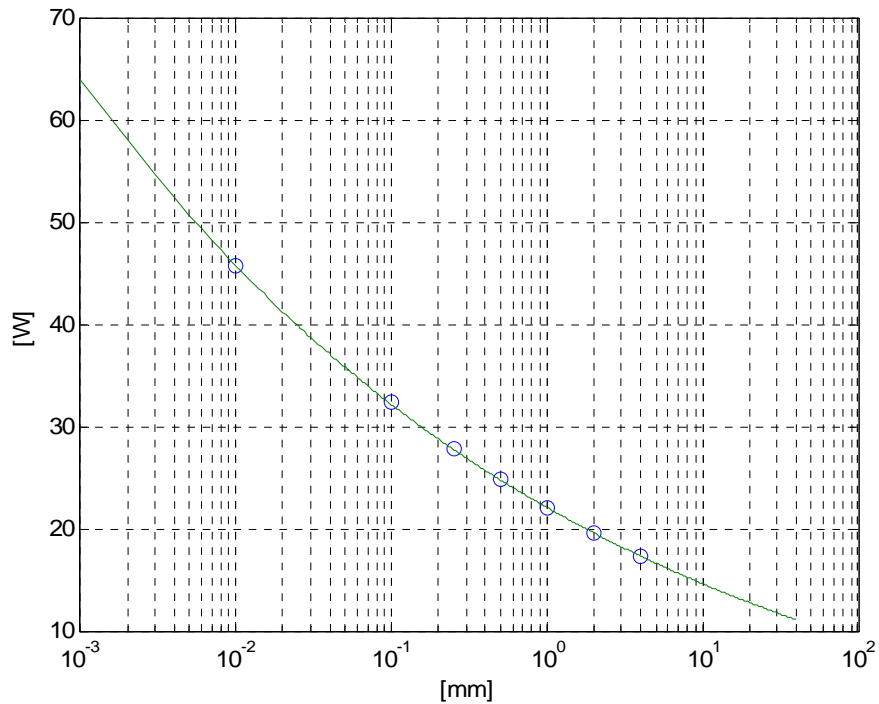


Figure 3-4. Theoretical THR vs. maximum droplet radius. THR is in W. Radius is in mm. Here, T_{sat} is $24.70 \pm 0.17^\circ\text{C}$ and T_o is $13.8 \pm 0.2^\circ\text{C}$. Circles mark the seven theoretical THR values for the given temperature conditions, determined from the seven different maximum drop sizes considered. The curve is the least squares fit to those seven data points.

CHAPTER 4 APPARATUS

The main aluminum cylinder that defines the pressure vessel for this apparatus was used from a previous study on a different topic. Therefore many design choices were made simply to accommodate existing features of this pressure vessel. For example seal grooves already existed on the ends of the cylinder and so only a smooth surface had to be made on the covers to work with them.

The original heater built for this experiment was taken from a study for spray cooling [89] and thus was intended to evaporate droplets impacted on its surface. The heat transfer was to be measured by the temperature gradient in the neck by three pairs of thermocouples. This temperature gradient could then be extrapolated to determine an average surface temperature for the heater. This choice of heater was made in a misguided attempt to reach toward an overall HT cell on the lines of the cited study above, in the hopes of moving closer to the ultimate goal of a two-phase HT cell that would be gravity insensitive.

Well into the first round of experiments, it was realized this strategy would not work. The design was inadequate because of the requirement of a saturated vapor environment. Therefore the apparatus had to be redesigned to focus on the condensation phenomenon only.

Also, it was realized that a benchmark would be needed for condensation without vibration, and the only relations that might apply to this apparatus were for an isothermal vertical plate. Thus the experimental pressure vessel (Figure 4-1) was set on a stand, on

its side, so that the condenser surface was close to vertical. The orientation of the outside of the vessel was checked with a common carpenter's level. This method was deemed appropriate based on the experimental results of [25], which showed the DWC process to be relatively insensitive to changes in surface orientation. In that study, a 10% decrease in HTC over the vertical case required a 40° forward pitch or a 10° rearward pitch. Therefore if this condenser surface was within 3 or even 5° of vertical, then any effect would likely be slight.

Ice was added to the coolant reservoir to lower the inlet temperature and provide more driving force for the HT process on the diaphragm. The coolant used was tap water. A simple model was constructed for desired reservoir temperature and consequent required mass of ice, and the amount found to be reasonable for acquisition and transport. Fifty pounds of ice would be required for an initial reservoir temperature just above the freezing point of water. Later on, when it was determined that the experiments needed to be run for long time periods, the procedure for ice handling was refined, as described in the Chapter 5.

However, the heater problem still needed a quick fix. By experiment, it was determined that a 50 W halogen lamp would provide both extra light for video records and sufficient heat to drive the experiments. However, this would leave little control or measurement of the heat input to the apparatus. Various placements of the light were tried, and below the bottom window of the vessel, facing up was selected as the optimal. This would allow the placement of the fluid reservoir in the bottom window and get the bulk fluid as close as possible to the heat source. Initially, a crude reservoir for liquid was fashioned from a piece of aluminum and placed in the bottom window.

Experimental runs with this configuration, however, rarely showed any condensation on the windows of the vessel. Since the vessel was basically cold to the touch and the T_{atm} measured inside the vessel was above ambient, this implied that the vapor atmosphere inside the vessel was not saturated.

In order to channel more of the heat energy from the lamp through the fluid reservoir, further tests used the window well itself as the reservoir. After this, when the test atmosphere temperature rose above the lab ambient temperature, condensation almost immediately appeared on the viewing windows, indicating the vapor was indeed saturated. Additionally, a thermocouple was placed in the liquid reservoir and this reading tracked very closely with the recorded vapor temperature for those runs with good NCG control. In fact, the gap between these two values would serve as an excellent indicator of NCG presence and also vapor saturation condition. The liquid reservoir temperature would rise above the measured vapor temperature when significant NCG was present, as part of the depression of apparent saturation temperature accompanying this presence. Further, if the vapor temperature recorded was higher than the liquid reservoir temperature, then the vapor was superheated. This assumption was backed up by a lack of condensation on the viewing windows despite higher than ambient vapor temperature for these cases. Also, modifications were made to increase its liquid capacity to about 40mL. This capacity proved to be sufficient enough that replenishing the water supply was only necessary in one experiment of all those performed. The only removal of vapor from the system was through the vacuum pump.

An oblique view of the pressure vessel showed the driver surface through the side window of the vessel (Figure 4-1). Since the original heater was in the place of the

window frame on the top cover, all videos in the first and second stage of experiments were taken from this corner view. Frames taken from those videos can be seen in Chapter 6, along with a full explanation of the three phases of the experimenting.

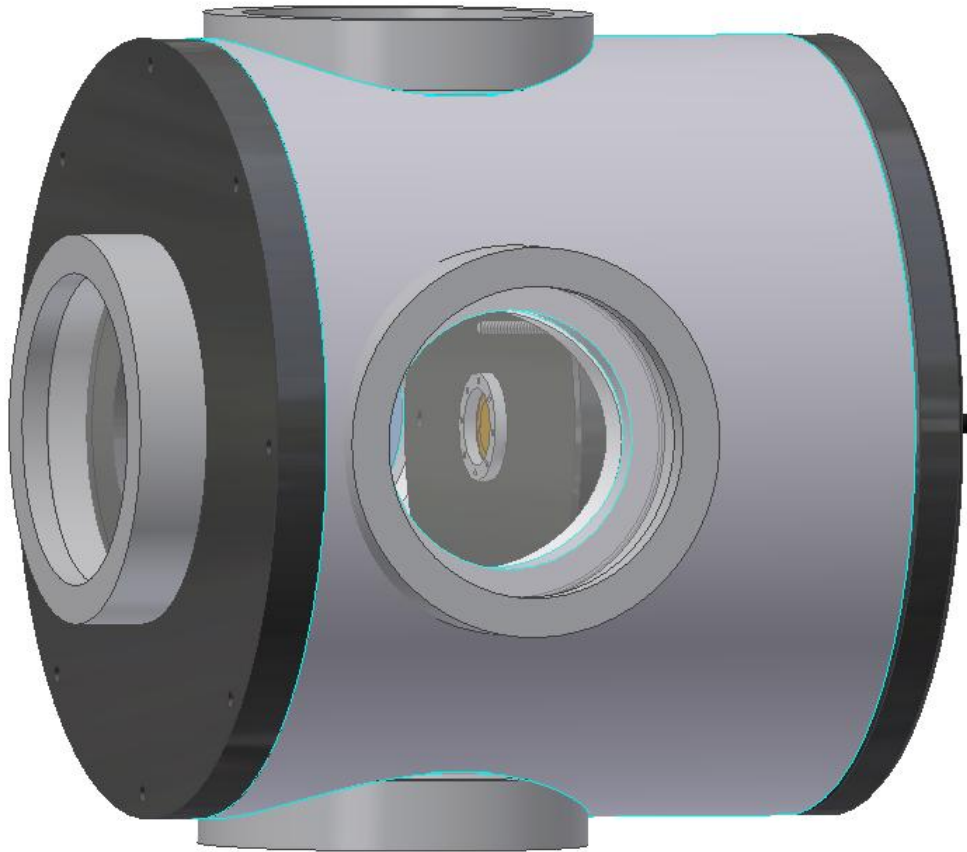


Figure 4-1. Corner view of experimental apparatus.

After the discovery of a significant air leak around the edge of the old, disused heater, it was removed and replaced with a window. The new front window provided a much improved view of the condensation process for videos in the third and final phase of experiments and a better seal.

The atmosphere of the pressure vessel was effectively divided into two parts, although they were not sealed separately (Figure 4-2). No method of sealing was available that would be effective and also provide a good thermal connection between the

driver edge and the cooler. Also, sufficient gas flow was needed between the two sides to allow for an effective evacuation process. Two small notches were made in the upper edge of the diaphragm frame (the divider between the two sections of the pressure vessel) for this purpose. As higher heat rates were encountered in experiments, condensate droplets on the face of the diaphragm frame were noted. This indicated that significant HT was occurring across the Diaphragm Frame, separating the two sections of the atmosphere. Insulation was added (about 1 in. thick) to the cold side of the frame and also around the exposed brass surface of the Cooler to impede this process. The insulation used was Permatex® brand silicone RTV sealant.

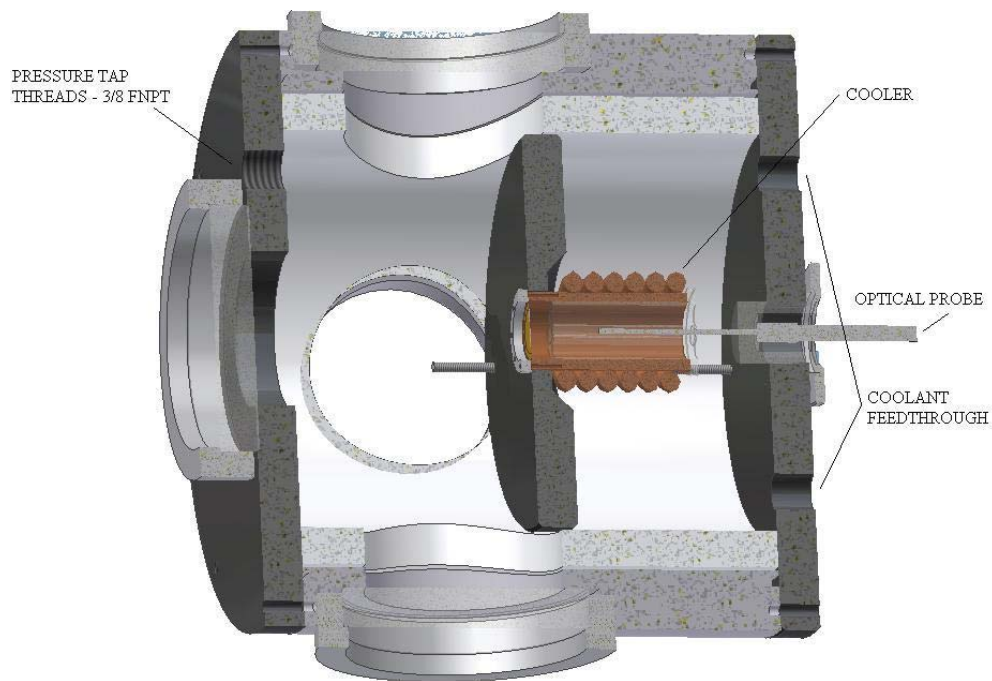


Figure 4-2. Sectioned view of experimental apparatus.

Further testing showed that additional insulation was necessary around the diaphragm clamp, where the copper cooler was the closest to hot side atmosphere. The caps of the machine screws that held down the clamp and also the supporting posts of the diaphragm frame needed to be covered with insulation as well, to reduce obvious

extraneous condensation (Figure 4-3). The fully insulated diaphragm frame was covered in the orange sealant, but showed little visible condensation during the test runs.

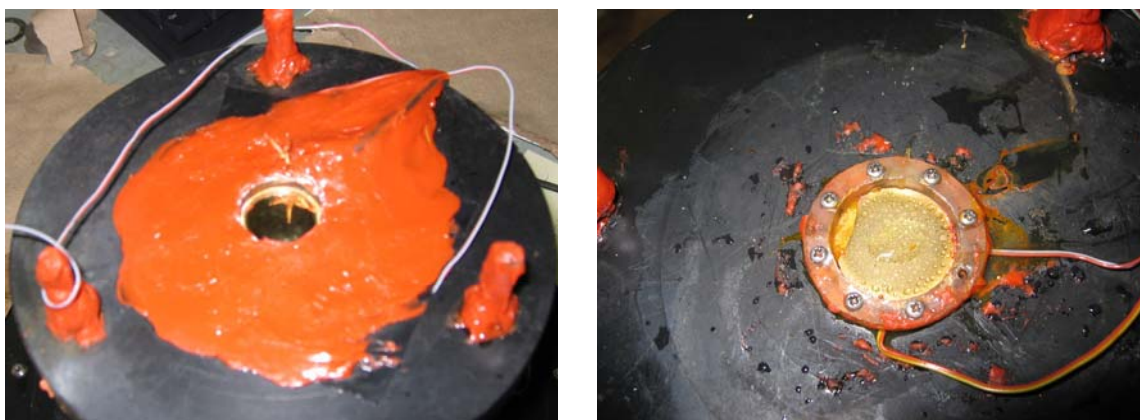


Figure 4-3. Insulation applied to and removed from diaphragm frame. The silicone sealant was applied as insulation over the metal screw head, the metal support posts and the central area of the Diaphragm Frame face. Visible wires are thermocouples. Left picture is a fresh insulation application, with polished driver surface. Right picture is a tarnished driver surface after removal of insulation.

Given a few days, the mirror-like finish of the polished brass driver surface could become quite tarnished. In this state, the quality of DWC produced was not good. The normal cleaning regimen was described in Chapter 5. The polishing was done to aid in the promotion of the DWC mode. However, full FWC was never actually achieved in this apparatus. It was eventually noticed that globules of oil were nearly always present on the liquid surface of the reservoir the day after an experiment. The most likely source for this oily residue, which also covered every other surface inside the vessel, was the silicon sealant and presumably, this contaminant was a dropwise promoter. There was also a silicone based Dow-Corning vacuum grease used on the vacuum seals which may have contributed to the oily residue. It has been proven in several studies that promotion can be effectively achieved by addition of an organic promoter to the fluid reservoir [37,43], as discussed in the Promotion Methods section.

In light of the relatively low saturation temperatures that were used in the experiment, as many components as possible were made of polymers rather than metal in the hopes of decreasing extraneous heat transfer and machine shop time. The Top and Bottom Covers and the Diaphragm Frame were all made of Delrin® (Figure 4-4). The Insulation was made of Teflon®. The optical probe Guide and Seal along with the Diaphragm Clamp were of polycarbonate. The choice of different materials for these different components was based solely on availability of stock in appropriate geometry

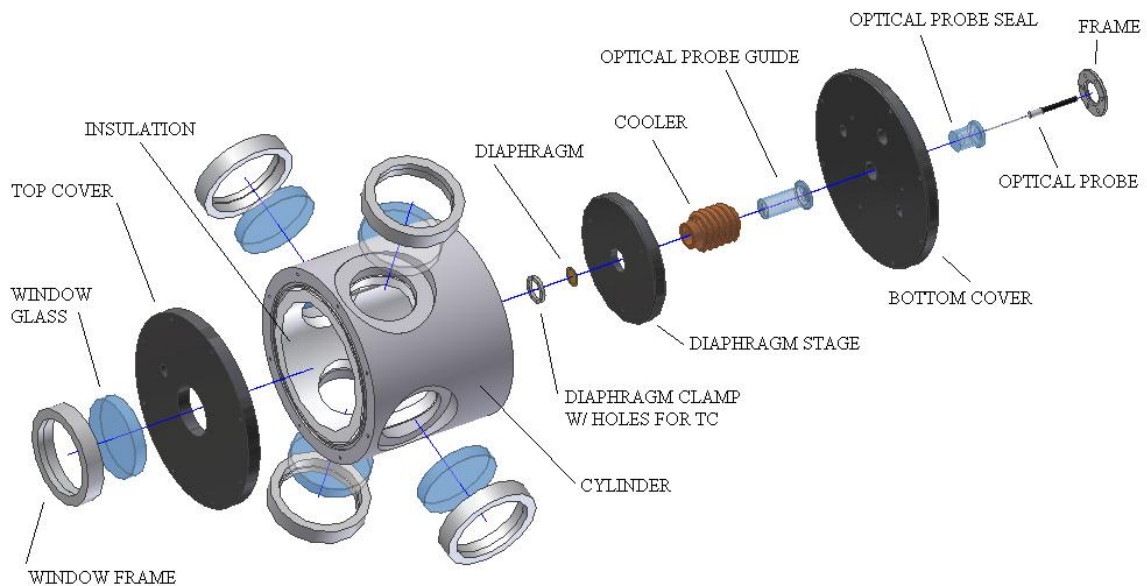


Figure 4-4. Exploded view of experimental apparatus.

and a maximum service temperature of at least 200°F. Some items were omitted from the exploded view for clarity, such as the vinyl coolant hoses and the Y-Or-Lok bulkhead fittings for them, whose locations can be noted in the cross-sectioned (Figure 4-2). All connecting hardware, pressure fittings, and soft seals were also omitted. The multi-pin connector/vacuum feedthrough was left out as well. It fit into the third hole in the bottom cover, was held down by 6 screws, and had a soft seal. All soft seals were manually cut from Buna-N sheet stock. The components that were press-fit, namely the Cooler into

the Diaphragm Frame and the Optical Probe Seal into the Bottom Cover, sustained liberal application of the silicone sealant for adhesive and sealing properties.

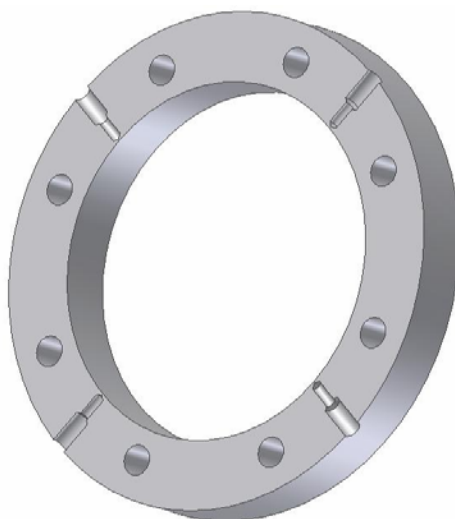


Figure 4-5. Diaphragm clamp, lower face showing grooves for placing thermocouples to measure edge temperature, T_o .

There were 8 thermocouples placed internal to the pressure vessel. Four of them were placed evenly around the circumference of the Diaphragm Clamp, in specially machined grooves (Figure 4-5). The grooves clamped the thermocouple beads to diaphragm edge and also clamped the edge to the Cooler. This design attempted to place the thermocouple junctions as close as possible to the edge of the exposed diaphragm surface without piercing through the wall. In practice, however, this very thin barrier between thermocouple and liquid eventually broke through in three of the four places on the clamp, allowing visible drainage of condensate through the lower holes.

Quantitative estimate was not made of how much this phenomenon might have affected the HT measurements. Qualitatively, it was expected to increase overall HT by decreasing the amount of condensate around the edge of the diaphragm, which would otherwise serve to insulate the most active portion of the condenser surface. Three of the

remaining thermocouples were placed in a bundle, with the tips spread, about $\frac{1}{2}$ inch above the condenser surface and just over the edge of the clamp. These three thermocouple readings were averaged and this value taken as the atmospheric temperature, usually taken as the saturation temperature, as described in detail in the Results and Discussion section. The one remaining thermocouple was placed in the liquid reservoir, with the tip slightly curved up, to hopefully measure the liquid temperature rather than the glass surface temperature. Note, however, that this liquid temperature measurement was only made for the last five days of testing. Two more thermocouples were employed on the outside of the apparatus, one each just outside the bulkhead connectors for the coolant lines. A hole was punched with a hot nail through the vinyl coolant line. Then the thermocouples were stripped of the clear, plastic outer casing, but not the Teflon insulation. This measure was undertaken because cooling water would be pushed by the flow pressure back through this casing and into the DAQ board. Next the stripped, but insulated, thermocouples were inserted in the holes in the coolant lines and secured with a liberal application of Copper-Bond® brand epoxy. After allowing 20 to 30 minutes for this to cure, the arrangement was leak tested with the flow control valve on the flow meter both fully open and fully closed. If no leakage was apparent after ten minutes with the valve closed, then the seal was deemed sufficient.

The cooler was constructed of copper stock. The central cylinder was made to accommodate the Optical Probe Guide with a press fit and to support the Diaphragm with at least a 1mm contact around the circumference. Two ‘washers’ were then made along with a tube section, all of which were soldered together to make the flow chamber of the cooler. Two holes were then drilled to accommodate the inlet and outlet tubes, also of

vinyl. Like the coolant thermocouples, these were secured in place by liberal applications of Copper-Bond® epoxy. Enough length was left on the tubes to facilitate easy attachment of the bulkhead fittings.

The Diaphragm Frame was supported by three lengths of 3/8 coarse all-thread, of galvanized steel. Certainly stainless would have been better, and better yet would have been something less thermally conductive, possibly another polymer. Eventually, these posts had to be covered in silicone insulation as well, since significant condensation was observed on their surface in the test chamber. Before the application of silicone, however, the height of the Diaphragm Frame had to be adjusted for displacement sensor calibration and then set for the testing. Two nuts were placed on the each post, below the frame to support it and lock each others position, then one on top. Once set, further adjustments were not made until the final calibration and displacement measurements of the used driver, after the conclusion of testing.

The pressure tap for the apparatus was eventually located toward the top of the top cover, relative to the side orientation pictured in the corner view (Figure 4-1). Special attention had to be paid to the pressure tap and fittings orientation since, after repeated evacuation procedures of a hot test environment, enough condensate would collect in the vacuum hose to clog the flow and prevent effective function of the vacuum pump. The vertical orientation of the fittings allowed this collected condensate to be emptied back into the test vessel by simply lifting the tube above the fitting inlet.

As the importance of NCG effects on DWC became apparent during the course of the investigation, the pressure integrity of the apparatus became a big issue. An earlier section on NCG effects in this paper looks qualitatively at the dynamics of the problem

and at the reported effects in the literature. Upon the initial assembly of the apparatus, prior to any experiments, a bubble test was applied to test for leaks. Bottled nitrogen was hooked up to apparatus and the internal pressure was raised to about 50 psi. The vessel was then submerged. Several leaks were located and fixed in this manner, however, due to the sensitivity of DWC to the presence of even small amounts of NCG, this method turned out to not be a sufficient leak control. After data trends indicated a significant air leak during the intermediate phase of testing, vacuum grease was applied to all soft seals. Initially this made the leaks worse but then better after the excess grease was wiped away and the apparatus reassembled. However, this still did not fully address the problem. The likely effects of NCG resultant to poor sealing were covered in more detail in the Results and Discussion section. Detail drawings for those parts listed in the above figure that were manufactured in-house can be found in Appendix C.

Equipment

Several other pieces of equipment, in addition to the main apparatus described above were needed for the conduction of this investigation. A schematic layout was presented, followed by a description, by letter, of each component (Figure 4-6).

Element A was a Mastercool brand vacuum pump, 2 Stage, 1.5 CFM capacity, and oil lubricated. This pump was intended for air conditioning equipment service, and thus was not intended for much contact with water vapor. Significant amounts of water vapor put through the pump would condense in the oil, degrade the performance, and cause it to over heat. For this reason, the evacuation operations described in the results section were limited to 5 to 10 minutes and the pump oil had to be replaced each day. Capacity was a few ounces of standard vacuum pump oil.

Element B was an array of brass ball valves and fittings, setup to allow independent venting of the test vessel and isolation of the pressure gauge from the vessel and also from the pump line. This separation of the gauge was necessary due to a small, constant leak in the gauge diaphragm. Because they were thermally exposed to the environment inside the test vessel, albeit minimally, the valve configuration was wrapped several times in reflective foam insulating tape to minimize heat loss. This potential loss would not have affected the accuracy of the measured THR, but rather the insulation was a cautionary measure to prevent any reduction in heat supply capacity to the vapor.

Element C was a vacuum gauge, ACSI 1200-VACU, with a 0-30 in-Hg range and an uncertainty of $\pm 1\%$ full-scale. This large uncertainty existed despite the two decimal place digital readout. This large uncertainty rendered it essentially useless for any information related to the saturation pressure of the water vapor. It was useful, however, to monitor the relative effectiveness of the vacuum pump, i.e. the condition of the lubrication oil, since the vacuum level would rise by up to 1.5 in-Hg when a change of oil was needed.

Element D was a 250 W, 120 V – AC, Ushio Halogen Projector Lamp. A copper tubing coil was fashioned to act as a spring to both support the lamp, which got very hot and to press it as close to the reservoir window as possible. The lamp itself, however, was held in an aluminum frame. The bolts of this frame kept about $\frac{1}{4}$ inch spacing from the window surface. This lack of thermal contact was instituted avoid excessive heat transfer to the vessel. In practice the vessel sometimes became hot to the touch. This issue is addressed in the Uncertainty and the Improvements sections.

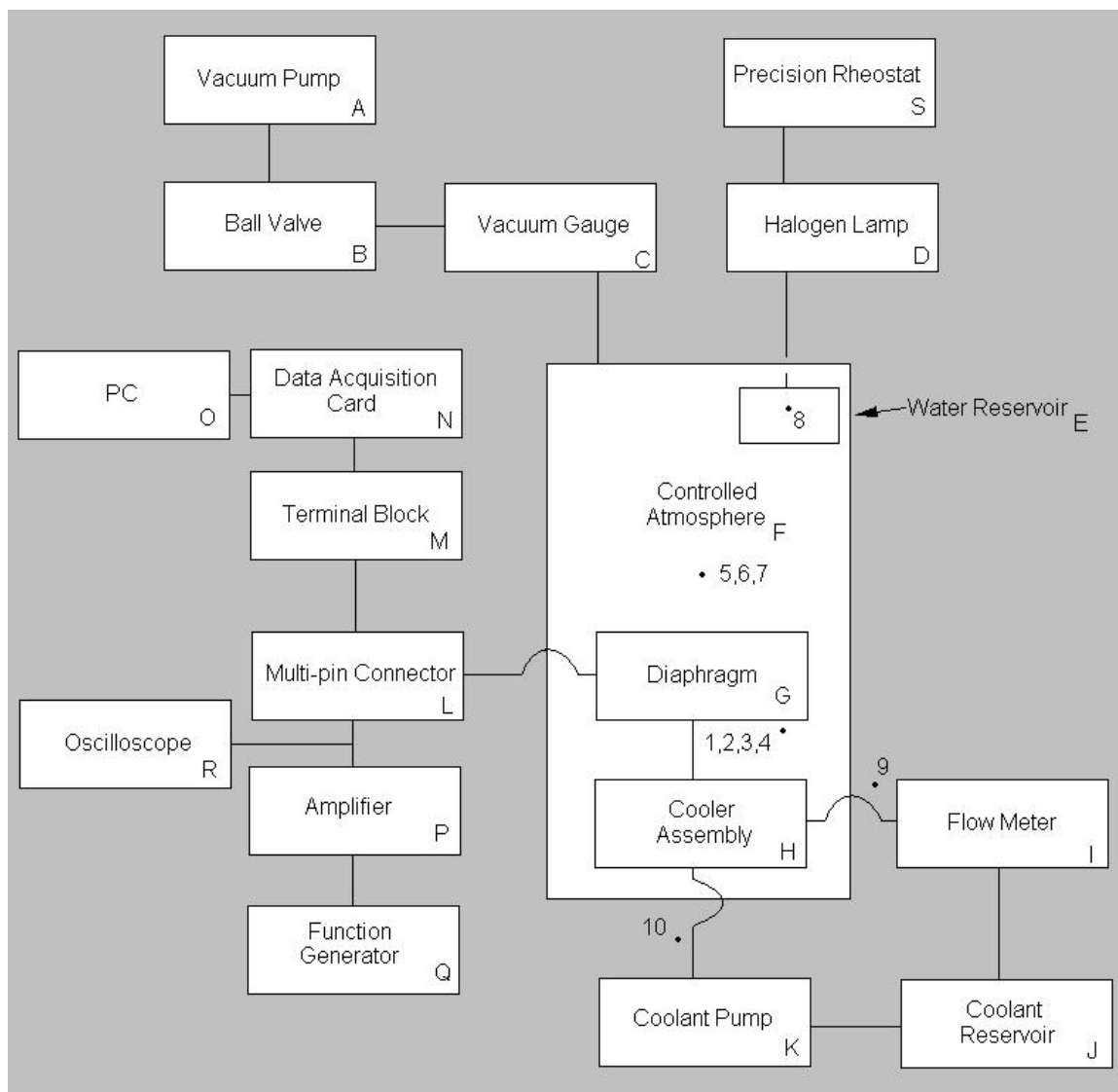


Figure 4-6. Schematic of equipment setup with labels.

Element E was the Water Reservoir, which was simply the window well on the bottom side of the four-windowed aluminum cylinder. Strips of aluminum were lined around the window well and the corresponding hole in the insulation sleeve using the silicone insulation as adhesive in order to increase the capacity of the reservoir to about 40 mL.

Element F was the Controlled Atmosphere of the vessel. Ideally this would be composed of pure water vapor, however, as the test results show, NCG was also a significant presence at times.

Element G was the piezoelectric Diaphragm. The supply of circular piezoelectric resonators, APC# FT-20T-3.6A1, was graciously supplied by American Piezo Corporation at no charge. The diameter of the brass shim to which the piezoelectric ceramic patch was attached was 0.004 inch (0.1 mm) thick and 0.75 inch (19 mm) in diameter. The positive and negative power lines both came through the multi-pin connector. The negative lead was hooked to essentially a washer on one of the bolts that held down the Diaphragm Clamp. The soldering of the positive lead onto silvered surface of the piezoelectric ceramic patch on the back of the diaphragm was a delicate operation. If the ceramic was heated by the soldering iron, or any source, above its critical temperature, it would lose its piezoelectric characteristics. Alternatively, the silver, electrically conductive backing might easily come off if over-heated. Only a minimal amount of solder was used to avoid extra mass loading of the vibrations. The soldering point was placed as far to the edge as possible for the same reason. Also, the soldered joint was covered with a thin later of JB Weld® epoxy, to physically secure the connection against vibration. It was necessary to be certain that the epoxy extended well onto the Teflon insulation of the power supply wire, or the very fine, 36 gauge wire used would often break at this exposed point. Also, for displacement measurements, a patch of metallic, reflective tape was placed on the back of the diaphragm so that it had sufficient reflectivity. About 1 mm of shoulder surface was required around the circumference to properly secure the diaphragm.

Element H was the Cooler Assembly, described in detail in the above section, fabricated in-house.

Element I was the analog, float-type Flow Meter, a King acrylic flow meter, 0.8 to 7 ± 0.1 gph. It was panel mounted on a piece of sheet metal on the table top, and vertical checked by a common level.

Element J was the Coolant Reservoir. This Rubbermaid Agricultural tank, of 60 gallon capacity was placed underneath the table supporting the experimental apparatus and equipment. Ice was placed here to both cool and, as it melted, supply feedwater to the coolant pump. Details about ice preparation were listed in Chapter 5.

Element K was the Coolant Pump, a Little Giant Pond Pump, 4300 gph, actually far oversized for this application.

Element L was the Multi-pin Connector, from Ceram-tec Products, a 19 pin, #16060-13-A, air-side plug/#16133-02-W single-ended receptacle. A flange held in place with epoxy and six stainless steel pan No. 8 pan head screws were used for attachment to the Bottom Cover.

Element M was the Terminal Block, from Measurement Computing, with 16 positive and negative posts for thermocouple attachment. Cold junction compensation done on-board with all terminals mounted on a single iso-thermal block. The block was designed to mate with Measurement Computing DAQ card.

Element N was the Data Acquisition Card, from Measurement Computing, part # PCI-DAS-TC, installed in a PCI slot of an IBM personal desktop. The card would support Labview, MSeExcel or MATLAB control, but Excel was chosen for convenience.

Element O was the desktop PC – IBM, Windows XP, in which the DAQ board was installed. Data was captured in Excel using DAS Wizard, supplied by Measurement Computing. All data was taken as a temperature reading, in °F, converted from voltage by the software. Each measurement represented 16 averaged values from in between sampling cycles. Sampling ranged from one per second to one per hour in increasing increments. Channels of the DAQ could be sampled individually or as a continuous set between two chosen limit terminals.

Element P was an Amplifier, made by Krohn Hite, model DCA-10, a wide band DC to 10 MHz amplifier with 1 and 10-times amplification, with continuously variable gain. This was the model recommended by the engineering staff of the driver manufacturer, APC.

Element Q was a Function Generator by B+K Precision, model 4017A, to 10 MHz with a sweep function. Only sinusoidal wave function was used.

Element R was an Oscilloscope by Tektronix, model 2247A, 100 MHz, with many functions, the most important of which were auto setup, to automatically find appropriate display settings for an applied input signal and a peak-to-peak voltage readout.

Element S was a Precision Rheostat from STACO, model # 3PN221B, with output range 0 – 132 V and up to 2.5 A, fused. This element was used to vary the input of the halogen lamp, especially necessary since, on the highest setting, smoke began to issue from the lamp area. Thus, the power was never set above 70%.

Elements 1 – 4 were the thermocouples used to measure the edge temperature of the diaphragm, whose placement was described in detail in the apparatus section above.

Elements 5 – 7 were the thermocouples used to measure atmospheric temperature.

Element 8 was the thermocouple used to measure liquid reservoir temperature.

Elements 9 & 10 were the thermocouples used for coolant outlet and inlet temperatures.

The following elements were not pictured for simplicity:

Element T was an Optical Displacement Sensor & Probe, from MTI Instruments, part number MTI-2000 Fotonic Sensor with MTI-2062H probe. This instrument used a broad spectrum halogen source lamp with precision input control along with a fiber optic cable to transmit the light to the sensor head. Half the fibers supplied the source light and half transmitted the light reflected from the source. There were two working ranges for each probe head design, on either side of an optical peak in captured, reflected light. The probe selected, in Range 1 used, had a standoff distance from the target of 0.76 mm with a range of ± 0.38 mm, with sensitivity of 0.12 $\mu\text{m}/\text{mV}$. Signal to Noise Ratio at resonance ranged in this study from a low of 13 for an old, used driver, to as high as 61 for a new driver. The resulting measured vibration amplitude, peak-to-peak measured had a minimum of about 7.5 μm , a maximum of about 38 μm and a noise equivalent to 0.6 μm . The main drawback to this instrument was that it required that reflective tape be placed on the back of the driver, for sufficient returned light. The problem then was that tiny air bubbles trapped under the tape would bubble up under the tape when the vessel was evacuated, thereby ruining the signal quality. No measurements of displacement were therefore possible during experimental runs. This data had to be inferred from a calibration curve constructed under atmospheric pressure. It could be expected that the vibration amplitude might slightly increase with less damping effect from air around it.

However, it was likely that the mass loading from the condensate on the driver surface would have a much more significant depressing effect on oscillation amplitude.

Element U was Camera 1, from JAI, model CV-730 color 770 x 500 CCD with a dedicated PC and controller card from Flashbus. This was the camera used for the initial and intermediate phases of experimentation.

Element V was Camera 2, the Motionscope from Redlake Imaging, with matching controller card and dedicated IBM – PC. This camera was capable of capturing up to 8000 frames per second. However, this frame rate required a massive light input to return a usable image and not enough light was available. Therefore a much slower frame rate was used. Some videos were taken at 50, 500, and 1000 frames per second, with good results. The frames from the final phase of testing were taken from videos captured with this camera.

Element W was the Heater Cartridge and Controller, from Watlow. A Firerod cartridge, 400 W and a Series 96 controller were taken from [89]. This heater was used in the initial stage of testing but was deemed ineffective and later removed.

Additional Testing

It was determined that the results of the data analysis warranted further clarification. This clarification would require slight modifications to the experimental apparatus (Figure 4-7). In this new setup, the fluid reservoir was separated from the test vessel, so as to isolate extraneous thermal energy conduction from the halogen lamp heating element to walls of the aluminum test vessel. Additionally, a phase separator, placed in an ice bath was added to the vacuum tubing arrangement between the vessel and the vacuum pump. This chilled separator would serve to minimize the amount of water vapor condensing in the oil of the vacuum pump by reducing the saturation

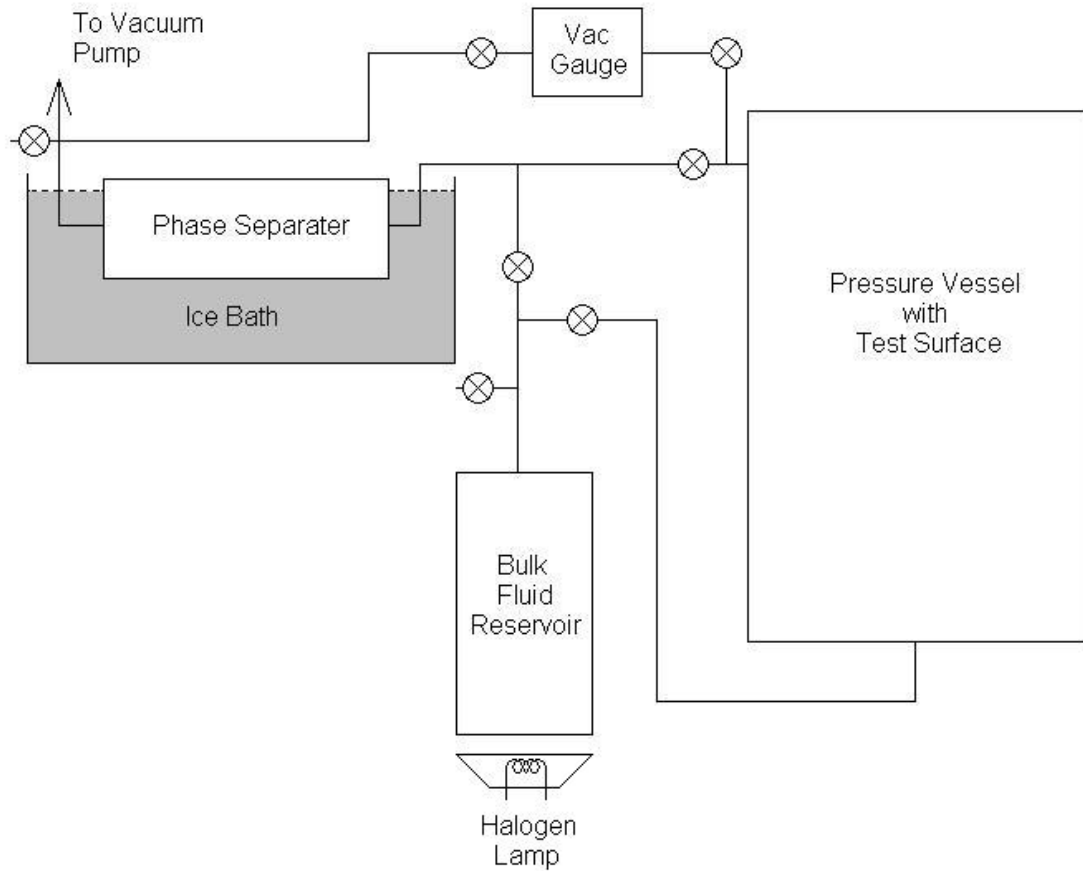


Figure 4-7. Schematic of vacuum apparatus adjustments for Additional Testing. temperature/pressure of the vapor being pulled through the tubing. This change improved the vacuum pump performance as well as the length of time that it could be operated without overheating, leading to better reduction of NCG in the test vessel environment. This arrangement was managed by inclusion of a series of manually operated ball valves, denoted in the figure by a standard valve symbol of a circle and an inscribed 'x'.

As an additional attempt to confirm assumptions of the theoretical analysis, three thermocouples were placed along a radial line of the brass shim (Figure 4-8). The same RTV silicone used elsewhere in the cell was used as an adhesive, with the thermocouple beads held in contact with the brass surface during application and curing. The positions

of the bead centers and corresponding uncertainties were then estimated from geometric analysis of digital photographs. The first thermocouple was centered within 4% of the radius of the center ($\pm 9\%$) while the second bead was centered at $33 \pm 13\%$ from the center, and the third at $66 \pm 9\%$ from the center.

For the additional testing, all thermocouples were replaced with type T, for its smaller absolute uncertainty. All these new thermocouples were Omega brand, made of 36 gauge wire. The part number of these thermocouples was 5TC-TT-36-36. They were all calibrated simultaneously to two laboratory-grade precision mercury thermometers.

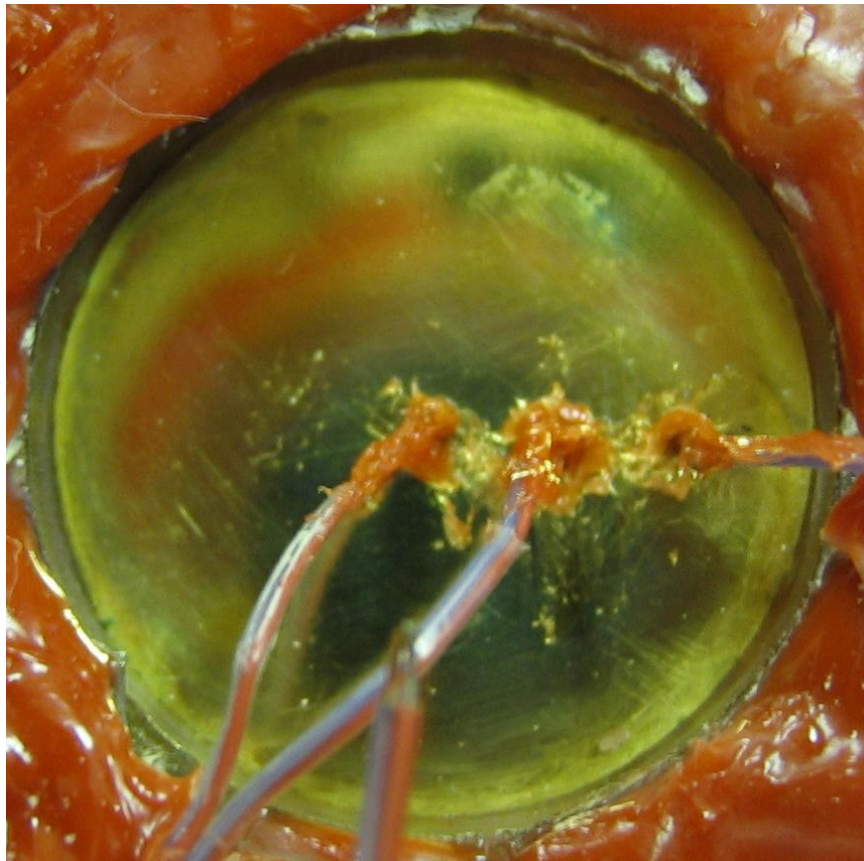


Figure 4-8. Placement of surface thermocouples on the piezoelectric diaphragm. Single thermocouple in foreground measured atmospheric temperature.

This step of direct surface temperature measurement was originally avoided due to concerns that the presence of the probes would interfere with the condensation

phenomenon taking place on the surface. However, the results of the Additional Testing proved to equal the best results of the previous testing in overall HT rate, indicating that any interference was negligible.

The atmospheric temperature estimate was now taken from a single thermocouple measurement instead of several, since the entire batch had been replaced with type T thermocouples. This new batch of thermocouples was calibrated together at a few dozen points across the full range of applicable temperatures. The calibration comparisons were two laboratory grade mercury thermometers with smallest divisions on their scales of 0.2 and 0.1°C. The calibration and expected maximum uncertainty in the readings were discussed in further detail in the Additional Testing section of Chapter 7.

CHAPTER 5 PROCEDURE

1. Prepare Coolant Reservoir.
 - a. Drain coolant reservoir level to just above the inlet of the pump, or to a depth of about 2 inch.
 - b. Add 100 to 150 lbs of ice was added.
 - i. If the pump was running, i.e. experiments being conducted, this amount of ice would last almost 6 hours. If the experiment was for some reason postponed, a usable portion of ice would still be in place some 12 hours later.
2. Clean diaphragm.
 - a. Clean diaphragm surface with a cotton swab lightly soaked in Brasso abrasive cleaner.
 - b. Wipe away residual material with two successive, dry cotton swabs.
 - i. Light pressure may be applied to scrub away any oxidation present on the diaphragm.
 - ii. Take care not to pull the diaphragm edges out of the clamp.
 - c. Clean diaphragm surface with a cotton swab lightly soaked in rubbing alcohol.
 - d. Wipe away any residual alcohol or debris remaining with two successive, dry cotton swabs.
3. Prepare working fluid reservoir.
 - a. Remove water in working fluid reservoir inside pressure vessel.
 - b. Clean reservoir with alcohol and a clean piece of cloth.
 - c. Refill reservoir with distilled water.
4. Insert Diaphragm, Cooler, Frame, and Bottom cover assembly into the insulation cylinder.

5. Test thermocouple and driver function, since connections were easily interruptible.
6. Secure bolts attaching Bottom Plate to the Aluminum Cylinder.
7. Re-test thermocouple and driver function.
8. General pressure gauge function:
 - a. Turn on, Allow reading to stabilize, ~ 1-2 min
 - b. Hit zero key, allow reading to stabilize, ~1-2 min
 - i. Gauge will stay on for 3 to 5 min. About 10-15 seconds prior to shut-off, the reading will spike a few percent. The shut-off is automatic.
 - ii. If further readings are desired after automatic shut-off, turn on again. Allow same stabilization period. Zeroing is not necessary again.
9. Evolution of evacuation process during experimental method development:
 - a. Cold evacuation, wait for equilibrium.
 - b. Cold evacuation, heat on.
 - c. Cold evacuation, heat on, evacuate again.
 - d. Hot evacuation, repeat if necessary.
 - e. Heat with open valve to near 170 or 180°F, then evacuate with heat on – generally acceptable results were obtained with this method.
10. Evacuate the pressure vessel.
11. Preheat vessel with open valve.
12. Turn on pressure gauge.
13. Adjust valves to desired arrangement.
14. Switch on vacuum pump for roughly five minutes.
15. Close off vessel before shutting off pump.
 - a. Take care not to leave vessel open to pressure gauge section, as the gauge itself leaks.

16. Vent vacuum line immediately after turning off pump or pump oil will be sucked into line.
17. Begin taking temperature data anytime before or during the evacuation process.
18. Close the coolant flow control valve.
19. Turn on power to coolant pump.
20. Slowly open the coolant flow control valve until it is fully open.
 - a. Allow any air trapped in the coolant line to escape through the flow-meter.
 - b. This process may be assisted by manipulating the coolant lines to allow the air pockets to rise in the fluid.
21. Adjust the flow rate down to the desired level.
 - a. Watch the coolant line connections for leaks.
22. Check flow rate every few minutes and adjust as necessary to maintain desired flow rate.
23. Continually check ice bath during experiment for:
 - a. Sufficient ice around pump inlet, stir reservoir if not.
 - b. Sufficient ice remains for continued testing, add as needed.
 - c. Inlet temperature was generally related to both of the above.
24. For test sections with vibrations:
 - a. Unhook driver cable from amplifier.
 - b. Turn on amplifier.
 - c. Switch selector to 10 x output.
 - d. Allow amplifier to stabilize for ~ 5 min.
 - e. Hook up driver cable to amplifier output.
 - f. Turn on function generator.
 - g. Select sinusoidal wave form.
 - h. Select 1-10 kHz frequency range.

- i. Turn the output knob completely counter-clockwise.
 - j. Turn on the Oscilloscope – set voltmeter function as peak-to-peak.
 - k. Adjust the amplitude on the function generator until the oscilloscope reads near 36.0 ± 0.4 Vp-p.
 - l. Tune in to resonant frequency of driver aurally. It will be readily apparent, even from inside the vessel
 - i. If you cannot easily hear the resonating driver, then there is a problem.
 - ii. Allow to run for a few minutes, to see if the problem corrects itself with a change in driver temperature.
 - iii. If not, then abort test and disassemble to determine trouble.
 - iv. Possible causes of weak or non-existent driver function:
 - 1. Loose connection at the multi-pin connector, vacuum side
 - 2. Soldering on positive power lead has come off the back of the driver.
 - 3. Thin wire portion of the driver supply line has broken
 - m. If you can easily pick out a range of resonant frequencies, continue.
 - n. Visually tune the frequency, to that range which minimizes the diameter of the residual drop or drops at the center of the vibrating diaphragm.
 - i. This range could be as much as ± 30 Hz.
 - ii. Closely monitor the resonance intensity of the diaphragm until edge temperature reading stabilizes.
 - 1. This precaution is necessary due to the temperature and also mass loading sensitivity of the resonant frequency of the piezoelectric diaphragm.
25. Several times per test session, when not at a change point in the data stream, interrupt data acquisition and save file, then re-commence DAQ operation.
26. When shutting down, no certain order is necessary, except to quit the DAQ program first.

CHAPTER 6 RESULTS AND DISCUSSION

Initial Testing

The experimental portion of this investigation developed in three stages. The first stage was the exploratory testing. In this phase, the coolant reservoir was at room-temperature, and the original heater (taken from a spray cooling study) [89] was the only heat source to the vessel. Evacuation was immediately followed by testing, or perhaps an hour delay was allowed for more evaporation of the fluid. Only about 5 mL of liquid was placed in the pressure vessel at this point. The orientation of the driver was horizontal. This orientation was only possible at steady state with VIDA, since something was required to clear away the condensate.

A comparison of video frames before and after the application of VIDA to a driver surface full of condensate demonstrated the ability of this process to effectively clear condensate (Figure 6-1). Clearly, the dropwise mode of condensation was underway on the diaphragm in the frame to the left, however, this amount of condensate had taken near ten minutes to build up. A few frames later, after the quasi-steady arrangement of droplets has set in for the VIDA section, it was apparent that the major drop sizes were much smaller. Unfortunately, with the coolant at room temperature, $\sim 24^{\circ}\text{C}$ (75°F) and the vapor temperature near 35°C (90°F) and the presence of NCG, which would not be identified until much later, there was not much HT going on. In fact, the ΔT across the cooler was drowned in the rather large uncertainty in this small heat rate, since heat rate was determined by the difference of two thermocouples at the coolant inlet and outlet.

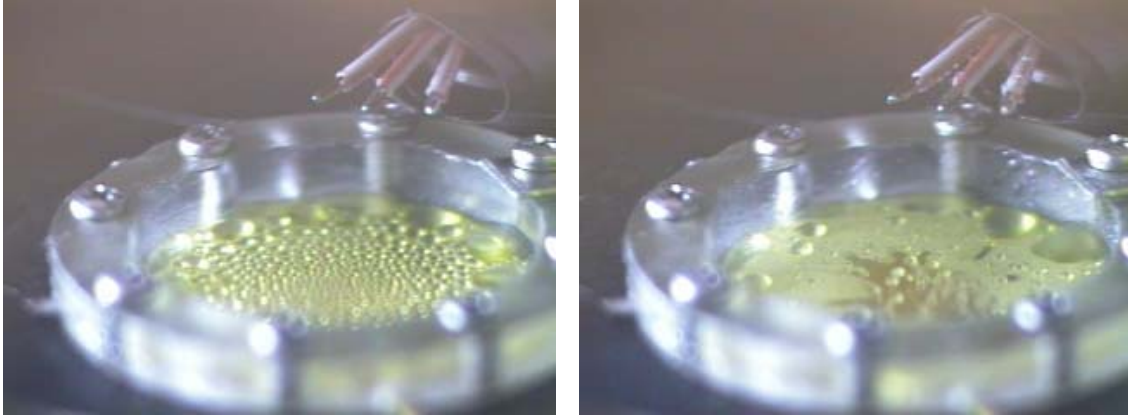


Figure 6-1. Video frames of DWC without (left) and with (right) VIDA. The fact that the coolant temp for the initial testing was about room temperature along with simple, cold evacuation being the only mode of removing NCG employed, the HT at this stage was negligible. Diaphragm orientation was horizontal.

Results of this first phase of testing originally focused on small, roughly ten minute windows, chosen for their low levels of oscillation in temperature reading, in pursuit of steady state readings. These data trends were in fact very flat, though this turned out to be due to a very low overall HT rate (Figure 6-2). At this point, the variation range in

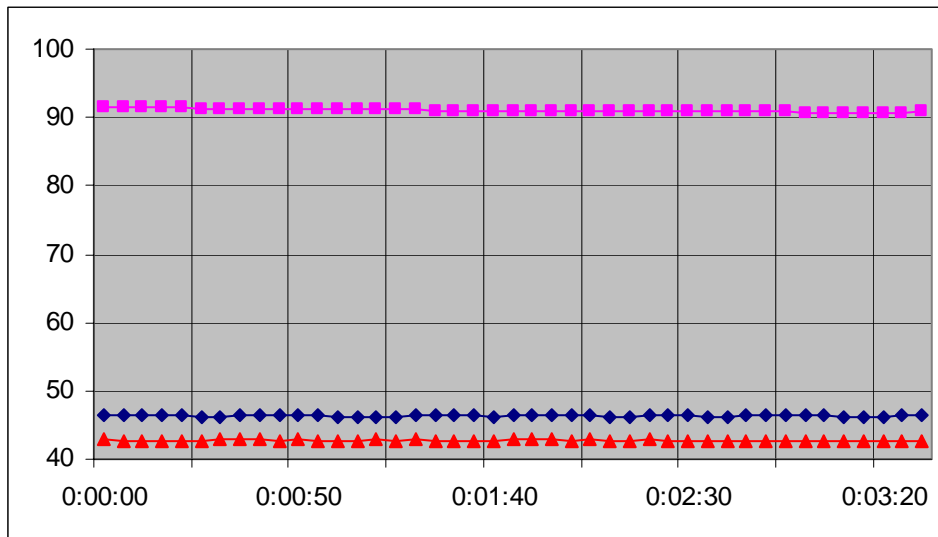


Figure 6-2. Temperature data from 1/26, in °F. Atmospheric temperature, T_{atm} , average edge temperature of the diaphragm, T_o , and coolant inlet temperature, T_{in} , respectively the highest, middle, and lowest readings. Readings were taken in °F over a 10 minute period at 5 second intervals.

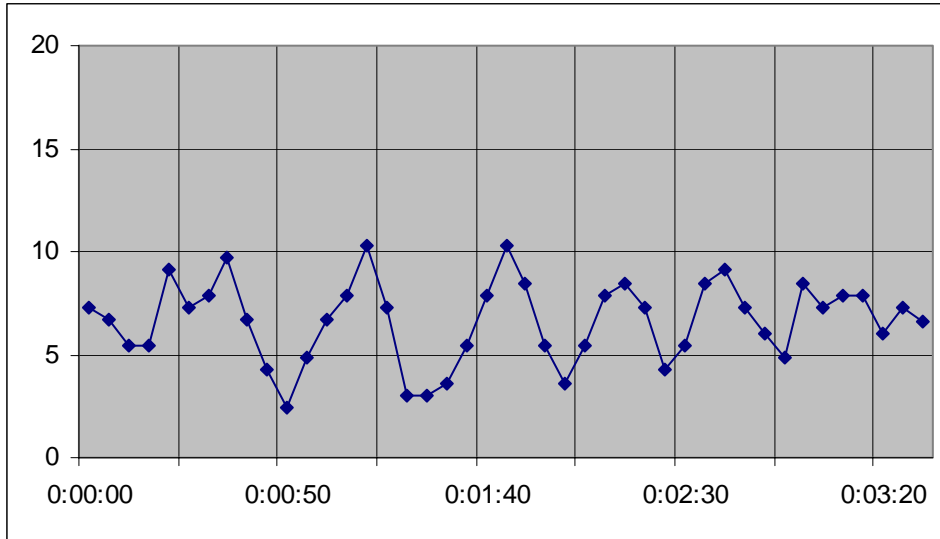


Figure 6-3. Total heat rate data from 1/26. Flow rate was 7.0 gph. No vibrations were applied to the diaphragm. THR was in W. The time interval between measurements was 5 seconds.

THR readings was almost 100% of the average reading (Figure 6-3). This situation arose from two things. First, the coolant flow rate was the highest available, 7.0 gph. Second, the THR was directly proportional to the small temperature difference between coolant inlet and outlet temperatures. The higher the coolant flow rate was, the higher the discretization error was relative to the overall reading because the measured temperature difference was smaller. It was hoped that this high flow rate, would help to get as close as possible to the ideal condition of a constant edge temperature for the diaphragm.

As yet, no difference between the vibration case and the non-vibration case was apparent. Steady state for HT transfer is the ideal condition, since this implies no temporal variation in total energy of the system. Thus the energy balance (Eq. 6-1) of the apparatus has one of the two unknowns reduced to zero. Then, since there was no significant source of energy generation within the control volume, the second unknown could be neglected. This left the heat input equal to the heat output. Therefore, the

measured heat output, THR, may be assumed to be made up exclusively of the energy input from the heater.

$$\dot{E}_{in} - \dot{E}_{out} + \dot{E}_{gen} = \frac{\Delta E_{CV}}{\Delta t}, \quad 6-1$$

Here ‘E’ stands for energy. The dot above represents time rate of change. ‘t’ refers to time. The subscript ‘in’ refers to inflow to the control volume, ‘out’ to outflow, and ‘gen’ to generation within the control volume – zero in this case. The ‘CV’ subscript referred to the control volume of the pressure vessel. Though this relation was not explicitly used in this investigation, it served to clarify that under steady state conditions, the only non-zero terms are E_{in} and E_{out} , the latter being measured and the former ignored. The important aspect here is that the ΔE_{CV} term does not contribute to the measured E_{out} and thus, it is assumed that all of the measured HT is due exclusively to the condensation occurring on the driver surface. The accuracy of this assumption will be addressed in the discussion of the results.

The temperature signal appeared relatively flat for the time period of display, which would be desirable as an indicator of steady state conditions, however, the THR was quite low, and on the order of the uncertainty in its reading. So it was determined that the likely limiting factor was the heater. An alternative arrangement was sought.

The design for the original heater, discussed in the apparatus section, had been taken from a study of spray cooling, and was thus ill-suited for this application. An ideal heater for a condensation study would supply vapor in a saturated state with no superheating, so that all HT would be involved in the heat of vaporization, although, for small superheats, the effect would be negligible. This would be best accomplished by submerging a heater in the liquid reservoir, as has been the case in every experimental

DWC HT study cited in the literature survey. However, this would have required a completely new heater design, further pressure vessel modifications, and new vacuum components, which would have been quite time consuming. So a method of heating was sought that would direct most or all of its thermal energy directly through the liquid reservoir while not requiring significant modification of the existing apparatus. A halogen lamp was placed below the window of the liquid reservoir. This would led into the second generation of the testing.

Intermediate Testing

All tests in this and the remaining phases were conducted with a vertical orientation for the condenser surface. After the heater was discovered as a major limiting factor in

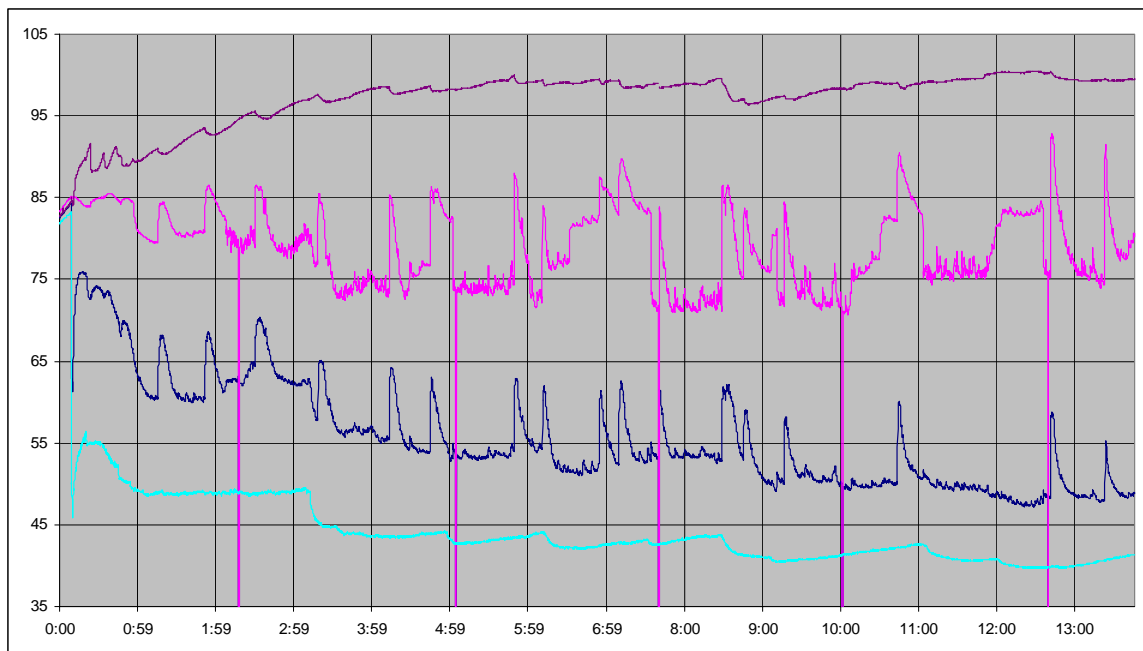


Figure 6-4. Temperature data from 2/17 in °F. The time scale is in hours:minutes. The data traces, from highest to lowest are T_{wall} – placed between the insulation and the vessel wall, at the top window well, T_{atm} – the atmospheric temperature, T_o – the average edge temperature of the diaphragm, and T_{in} – the inlet temperature of the coolant flow. Discontinuities in the T_{atm} measurements were artificially placed markers between input changes.

the HT process, it was replaced with an external, 50 W halogen lamp. At this point, there was no control on the lamp's input power. The early results during the intermediate phase of testing were characterized by wild fluctuations in both the atmospheric and the diaphragm edge temperatures (Figure 6-4). This variation, it was later discovered from the literature, is typical of condensation measurements in the presence of NCG [27,31,74].

A possible explanation then for these oscillations was a pocket of NCG collecting at the condenser surface, building up, and periodically departing. Condensation induces a net mass flow towards the condenser surface. When there are NCG molecules present in the vapor, they are swept toward the condenser surface with this flow. However, since the NCG molecules do not condense, they remain at the condenser surface and impede inflow of new molecules of the condensable vapor. Eventually, the concentration of NCG molecules becomes very high at the condenser surface, relative to that in the rest of the test vapor. This has the effect of insulating the condenser surface, allowing it to get colder than it otherwise would if fresh condensable vapor were supplied in excess. For a vertical condenser surface, this insulating effect eventually induces the mass of NCG collected at the condenser surface to be pulled away by buoyant forces. This leads to a sudden burst of warm, saturated vapor to the artificially chilled condenser surface, shown by an upward spike in temperature. This is exactly the behavior shown in the temperature charts (Figure 6-4). Corresponding spikes in THR were also shown by the data (Figure 6-5). A detailed account of the justification for this conclusion follows:

- Periodic temperature and THR spikes corresponded with each other and therefore were not due to instrument error. THR was a differential measurement and the other temperatures were individual measurements. Therefore any group upswing in

reading would not have registered on the THR, as it would have equally affected both thermocouples.

- Spikes did not correspond to changes in any of the control parameters of the experiment, those being heat input, coolant flow-rate, or presence of vibration.
- Over the 14 hours of this test, 7 different flow rates were sequentially tested for half of that flow-rate period with the vibrating driver and half without. The lengths of successive flow-rate sections were more or less equal, at about one half hour each. Changes in flow rate roughly corresponded to the corners in the coolant inlet temperature graph.

No effect of vibration was apparent in the DWC HT from these results.

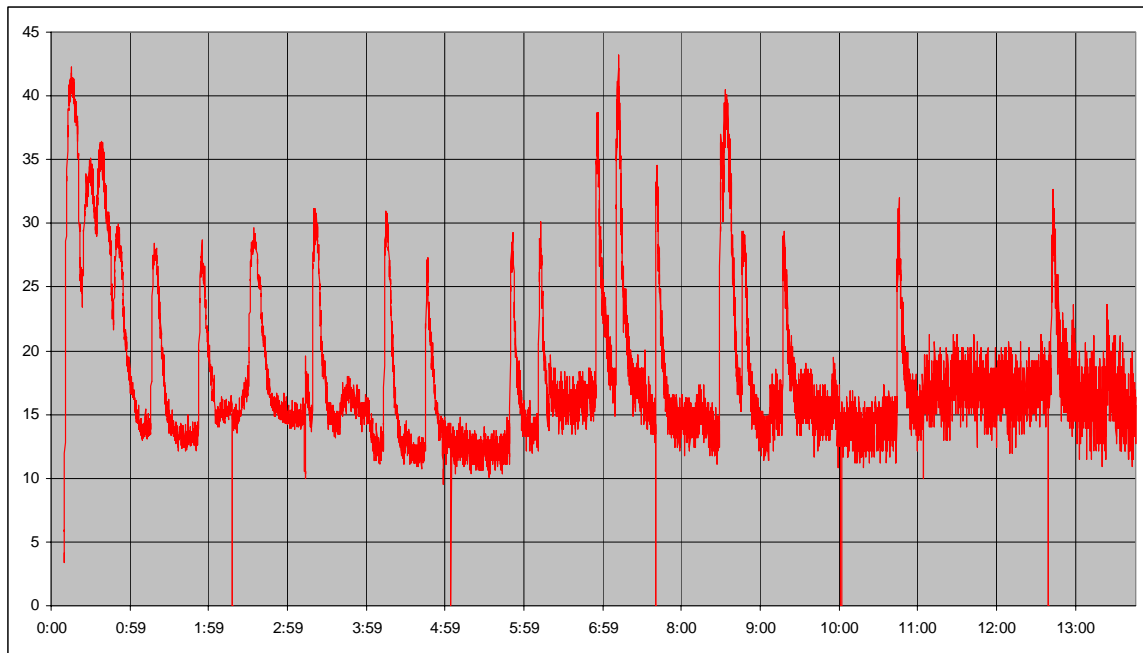


Figure 6-5. Total heat rate data from 2/17 in W. Time scale is in hours:minutes. During this run, 7 different flow rates were tested, beginning at 1.0 gph and increasing in 6 steps to 7.0 gph. At each level of flow rate, conditions were monitored with and without the driver vibrating. Each flow rate stage was held for about 2 hours and was evenly divided between vibration conditions. The spikes in THR did not correspond to changes in the experimental conditions and were thus attributed to the effects of NCG.

The downward trend in T_o and T_{in} was due to the flow rate changes (Figure 6-4).

For the lower flow rates, the coolant moved through the feed tubes more slowly and therefore had more time to absorb heat from its environment prior to arriving at the test

vessel, despite attempts at insulation. This external heating led to lower inlet temperatures for higher flow rates, moving from about 38 to 40°F for 7.0 gph to near 50°F for 1.0 gph. Since this was the heat sink temperature, the rest of the temperatures of cell were correspondingly shifted up for a given increase in T_{in} .

Another temporal trend was apparent in the wall temperature reading. The first 4 hours showed some thermal capacitance as the apparatus heated up. As far as the energy balance and THR readings go, this could be ignored, since the energy balance was not being monitored and the addition of thermal energy here was positive. If the addition were negative – that is the apparatus were experiencing a net cooling – then this would imply that the heat being absorbed by the coolant included thermal energy from the vessel itself, instead of only the condensation phenomenon. However, as long as the apparatus temperature was increasing or steady, the trend could be safely ignored.

The visual record of the 2/17 test, in the intermediate phase of testing showed partial DWC (Figure 6-6). This test occurred before the cleaning regimen of Chapter 5

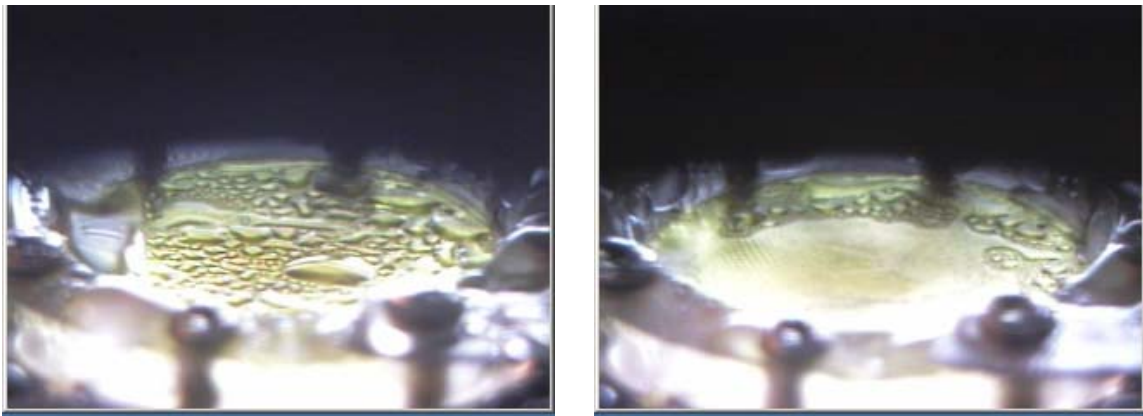


Figure 6-6. Two frames taken from videos on 2/17, showing condensation without vibration (left) and with vibration (right). The cleaning regimen had been delayed for a few days to try to induce FWC, which only resulted under conditions of vibration. Though not visible in the right hand side picture, droplets were continuously being ejected from the film. Down was to the left.

was established. This partial DWC was the result of the driver surface being allowed to tarnish over several days. The frame on the left shows condensation progressing on a quiescent diaphragm. The frame on the right shows the result of the same parameter set except for the application of VIDA. Curiously, the quiescent mode of condensation remained mostly dropwise although the drop edges were more irregular. However, under imposed vibrations at the resonance frequency of the diaphragm, a film formed on the center of the driver. Unfortunately, the 30 fps frame rate of the camera used here was insufficient to capture the continuous ejection of droplets from this liquid film. A wave pattern is slightly noticeable on the lower portion of the right picture, as evidence of existent capillary waves. These waves were constantly ejecting droplets, as per the description of Vukasinovic [10] of VIDA. The data from this set were determined not worthy of comparison as filmwise mode to other data, since the NCG presence was still far from under control.

At this early portion of the intermediate phase of testing, the data was still only being examined in small – 10 minute – chunks, so the overall variation (Figure 6-4) was not yet apparent. The portions of data without spikes were simply selected for analysis. THR values were still considered low at this point, and though this was later proved true, it was not yet based on a theoretical model. The theoretical model was quite unfortunately constructed after the conclusion of experimental work, since a method of modeling had not yet to been found.

In the latter portion of the intermediate testing phase, a concerted effort at reaching steady state conditions was finally undertaken. For the remainder of the tests, the thermocouple between the wall and the insulation was moved to the liquid reservoir, in

order to make comparisons between this temperature and the atmospheric temperature.

The relation between these two temperatures was then used to infer the saturation state of the vapor. The remainder of the tests were conducted for durations of 10 to 18 hours with only a few experimental conditions examined, in order to more accurately pursue and evaluate the steady state condition of the variables. Also for this and further tests, the diaphragm was cleaned with the regimen described in the PROCEDURE section just prior to commencing each day's experiment.

The temperature data from 2/24 (Figure 6-7) showed a gradual increase in the liquid temperature (T_{liq}) and T_{atm} . These two values also maintained a near constant difference between them. This apparent increase in the thermal energy of the hot side of the vessel will be ignored in relation to steady state of the apparatus for reasons discussed above. However the concept of warm vessel wall has potential for parasitic heat transfer

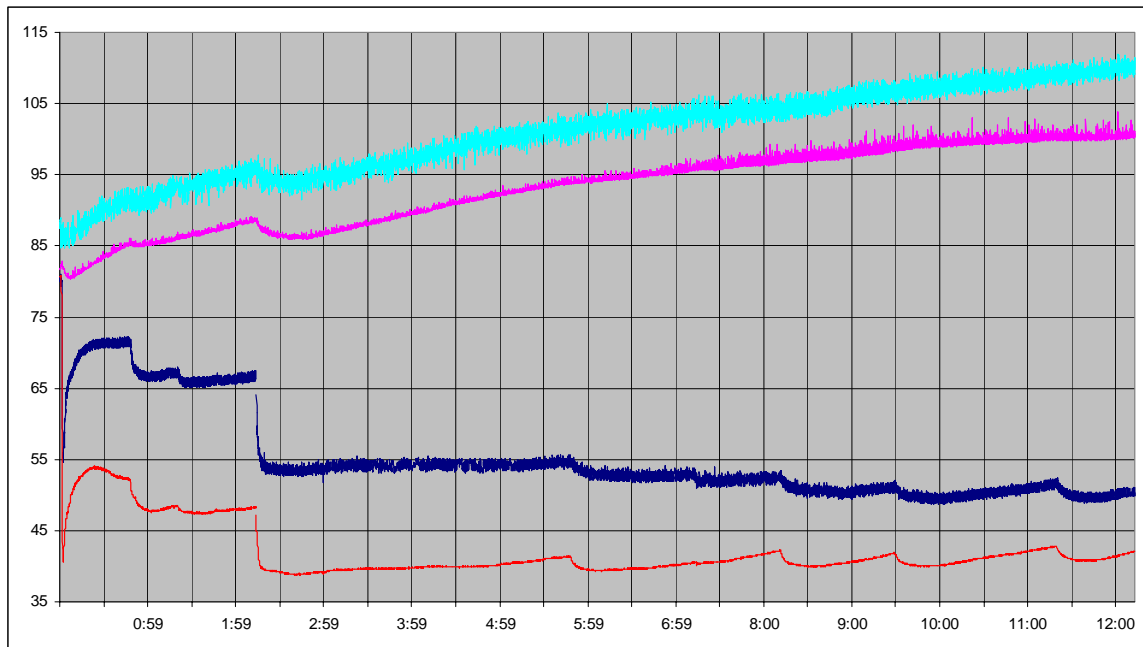


Figure 6-7. Temperature data from 2/24, in °F. Time scale is in hours:minutes. Values are, in decreasing order, T_{liq} , reservoir temperature, T_{atm} , atmospheric temperature, T_o , average edge temperature, and T_{in} , coolant inlet temperature.

to the cooler, through the insulation sleeve. This potential error was addressed later in this chapter.

After an initial test period at 1.0 gph, coolant flowrate was increased to 7.0 gph and held there for the remainder of the test. A constant inlet condition was difficult to maintain. This fact was firstly due to the non-uniform melting of the ice in the reservoir. The pump was the primary heat load in the reservoir and so melted the ice immediately around it much faster than the rest. Variations in pump performance with supply voltage were also responsible for inlet temperature fluctuations. Also, small air bubbles or pieces of debris in the coolant flow at times became lodged in the flowmeter valve or otherwise restricted flow, thereby causing the equilibrium inlet temperature to change. These are the sources for the corners apparent in the T_{in} data later than 3 hours into the test.

Possible direct evidence of vibration improving HT was found at 7:15 (Figure 6-7). A slight drop in T_o was noted here, which corresponded directly to the vibration being turned off and a slight drop in measured THR. While other noticeable drops in T_o are present in the data record, they each corresponded to an adjustment in the coolant flowrate and therefore a drop in sink temperature. This pairing was readily apparent in the temperature graph. The net effect, however, was slight, and will be discussed further in the next section.

Another trend of note was apparent in the gradually decreasing T_o relative to T_{in} and the corresponding gradual drop in measured THR. This would later be explained by an air leak introducing more NCG to apparatus with time. As compared to the 2/17 test, the NCG concentration is assumed less in this test, due to the lack of chaotic temperature of THR swings (Figure 6-8). The remaining variation was due primarily to uncertainty in

the temperature measurements and the data acquisition system, since this value was based on the differential reading between two thermocouples. This uncertainty was higher for a higher flow-rate, this data being taken at the maximum 7.0 gph, since the temperature difference encountered by a fluid flowing faster through the cooler was smaller than for slower transit. The tradeoff of lower uncertainty, however, was not deemed justifiable in light of the incurred higher sink temperature inherent in using a lower flow rate.

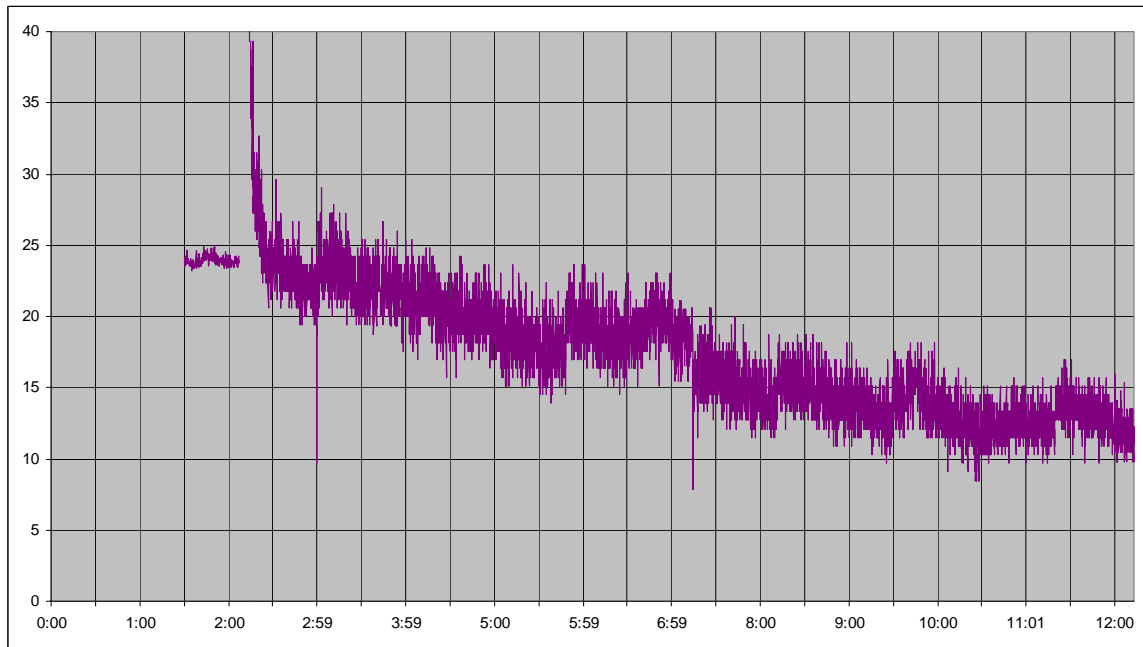


Figure 6-8. Total heat rate data from 2/24, in W. Time scale in hours:minutes. Note the gradual decrease in THR for increasing time and the disjoint at 7:15, deemed possible evidence of vibration increasing HT.

Later tests in the intermediate phase also saw the additional insulation discussed in the apparatus section, visible as the orange colored area in the foreground (Figure 6-9). These photos were taken from the same oblique angle as the first schematic of the apparatus (Figure 4-1). Focus and field of view were difficult to work with at this angle and for this geometry, so the picture quality was not optimal, but the main patterns of DWC are nonetheless apparent.

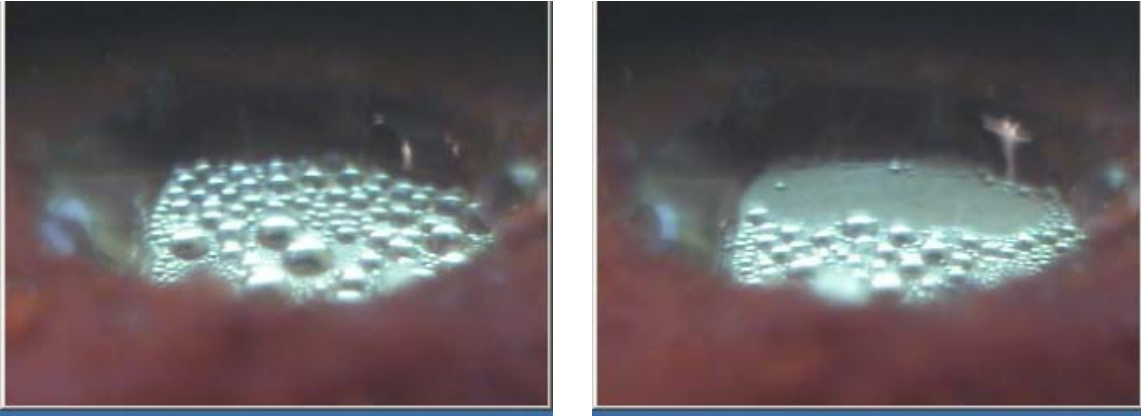


Figure 6-9. Typical droplet distribution for DWC on the test diaphragm without VIDA, prior to departure (left) and after departure of a large drop (right). Down was to the left.

Graphical estimations showed a maximum droplet radius for this photo of 1.05 ± 0.18 mm. This result was well in line with the Rose estimation of maximum drop size (Eq. 2-11) for this temperature range. The final section in this chapter compared the measured THR to that predicted by the Rose theory for this diaphragm. The theoretical analysis included an effective maximum droplet radius.

The maximum drop size under conditions of vibration (Figure 6-10) was much smaller than without applied vibration (Figure 6-9). It was expected that this lowering of

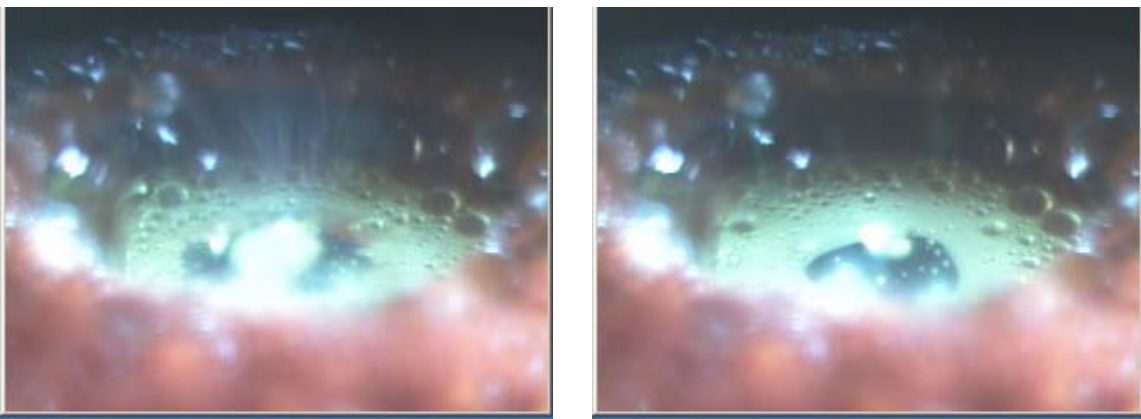


Figure 6-10. Video frames of typical droplet distribution for DWC with VIDA. A droplet during the process of bursting (left) and after (right). Down is to the left.

the maximum drop size would increase the overall heat transfer, though only slight evidence of this was noted in the experimental run of 2/24.

Two factors in this arrangement likely served to mitigate the potential HT gains from the apparent decrease in maximum drop size. First, maximum droplet size around the edges of the diaphragm was still on the same order as the non-vibration case. And since the edge was where most of the HT took place (Figure 3-2), the same level of HT was expected. Second, NCG presence in the test vessel had yet to be sufficiently controlled. The decline of THR with time indicated a leak in the pressure vessel, since this behavior stopped when the seals were better controlled. Also, THR was relatively low compared to theoretical estimates, presented later in this chapter.

Final Testing

Efforts to purge NCG from the vessel became more effective in the third and final stage of experiments. Multi-stage evacuations and heating times were instituted, eventually leading to the process described in PROCEDURE for the final two days of testing, which yielded the highest THR values of the entire study. The resulting data now warranted a close look at the relative behavior of T_{liq} and T_{atm} .

The test data from 3/4 clearly demonstrated the effect of NCG on DWC in the HT cell (Figure 6-11). From time 0 to about 50 minutes, the vessel was heating up, after evacuation, with no coolant flow. Following an evacuation ending just after the 1 hour mark, where all the temperatures run together, another heating period ensues. At about 2:40, the coolant flow was started and T_{in} drops almost immediately to relatively steady value. From the gradually increasing difference between T_{atm} and T_{liq} , with the former dropping and the latter rising, an air leak in the vessel is apparent. The effect of air here to raise the was liquid temperature while depressing T_{atm} , T_o , and consequently THR.

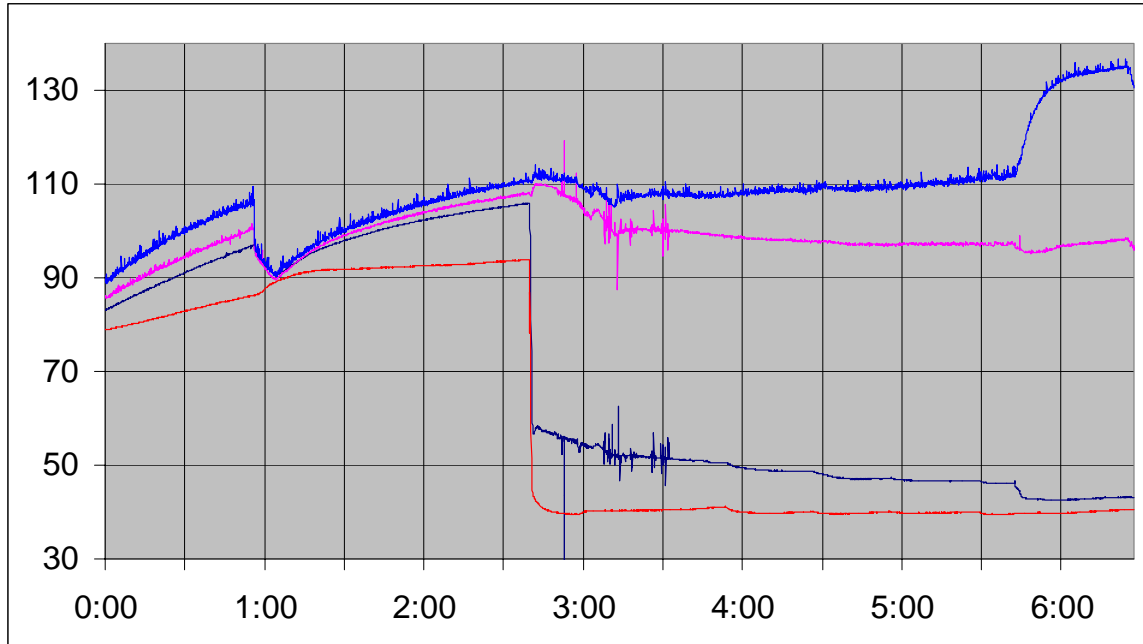


Figure 6-11. Temperature data from 3/4, in °F. Time in hours:minutes. Values from high to low are T_{liq} – liquid reservoir temperature, T_{atm} – atmospheric temperature in vessel, T_o – averaged diaphragm edge temperature, and T_{in} , coolant inlet temperature.

This effect is unquestionably demonstrated when, at about 5:40, the vessel is accidentally vented to 1 atm. With no change to the control parameters, coolant flow-rate, T_{in} , or the lamp power, T_{liq} rose 25°F in about 15 min while the boiling that had been fairly vigorous prior to venting immediately ceased. Simultaneously T_{atm} and T_o drop a few degrees and THR drops about 30% (Figure 6-12). Additional support for this NCG effect conclusion was the fact that during an evacuation process, even though the high temperatures dropped significantly, the THR always peaked significantly at the same time.

This precipitous drop in HT clearly indicated that the suppressive effect of NCG on DWC in this HT cell greatly overshadowed the anticipated improvements of VIDA. This accident clearly demonstrated the importance of the NCG effect, which was then researched in earnest. New effort was applied to making good seals at every possible

leak point in the vessel. Dow Corning high vacuum grease was liberally applied to all soft and hard seals. This turned out to be even worse, but after the excess grease was removed, the result was much better than the original dry arrangement. Data from the next experiment, 3/7, showed a much closer and temporally stable relationship between T_{atm} and T_{liq} .

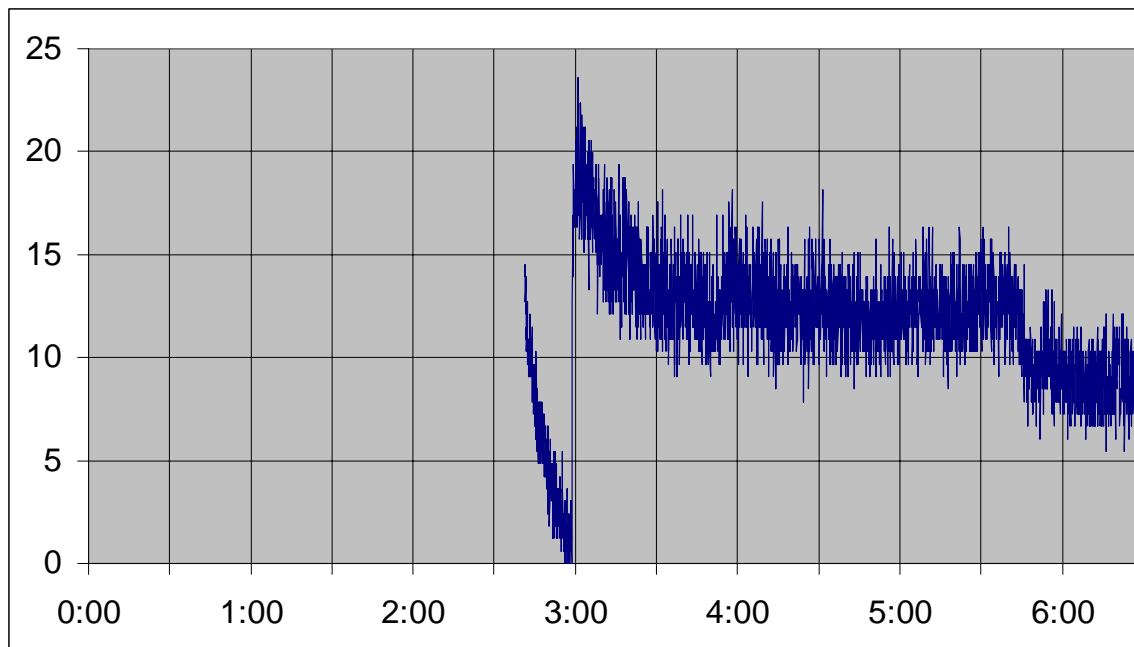


Figure 6-12. Total heat rate data from 3/4, in W. Note the drop at 5:40, which was due to accidental venting of the vessel to 1 atm. The low readings before 3:00 were fluctuations associated with establishing steady state after turning on the coolant flow.

The seal situation on 3/7 was not perfect. Fortunately, a problem with thermocouple deterioration required re-wiring of the multi-pin connector and replacement of the soft seal. This activity apparently fixed the leak, to the extent possible with the current apparatus. All subsequent experiments, from 3/8 through 3/15-16 showed a very close relation between T_{liq} and T_{atm} , indicating a very low presence of NCG.

Next the 50 W lamp was replaced with a 250 W lamp. A precision rheostat was added to control the input voltage to the lamp. Superheating of the vapor was noted after

this addition. This new phenomenon was attributed to the significant heating of the vessel walls from the new, more powerful lamp. This also raised the possibility of parasitic HT from the walls of the vessel directly to the cooler, through the insulation sleeve, see Chapter 7.

The last three days of experiments in the Final Testing phase were the best with respect to elimination of NCG. However some small effects of NCG were still noted. No dramatic improvement in HT due to the application of vibration was readily apparent from the graphic displays of this data. The major events marking the data of 3/13 were the initial heating period, followed by coolant flow commencement at 1:20, and evacuations at 2:00, 6:30, and 9:00 (Figure 6-13). The power supply to the lamp was

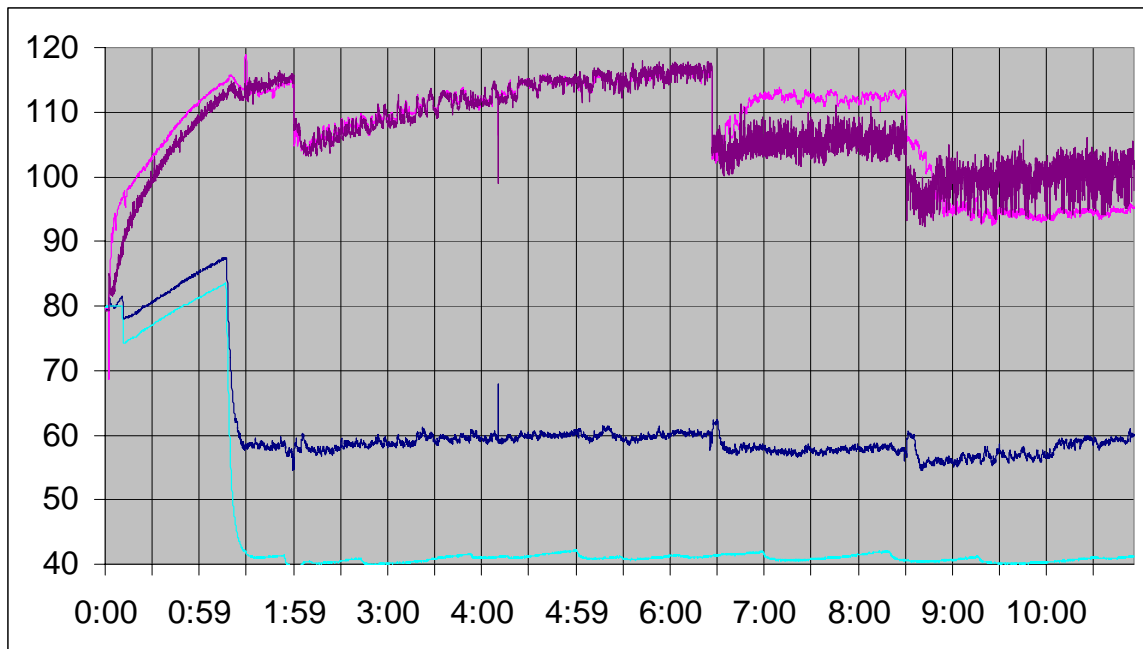


Figure 6-13. Temperature data from 3/13, in °F. Time in hours:min. The two highest readings are T_{atm} and T_{liq} , which tracked quite closely once the NCG presence in the apparatus had been better controlled. Between 6:30 and 9:00, T_{atm} is actually higher than T_{liq} , then it drops below it after the heat input was reduced 10%. T_{liq} , the liquid reservoir temperature, T_{atm} , the atmospheric temperature in the vessel, T_o , the averaged edge temperature, lying in at the middle value, and T_{in} , the coolant inlet temperature.

kept at 70% until 9:00, when it was switched to 60%, in an effort to reduce the superheat seen between 6:30 and 9:00. The desired effect was achieved. The presence of superheat in the second stage but not the first may be explained as an effect of vibration, since the driver was turned off at 6:30. That is, evaporation of spray from the VIDA most likely counteracted that tendency to of the vapor to develop superheat. Curiously, the THR was actually higher in the region with superheat (i.e., without vibration) (Figure 6-14), even though the T_{atm} was higher in the case with vibration.

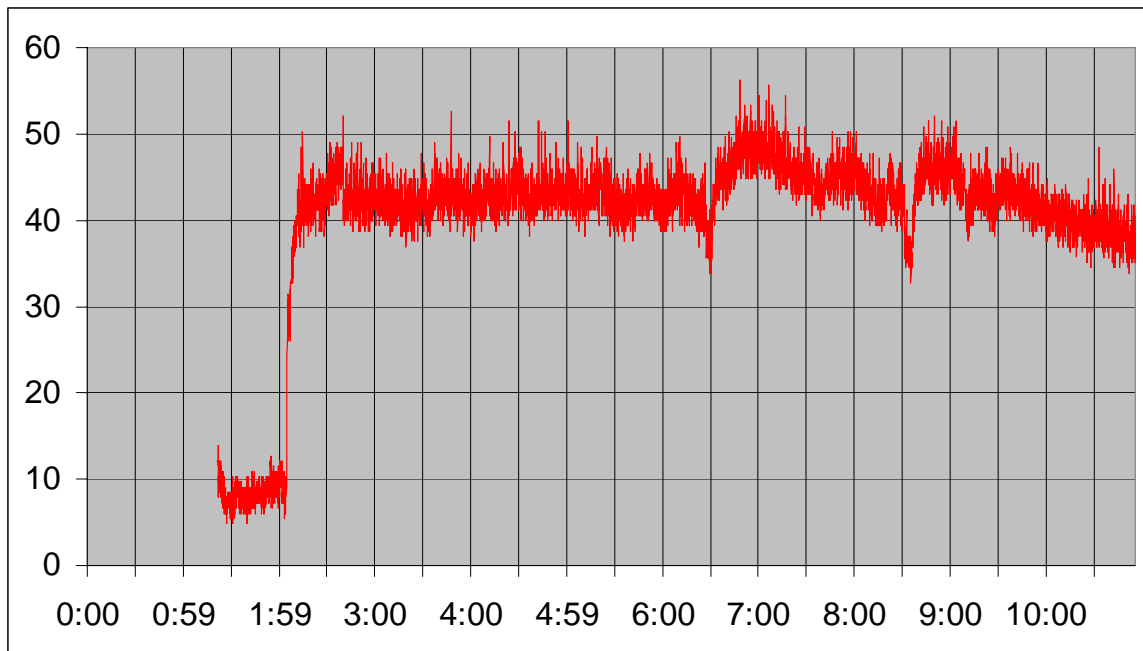


Figure 6-14. Total heat rate data from 3/13, in W. Time in hours:minutes. Low initial readings due to start-up transients and fluctuations in coolant flow rate.

This discrepancy of higher HT with lower T_{atm} and no vibration was not immediately explained. However, one possibility was that evacuation temporarily improved HT, an effect that was seen more dramatically under the effects of NCG. It should also be noted that this increase in HT with a decrease in pressure would stand to go against the Rose theory's predictions of decreasing HTC with pressure. A possible reason for the increase in HT with evacuation may be the inducement of mixing in the

vessel atmosphere assisting the diffusive process of vapor moving towards the condenser surface as well as removing a portion of the NCG present.

The experiments of the next day (3/14) showed excellent steady state characteristics (Figure 6-15). This was probably due to the lower power level used, 60%. There was still a general heating trend of the atmosphere, but the increase was small compared to others. The only effect of VIDA visible in these results was to slightly increase the difference between the average T_{liq} and T_{atm} . The difference however was barely noticeable from 1:00 to 4:00, 7:00 to 8:00, and 10:15 to the close of the experiment.

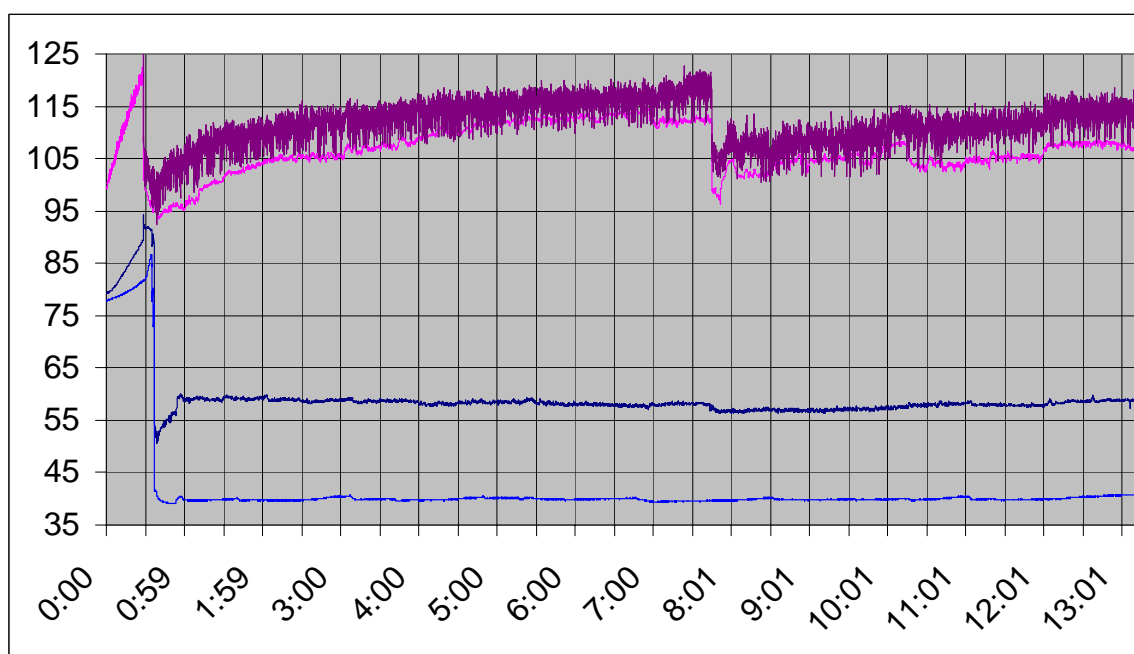


Figure 6-15. Temperature data from 3/14, in °F. Time in hours:minutes. T_{liq} was the highest and most variant value, due to the boiling process. T_{atm} , the atmospheric temperature, was just beneath it and at times indistinguishable. T_{avg} was the averaged edge temperature, which hovered around 56-57. T_{in} was the coolant inlet temperature, the lowest value shown.

The THR values (Figure 6-16) showed only a marginal change due to the application of VIDA. The times of these changes were noted in the above paragraph.

The evacuation process, in fact, shows a much more significant and consistent effect on THR, as can be seen as an increase near 8:00.

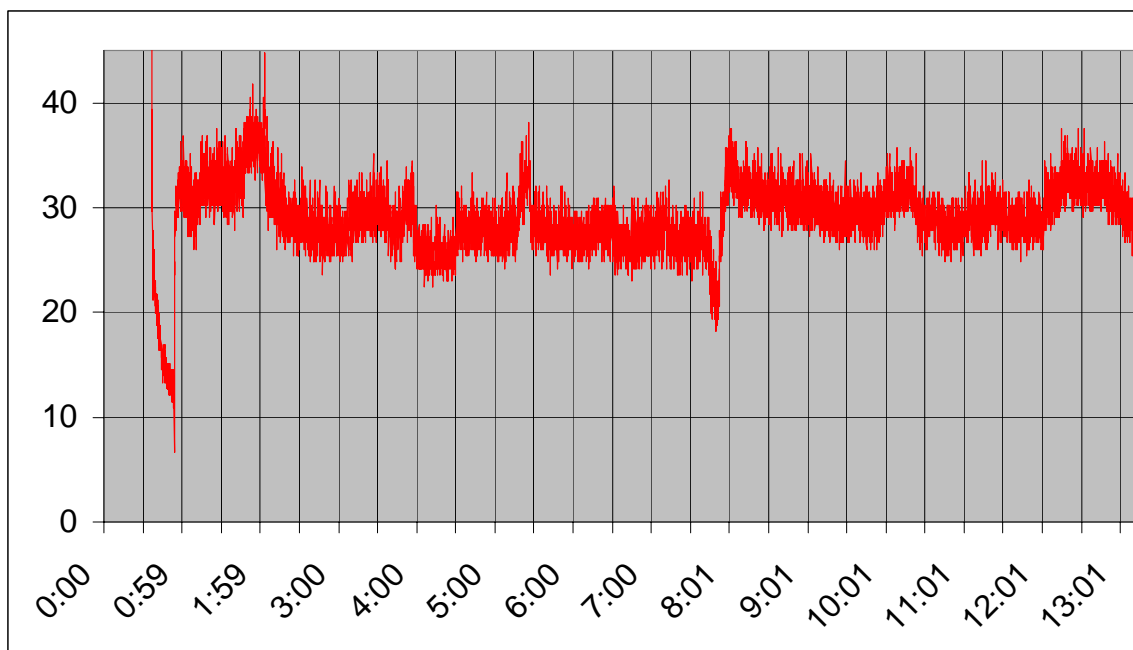


Figure 6-16. Total heat rate data from 3/14. Data were in W. Time was in hours:minutes. Only marginal differences appeared for the application of VIDA to DWC. The largest jump shown is due to evacuating the vessel at 8:00.

The third and final day of testing (3/15-16) also failed to show a dramatic impact of VIDA on HT (Figure 6-17). The first section of the test, from 2:00 to 12:00, was run with 50% power setting to the light. It should be noted that no attempt was made to quantify the heat input from the light and the percentage input values should merely be taken as relative. The VIDA was switched on a little before 9:00. Consequently, the gap between T_{atm} and T_{liq} shrank a little. However, this gap could also be seen to grow with time prior to that period. This observation coupled with the downward trend in THR with time (Figure 6-18) indicated an air leak in the installation of this day. The effects of this leak, however, were small, since the ΔT_{atm} remained small (less than a few degrees), especially close to the evacuations at 1:30 and 12:00. Actually, after the readings dip

near 17:00, due to a heat shut down rather than an evacuation as has been seen before, the vapor became superheated by a few °F for the remainder of the test.

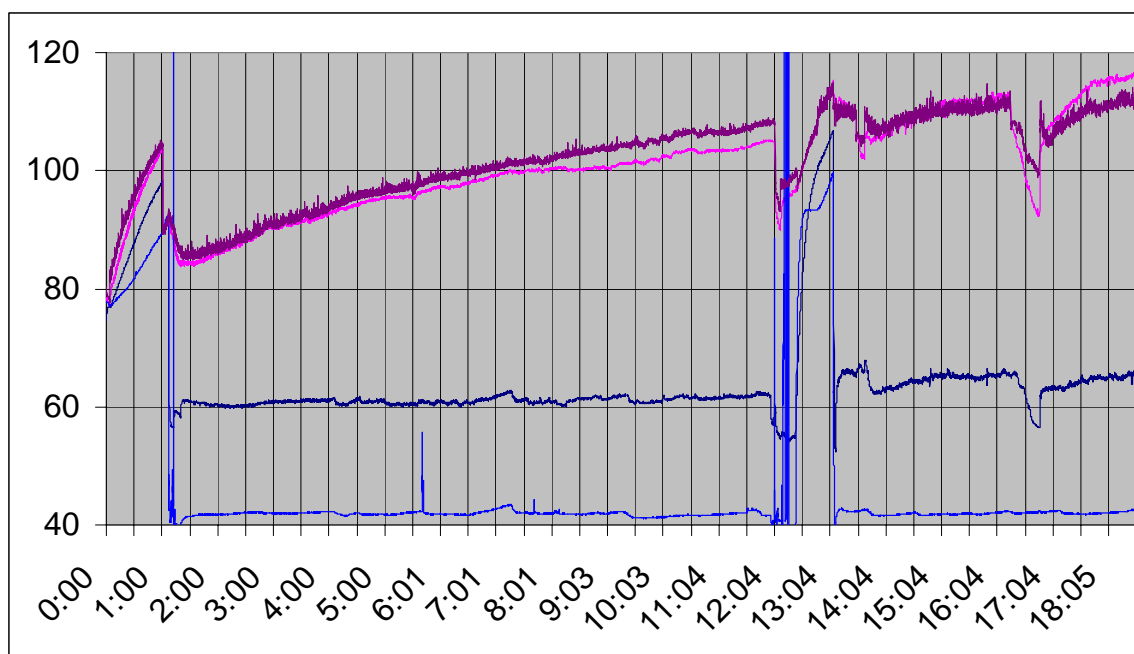


Figure 6-17. Temperature data from 3/15-16. Data in °F. Time in hours:minutes. T_{liq} – liquid reservoir temperature is the more variant of the two higher temperatures. T_{atm} – the temperature of the atmosphere on the hot side of the vessel, is the less variant of the two higher temperatures. T_o – the averaged edge temperature of the diaphragm, is the middle temperature value. T_{in} – coolant inlet temperature, is the lowest reading. The flow-rate was 3.0 gph.

In discussing the THR data of 3/15 (Figure 6-18), it should be noted that the first portion of this test was run with 50% input to the heater/lamp and the second portion, after the discontinuity, at 70%. Fifty percent input yields about 30 W, 60% input yields about 40 W, and 70% input yields over 50 W, which makes sense when considered in the context of an energy balance. It also would seem to highlight the fact that input power was generally held constant and excess steam supplied to the condenser surface in most experimental studies of DWC. Such an arrangement would therefore be preferred for comparability of data in the future.

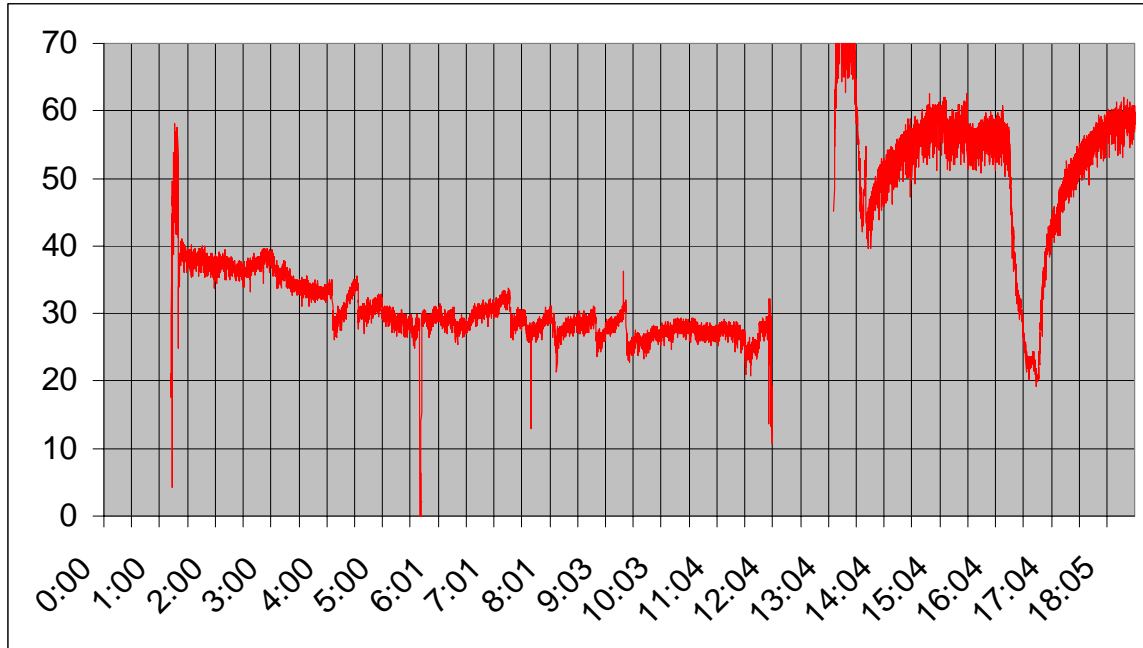


Figure 6-18. Total heat rate data from 3/15-16. Data was in W. Note the gradual decrease in THR between the first and second evacuation (1:45 and 12:00), a period of relatively constant input parameters. This indicated a probable air leak in the vessel.

The quality of DWC on the diaphragm surface was good (Figure 6-19). The droplet size distribution and appearance was qualitatively typical of those shown in [19, 28,55]. A common description of DWC condensation was an array of drops of different sizes that were arranged in a self-similar pattern at different magnifications. Following a departed drop may provide some insight to the origin and maintenance of this pattern. As a newly departed drop swept down the surface, it absorbed all the smaller drops in its path. Once the falling drop had passed, a clean, bare metal surface was left in its path. Small drops were then seen to be in the bare path. They quickly began to coalesce as they grew enough to touch each other. The coalescence was visible as a flashing, when new, bare condenser surface was exposed after a smaller drop was absorbed into a bigger one. Eventually, these drops neared the size of the neighboring drops and the swept path of the fallen drop became indistinguishable from the areas around it.

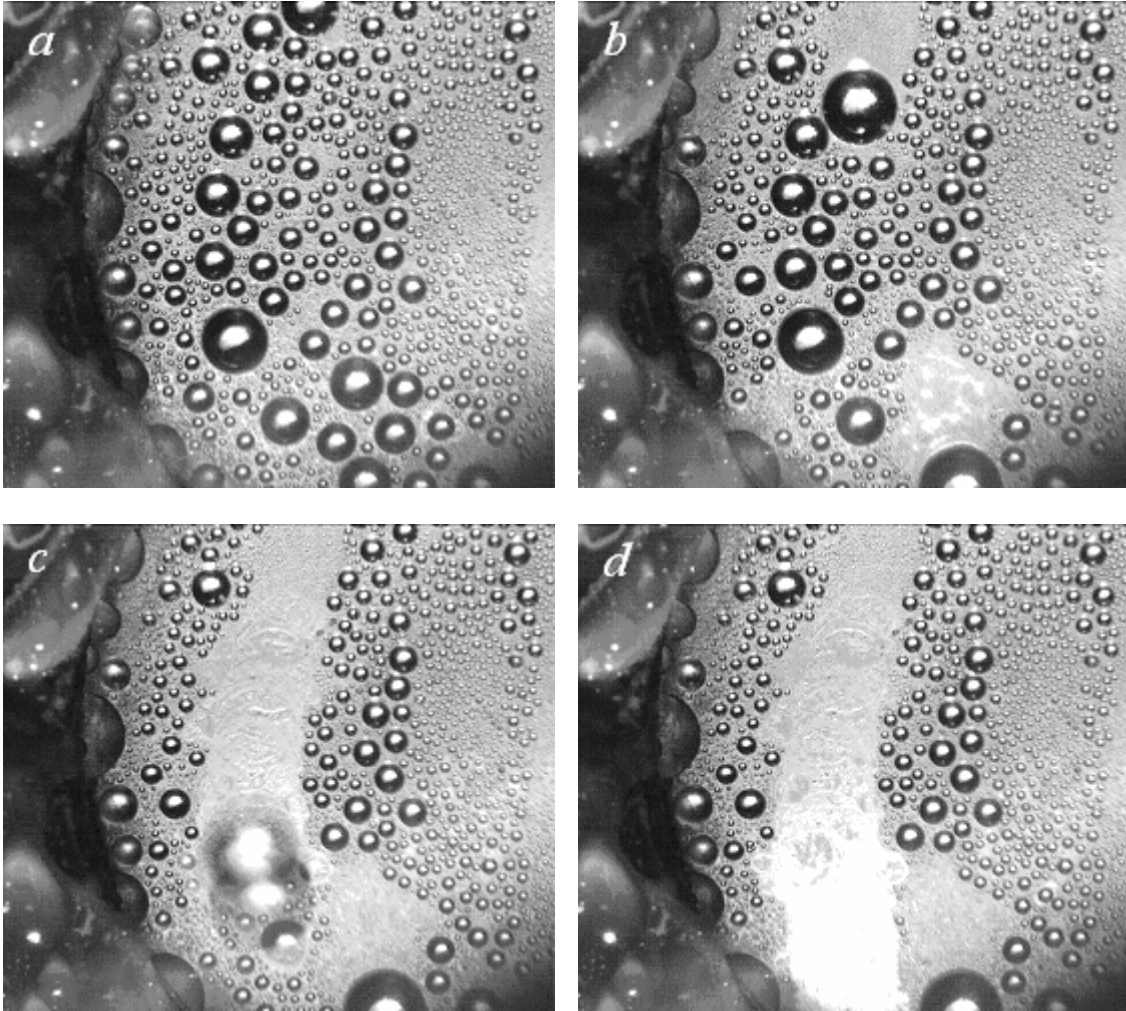


Figure 6-19. Droplet departure and regeneration in DWC without VIDA, 3/15-16. Conditions were THR of 27 W, T_{atm} of 35°C and T_o of 16°C. a) Initial state. b) A large drop began to depart. c) Departed drop quickly swept across condenser surface. d) Swept path left behind departing drop. e) Nucleating drops appear in the swept path of the departing drop. f) New drops continued to grow. g) Swept path began to disappear amid new drop growth.

A clear trend in developing droplet diameter was noticeable. Growing droplet diameter increased with radial position away from the origin and up the swept path. These coupled trends resulted from lower surface temperature and greater age, respectively. This sweeping function would seem essential to the phenomenon of DWC, and indeed it has been called such in the literature. Rose justified the omission of this

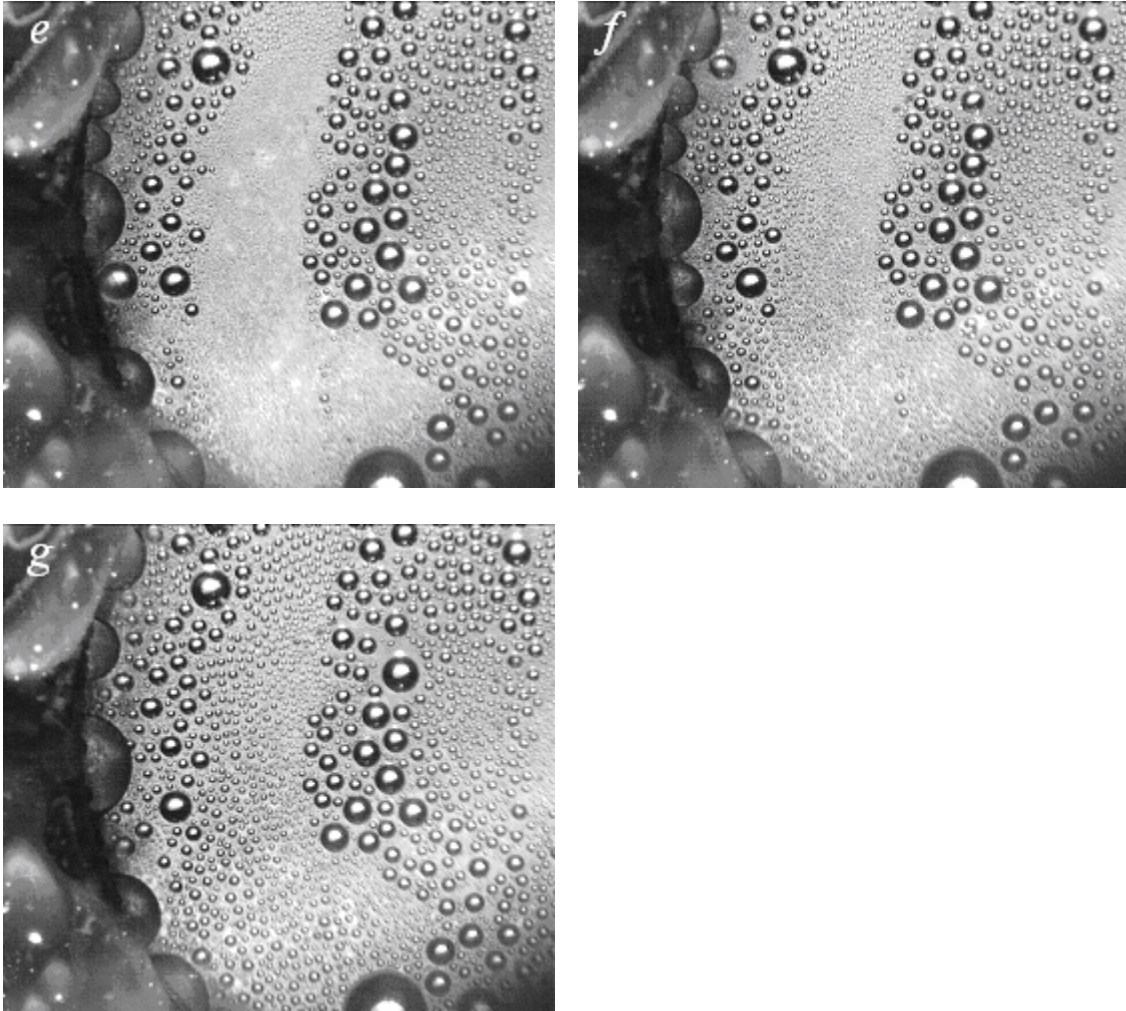


Figure 6-19. Continued.

phenomenon from his theory by saying that the net effect of increased condensate volume for a given time on the lower surface, which would serve to insulate, was effectively offset by the increased sweeping frequencies effect of lowering the maximum droplet size, which would serve to increase HF for a given set of conditions, as shown in the functional behavior analysis section. He also claimed that this net cancellation justified the lack of surface height dependence of his theory [18,24,45]. Indeed, Yamali and Merte, in their 2002 presentation of a theory to go with their experimental results of 1999 [15,16] concluded only slight surface height dependence of DWC HTC from their

theoretical analysis and numerical simulation. The parameters of that study ranged from typical to extreme values of subcooling and body force (a control on maximum droplet size and therefore sweeping frequency). At any rate, the large radial temperature gradient on the diaphragm surface prevented any speculation on spatial effects in this study.

Video frames taken with a high-speed camera offer a detailed look at the onset of VIDA for a condenser surface undergoing DWC (Figure 6-20). Before the driver was switched on, the droplet size and spatial distribution was typical for quiescent DWC. Unfortunately, condensation on the viewing window somewhat often partially obscured the camera view of the condenser surface. Attempts were made at heating the window to prevent this, but found only moderate success. With VIDA applied, ejected droplets also contributed to obscuring the camera view.

Just after the application of vibration to the diaphragm, the outlines of the individual droplets became less distinct, due to their induced oscillations. Next the oscillating droplets merged and began to move toward the center of the diaphragm. Centripetal acceleration from the diaphragm cause droplets above a certain size to be propelled toward the center of motion. This acceleration was more intense closer to the center of motion, therefore the stable drop sizes grew smaller toward the center. This aided the effectiveness of VIDA of clearing the condensate from the diaphragm surface.

As the merged droplets moved toward the center position of the resonating diaphragm, their surface was constantly oscillating and ejecting droplets. At the center, this ejection was most intense. The bulk of fluid was quickly dissipated in this manner, leaving a surface with significantly less condensate on it. The final frame qualitatively represents

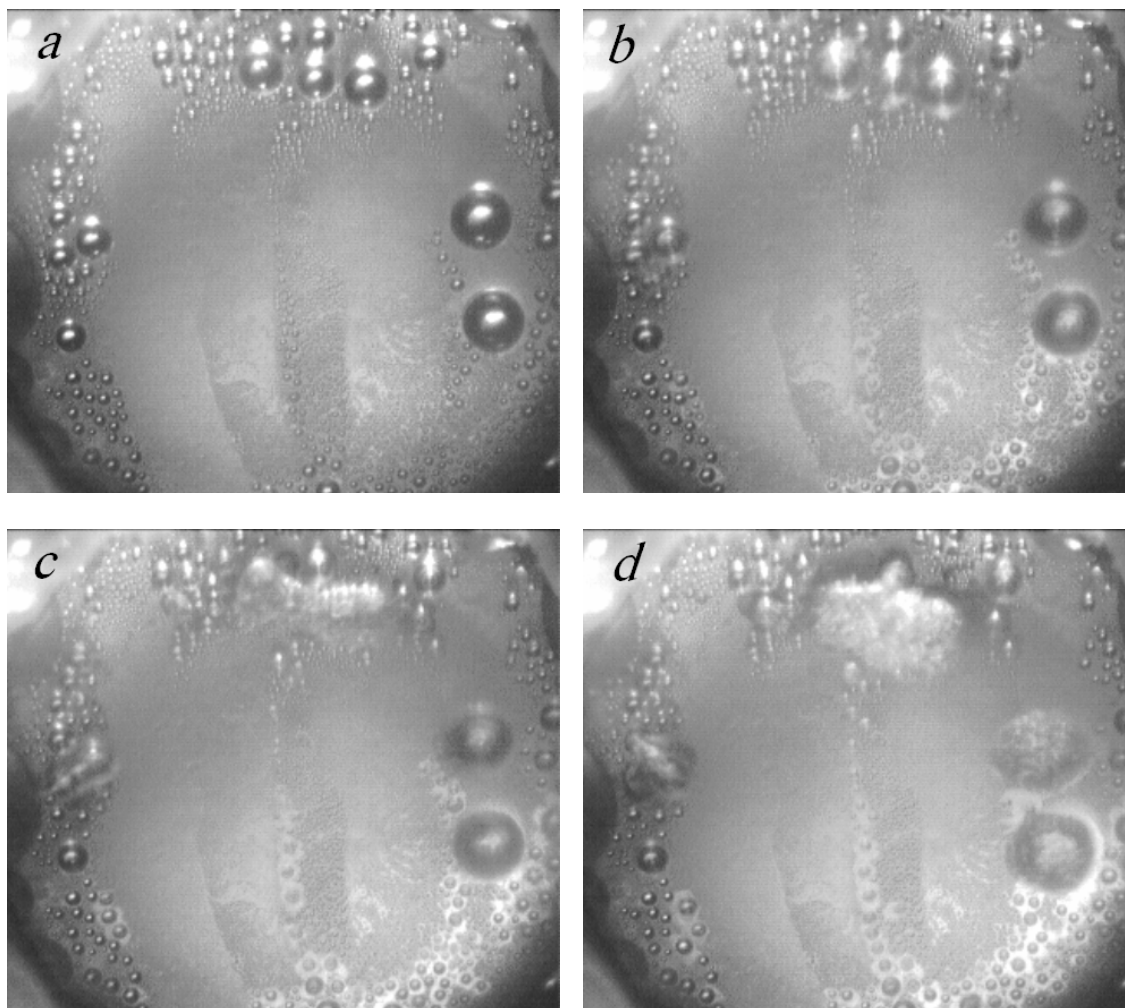


Figure 6-20. Video frames of VIDA onset, front view. Conditions were THR of 27 W, T_{atm} of 35°C, and T_o of 16°C. Video taken at 500 fps. a) Droplet distribution prior to the application of vibration to the diaphragm. b) Just as vibration was applied, the outlines of the drops become less distinct due to surface oscillations, frame 2 (4 ms). c) The three drops begin to merge, frame 3 (6 ms). d) The three drops continues to merge. The two large drops at right begin to merge, frame 4 (8 ms). e) All large water groupings begin to move toward the center of vibration, while undergoing intense surface oscillations, frame 5 (10 ms). f) Migration to center of motion continues as oscillation intensity increases, frame 8 (16 ms). g) All large water drops merged at center, frame 12 (24 ms). h) Virtually nothing left of the primary drops by frame 60 (120 ms).

a steady state droplet distribution under VIDA conditions. The process of condensate removal by VIDA was quite fast. The frame rate for this video capture was 500 fps.

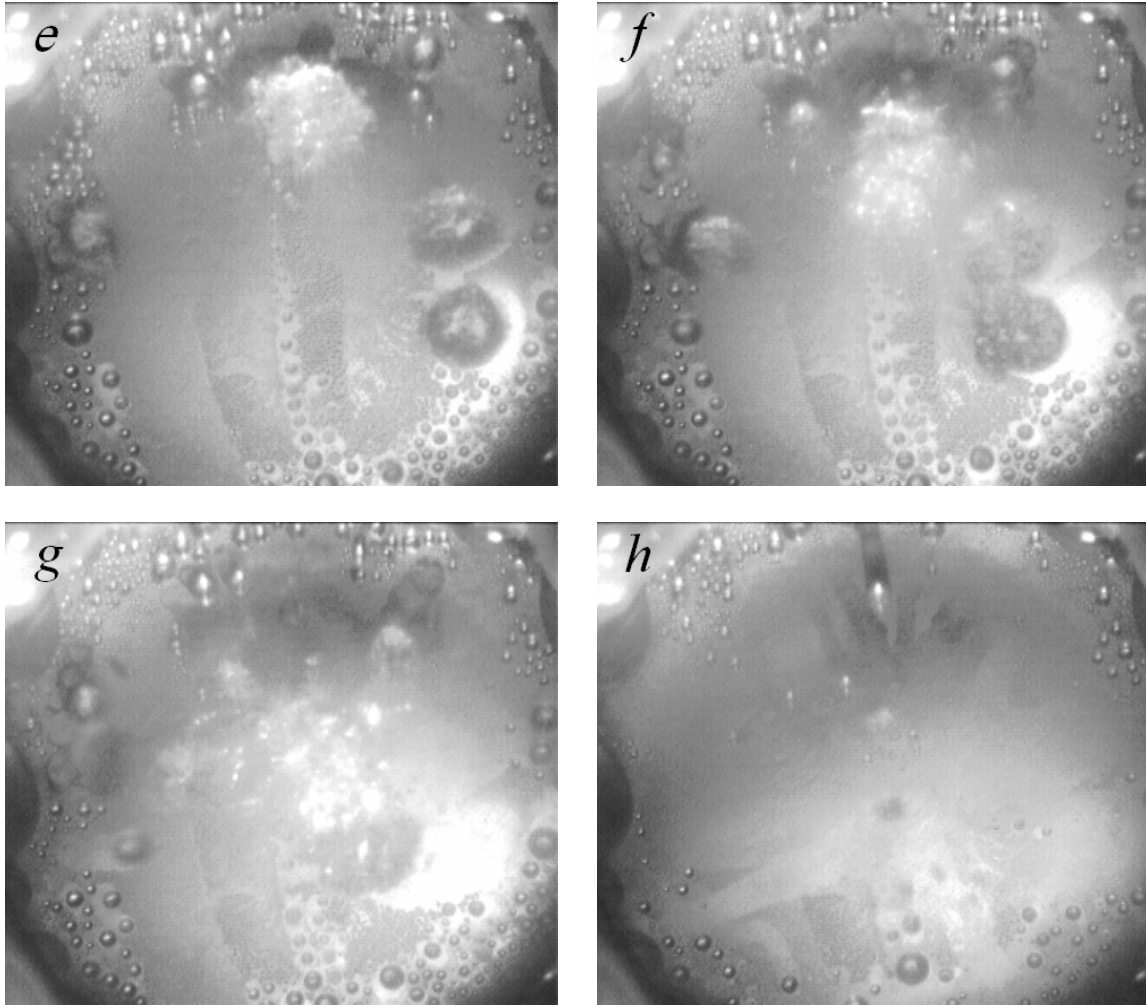


Figure 6-20. Continued.

Frames a through f covered only 12 image captures (24 ms). The entire sequence presented occurred over only 60 frames, or (120 ms).

A calibration curve was constructed for a new driver during the initial testing phase (Figure 6-21). This curve showed a peak-to-peak displacement of about $37\ \mu\text{m}$ at resonance. By this point in the testing, the driver was quite old. It had been employed for almost half of the testing. A frequency response test (Figure 6-22) conducted after conclusion of experiments indicated a peak-to-peak vibration amplitude at resonance of about $13\ \mu\text{m}$. This was only about $1/3$ that of the new driver. Input voltage was held

relatively constant at about 35 Vp-p for this test, with up to 4 Vp-p variance at the peak frequency.

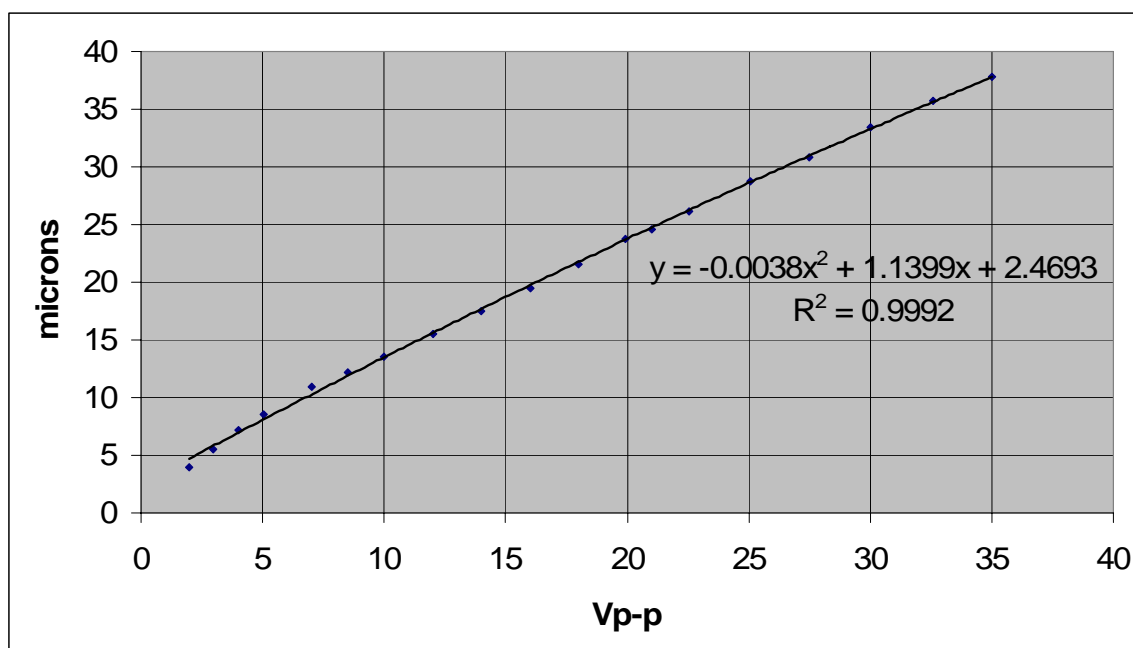


Figure 6-21. Calibration curve for peak-to-peak displacement vs. input voltage. The relation was essentially linear. Peak displacement for this new driver was almost 4 times that of a used driver, tested after running several weeks of experiments. The displacement discussed is that at the center of the diaphragm, which would constitute the maximum.

Generally, frequency tuning to find the appropriate resonance frequency was done by ear. This was easily done, since the sound at resonance was piercing and differences in intensity quite noticeable. When the resonating driver was enclosed in the vessel, the intensity of sound was greatly reduced, however ear plugs were still required for long exposure.

The peak to peak voltage used in this investigation was 35 to 36 Vp-p, with the exception of one day, when testing was done at 42 Vp-p, with no resulting difference in the data. The general uncertainty in this value was ± 0.2 V. Because of all the variability in the driver characteristics, temperature dependence of resonant frequency, and varying

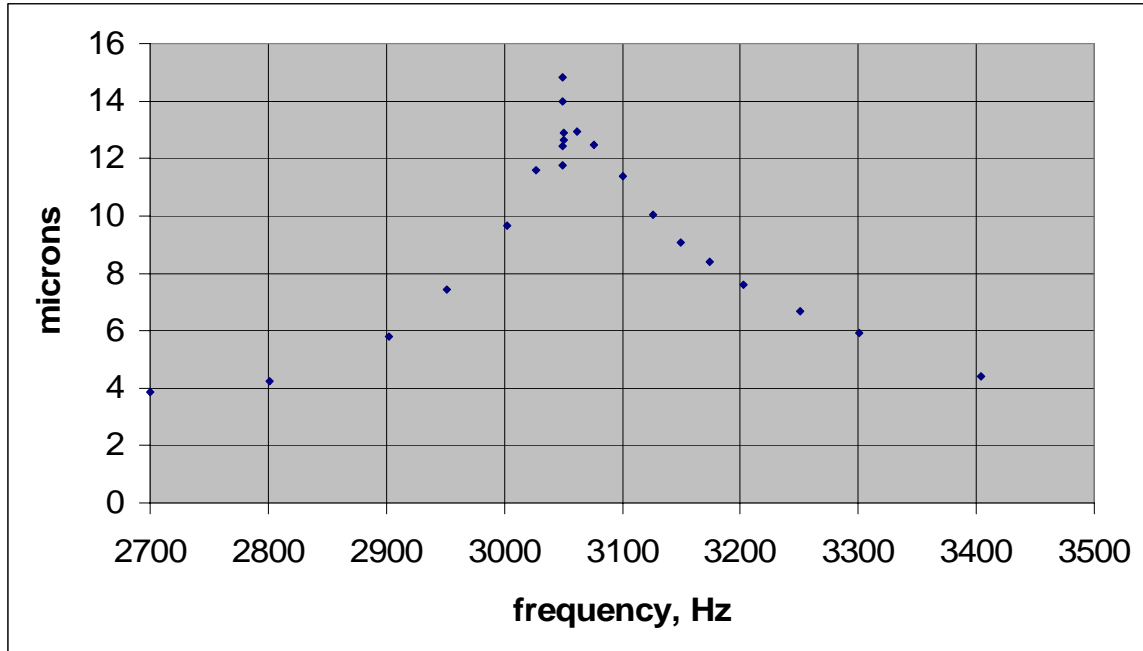


Figure 6-22. Peak-to-peak displacement vs. frequency for used driver, constructed after the conclusion of testing. Note that the resonant frequency of about 3050 Hz (manufacturer reported was 3.6 kHz) was only applicable to room temperature at the time, as this quantity for piezoelectric elements was temperature dependent. The vertical dispersion at resonance represents amplitude variation of the input signal of ± 2 and 4 Vp-p. The displacement discussed is at the center of the diaphragm, the maximum.

intensity of peak response, the focus was kept on the presence or absence of vibration and therefore VIDA. In any case, the maximum droplet size was significantly reduced for the presence of VIDA, even for the older driver.

Vukasinovic [10] offered an excellent correlation for non-dimensional droplet diameter and critical acceleration, shown in Figure 1, but this correlation was not applied to this investigation due to time constraints. Also, a method for application was not immediately clear. The fact that the correlation referred only to maximum acceleration at the center of the diaphragm was a complicating factor. Could this acceleration be projected to the edged of the diaphragm and its correspondingly lower accelerations through a deflection model? This was not addressed in the VIDA study. Also, the main

mechanism that would appear to govern a model as such would depend most on the centripetal acceleration experienced by the drops at the outer radii and at what point this would overcome the surface tension holding them in place. The limit on the drop size at the outer radii would be the critical concern since that was the active area of HT (Figure 3-2). Due to these complications, an attempt to predict the limitation on droplet size was not made, and the VIDA was addressed only qualitatively.

A more detailed, oblique view of the VIDA process offered a better visual description of how this phenomenon progressed (Figure 6-23). This series was taken during steady state conditions and at a higher frame rate (1000 fps). This video was not from the onset of vibration, but taken during quasi-steady state conditions more representative of test conditions. The image focus was again a problem due to condensation on the viewing window and insufficient lighting. Attempts were made in all the video attempts to heat the window to reduce condensation. However these efforts were not always effective.

The series showed a single, large drop at the edge of the diaphragm. This drop was propelled toward the center of motion by the centrifugal acceleration of the resonating diaphragm. The drop surface was constantly oscillating and ejecting droplets. At the center of motion, it merged with a smaller droplet. After only a few frames, the volume of the merged drop was notably reduced by the continuous droplet ejections. These ejected droplets showed up as streaks on the frames. Unfortunately, the frame rate was not fast enough to capture the moving, ejected droplets. There was not enough available light to effectively capture images at a higher frame rate. A given increase in frame rate implies a decrease in exposure time for the CCD, and therefore a lower quality image.

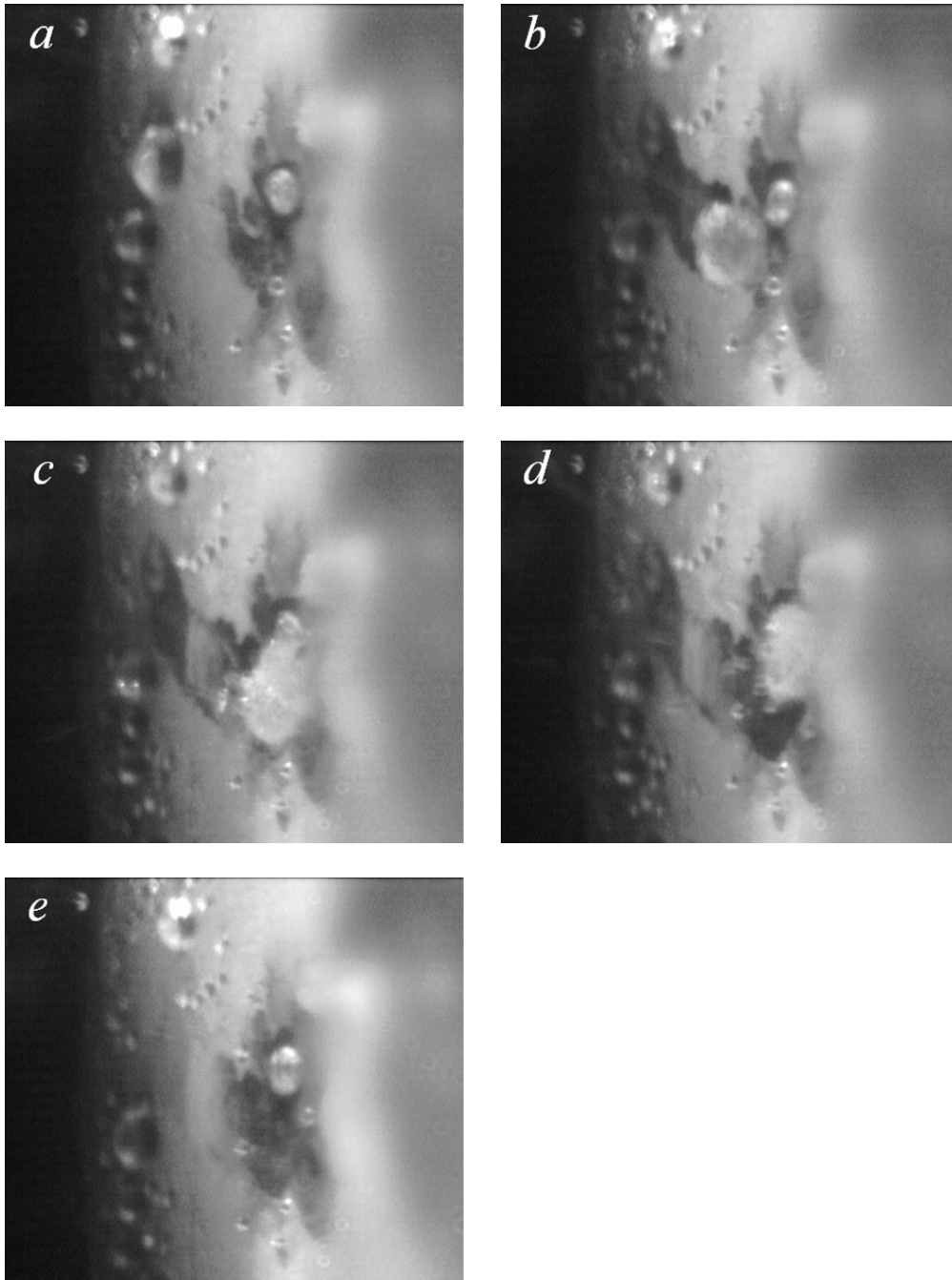


Figure 6-23. Video frames of VIDA process, corner view. Conditions were THR of 27 W, T_{atm} of 35°C, and T_o of 16°C. Video taken at 1000 fps. a) Note large drop in the background, frame 1 (at the edge of the resonating diaphragm). b) Large drop was propelled toward the center of motion, frame 4 (4 ms). Oscillations of drop surface were ejecting secondary droplets. c) Large drop merged with smaller drop at center of motion, frame 7 (7 ms). d) Volume of merged drop was significantly reduced, frame 10 (10 ms). e) Volume of large drop completely dissipated, frame 27 (27 ms).

The center droplet in the final frame was actually quite large. It was normal for there to be a few stationary drops near the center of motion of the resonating diaphragm, however they were usually quite small. For a new driver, these stationary drops were barely visible. The driver employed for these videos was the old driver discussed above, that had only 1/3 of the original peak-to-peak displacement of a new driver, for the given application of 35 Vp-p. Larger amplitude oscillations corresponded to more intense sound and smaller droplet sizes at the center. No size estimate is available for this center drop, but it was noted when the video was taken to be somewhat larger than usual.

Data Summary and Comparison with Theory

This section compares the theoretical THR, computed for the given experimental conditions, with the measured experimental value. The theoretical value for THR relation to maximum departing droplet radius was also used to estimate an effective maximum droplet radius for each set of experimental conditions. See Chapter 3 for further explanation of the calculation methods.

Effective maximum droplet radius values were calculated for those experimental runs considered to most likely be free from the effects of NCG. This determination of acceptability of the results for a given experimental data set was based on the effective maximum droplet radius being less than 2 mm. This upper bound of acceptable r_{eff} was chosen as larger than the greatest theoretical maximum droplet radius considered in this study, 1.1 mm at a T_{sat} of 280K, by a reasonable uncertainty and also by existing grouping of the data. In fact, only 18 of the 104 data points used from the third phase of testing returned reasonable values for r_{eff} , as judged by the aforementioned criteria. The remainder of those 104 data points returned r_{eff} values so large as to not merit consideration. The implication of this fact was that the measured THR was much lower

than that predicted by the Rose theory. Assuming the theory to be accurate for the conditions used and also assuming “good” DWC, a qualitative check of DWC appearance commonly used in the literature [27,31,54,55], the most likely source of this deficiency was a significant presence of NCG.

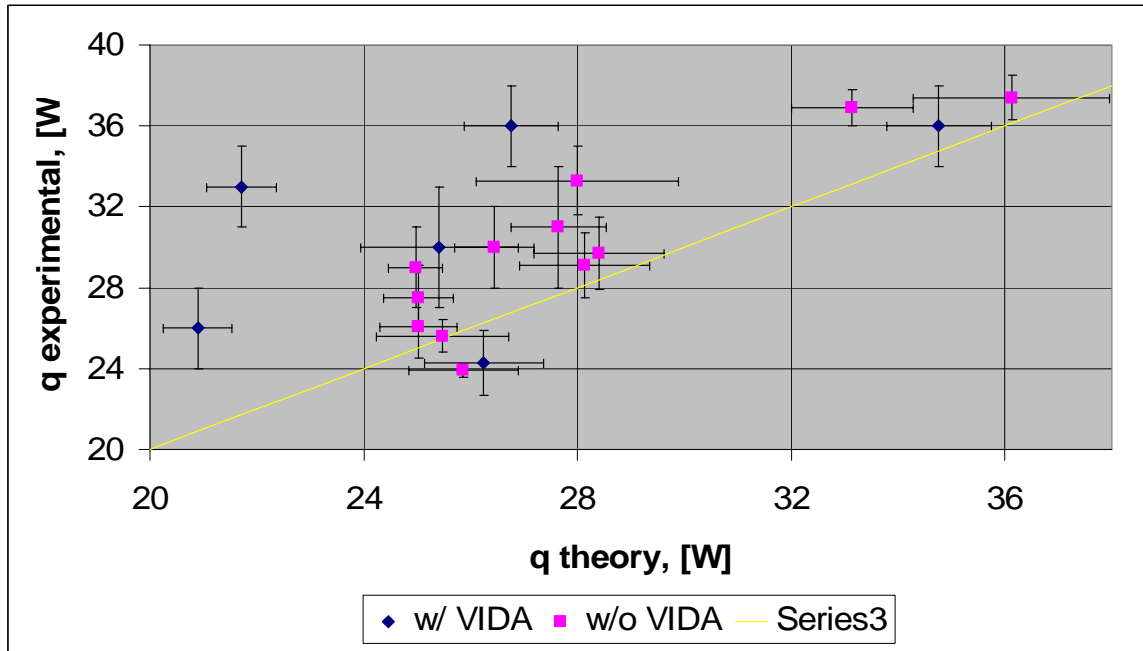


Figure 6-24. Experimental THR vs. theoretical THR. Both axes in W. Diagonal line represented the point where the theoretical value would coincide with the measured value.

Those measured THR values which were determined to be satisfactorily free of NCG were all higher than the theory predicted (Figure 6-24). Ideally, the non-VIDA case would lie directly on the yellow line, which has a 1:1 slope. Aside from one outlier in each data series, all points were above the dividing line. This implied that the actual maximum drop size in this experiment was smaller than the theoretical one, proposed by Rose (Eq. 2-11). This scenario was entirely plausible, due to the inclusion of the empirical parameter K_3 in that equation. This parameter was merely chosen by Rose to provide a good fit to experimental data over the full range of saturation temperature and subcooling data available. Also, the estimated error of the Rose theory from the large

comparison of data in Figure 3 from Rose, 1988 [12], was about 15%. This error estimation easily accounted for the variation. The error was estimated from the given figure because an explicit statement of error for the Rose theory was absent from any publication. The error bars in the figure actually represent the standard deviation in the measured value on the independent axis and the effective variation of the theoretical value from that of the principle inputs on the dependent axis.

Unfortunately, the sample size in comparing those data points free of significant NCG influence was small. Therefore significant conclusions from the data distribution were not warranted. Examining the measured THR with respect to the maximum subcooling (difference between the vapor temperature and the edge temperature of the diaphragm) did not shed any new light on the presence or absence on a VIDA effect on DWC (Figure 6-25). What was of note, however, was that 3 of the 6 data points for cases with the presence of VIDA showed more than a 24% increase over the theoretical prediction. The other three values were well within uncertainty of the predicted values, though whether this lower performance was due to the VIDA not performing its assumed function of limiting the maximum droplet size or whether it was due to a small presence of NCG was ambiguous. The non-VIDA experimental THR values were all within appropriate uncertainty of the theoretical values, though slightly higher, again indicating the possibility of a smaller value for maximum droplet size than that predicted by the theory.

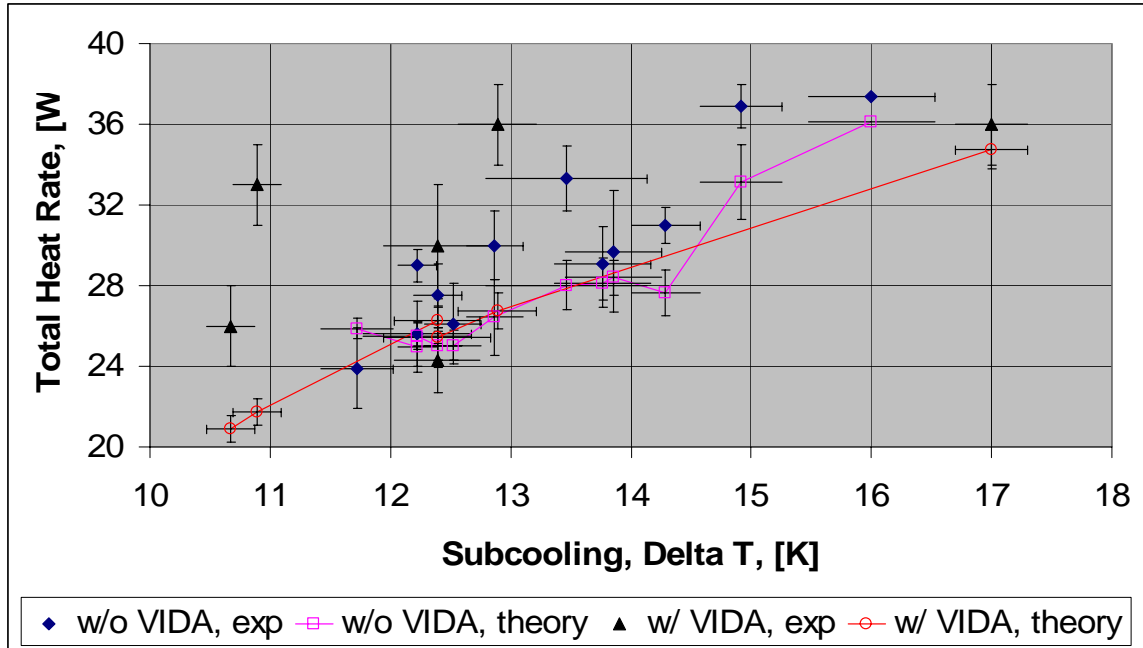


Figure 6-25. Total heat rate vs. maximum subcooling, $\Delta T_{\max} = T_{\text{sat}} - T_o$, in W and K. Experimental values are single points, theoretical values are connected by lines. Cases of both the presence and absence of VIDA shown.

Effective maximum droplet radii were calculated for given experimental conditions using the program `Get_Theoretical_THR_and_r_eff.m` (Appendix A), as discussed in Chapter 3 (Table 6-1). The average r_{eff} determined from these calculations was 24% less for the VIDA cases than for without. If the one high-end outlier was removed from each data set, then the average r_{eff} for the VIDA cases became 46% less than the non-VIDA cases. Such a removal was justified by the fact that the r_{eff} for each was almost 70% larger than theoretical r_{max} . A maximum departing drop size of this magnitude could not be supported by experimental observations.

The results seemed compelling only outside the consideration of the very small sample size involved in the calculations. Indeed, almost 84% of the experimental results (those not presented here) appear to have been tainted by the effects of NCG. The main reason for this situation was poor pressure vessel design.

Table 6-1. Experimental and theoretical data for THR, effective maximum droplet radius, relevant temperature data.

VIDA	THR, exp.	Std. Dev.	THR, theory	Std. Dev.	Effective Max. Droplet Radius	Std. Dev.	Max. Subcooling, $T_{atm}-T_o$	Std. Dev.	T_{atm}	Std. Dev.
Y/N	W	W	W	W	mm	mm	°C	°C	°C	°C
N	23.9	03	25.9	1.0	1.72	0.13	11.7	0.3	30.7	0.3
N	29	2	25.0	0.5	0.45	0.24	12.2	0.2	25.6	0.11
N	25.6	08	25.5	1.2	1.07	0.22	12.2	0.4	27.4	0.4
N	27.5	1.6	25.0	0.7	0.63	0.27	12.4	0.2	25.2	0.17
N	26.1	1.6	25.0	0.7	0.86	0.39	12.5	0.2	24.7	0.2
N	30	2	26.4	0.7	0.52	0.27	12.9	0.2	26.1	0.2
N	33.3	1.7	28.0	1.9	0.39	0.15	13.5	0.7	27.2	0.7
N	29.1	1.6	28.1	1.2	0.91	0.35	13.8	0.4	26.1	0.4
N	29.7	1.8	28.4	1.2	0.85	0.37	13.9	0.4	26.2	0.4
N	31	3	27.6	0.9	0.56	0.46	14.3	0.3	27.3	0.3
N	36.9	0.9	33.1	1.1	0.58	0.09	14.9	0.3	30.6	0.3
N	37.4	1.1	36.1	1.8	0.89	0.17	16.0	0.5	31.8	0.5
				Avg.	0.79	0.26				
Y	26	2	20.9	0.6	0.30	0.19	10.7	0.2	24.2	0.2
Y	33	2	21.7	0.6	0.08	0.04	10.9	0.2	24.7	0.2
Y	24.3	1.6	26.2	1.1	1.70	0.78	12.4	0.4	28.3	0.3
Y	30	3	25.4	1.5	0.42	0.36	12.4	0.4	26.2	0.4
Y	36	2	26.8	0.9	0.18	0.08	12.9	0.3	26.8	0.3
Y	36	2	34.8	1.0	0.90	0.36	17.0	0.3	25.3	0.3
				Avg.	0.60	0.30				

Additional Testing

Further testing was undertaken to clarify any effect that VIDA might have on DWC HT. There were three main aims of this new round of testing. The first aim was to better control NCG in the test apparatus by special attention to seals and valve arrangements. The second aim was to place thermocouples on the diaphragm surface, in order to confirm the assumed radial temperature profile. The third aim was to better achieve a saturated atmospheric condition in the test vessel by making the water reservoir physically separate from the pressure vessel. A halogen lamp was still used for heat input, but a separate vessel was constructed to hold the excess water and connected to the main vessel by vacuum tubing and valves.

Three days of testing were conducted in this new phase of testing. The results from the first day of testing had low overall THR values, which was a symptom of bad seals allowing continual leakage of NCG into the pressure vessel. The potential leak points were then sealed to the extent possible with the current design. The second day of testing, 5/21, showed overall THR values much more inline with the theoretical predictions. Though the temperature data showed slight increasing trends with time, this increase was caused by drift in the coolant inlet temperature, which was the base point for these values (Figure 6-26).

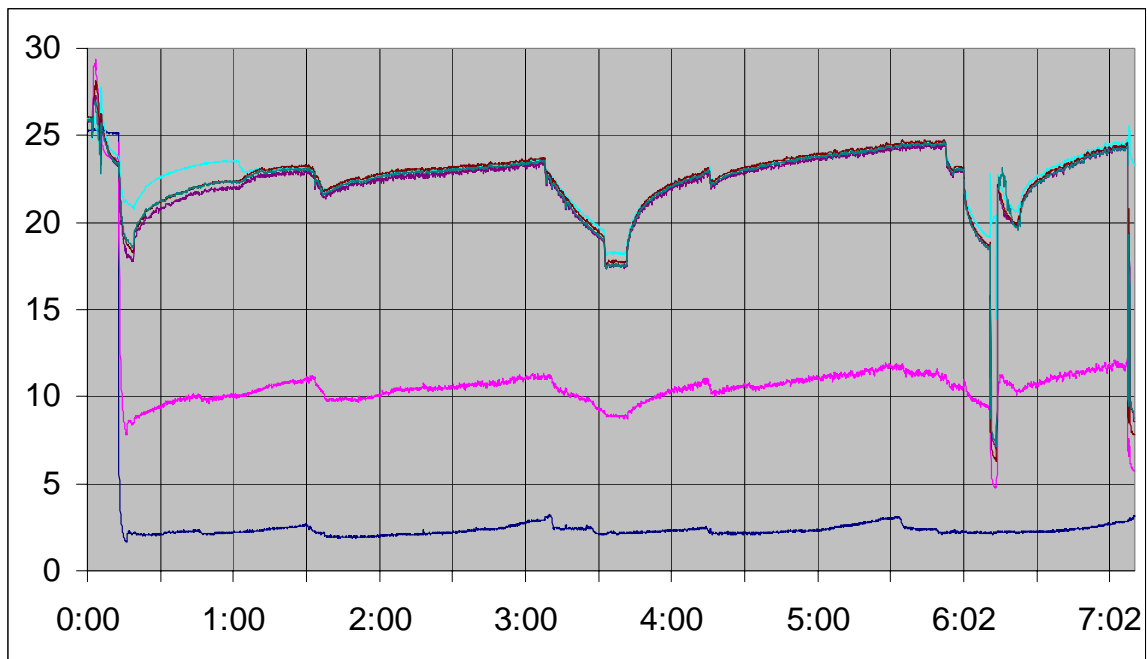


Figure 6-26. Temperature data from 5/21, the second day of additional testing. Readings were in °C. Time axis in hours:min. The top four temperature traces show the atmospheric temperature estimate with three thermocouple readings placed on the condenser (diaphragm) surface. The three thermocouples were placed so as to divide the radius of the shim into equal parts along the same line, in order to confirm the assumed temperature profile. The middle temperature value was the average edge temperature. The lowest temperature was that of the coolant inlet. Each major dip in temperature coincides with an evacuation operation on the vessel. No VIDA was induced in this test.

The four highest temperature traces from that data represented the atmospheric temperature estimate, a single thermocouple located about $\frac{1}{2}$ inch above the test surface, and three thermocouples attached to the surface of the brass shim. The adhesive used was the same insulating RTV silicone employed elsewhere in the apparatus. Adhesive was applied and allowed to cure with the thermocouple bead pressed against the brass surface.

After allowing 18 to 24 hours for the silicone to cure, digital pictures of the thermocouple arrangement were taken from directly overhead. Geometric markers were then added to the pictures and bead center positions and uncertainties then estimated by pixel counting. The center thermocouple covered the center point of the diaphragm and so its reading was assumed to represent the average temperature of the center 10% of the radius. The centers of the other two thermocouples were located at $33 \pm 13\%$ and $66 \pm 9\%$ of the radius from the center, respectively. Visual appearance of condensate distribution on the condenser surface was essentially the same as without the attached thermocouples.

It was attempted to make the thermocouple bead placement collinear. The placement of this line was roughly horizontal during testing, though deliberate variation of this quality showed no effect in the data. The test surface was vertical and all other thermocouples placed in the same arrangement as in the previous tests. See the Additional Testing section of Chapter 7 for a discussion of calibration and uncertainty for this round of testing.

In the first hour of testing, superheating was noted in the vapor. This was corrected by rotating the vessel a few degrees to allow for unimpeded entrance of the vapor to the test vessel atmosphere. This step was necessary because the volume of collected

condensate would sometimes be substantial enough to clog the inlet tube from the vapor supply, located at the center of the lower window hole.

The clogging (or reflux prevention) phenomenon necessitated periodic efforts to drain the condensate, since the vapor velocity issuing from the $\frac{1}{4}$ inch ID vacuum tube coming from the Bulk Fluid Reservoir was sufficient to prevent any backflow of condensate. Drainage was accomplished by simply turning off the halogen lamp used for a heater for a few minutes and elevating the vessel slightly to facilitate condensate removal. This process was only necessary once every few hours of testing and only lasted about 5 minutes. Thus it was a notable event in the temperature record, but had few larger effects. However, the initial clearing of condensate did have the effect here of eliminating the superheat of the vapor for the remainder of the test, during which the maximum variation between any of the surface thermocouples and the atmospheric reading was less than about 0.5°C .

Each major collective drop in the temperature readings corresponded to an evacuation operation, similar to earlier tests. More shallow and short temperature drops were due to condensate draining operations. The significance of the 5/21 test data was that it confirmed that the center $\frac{2}{3}$ of the radius of the diaphragm was very near the vapor temperature and was thus relatively inactive in HT transfer compared to areas closer to the edge, as the assumed temperature profile had predicted. Though there was a distinct decrease in each successive temperature reading from atmospheric to center to $\frac{1}{3}$ to $\frac{2}{3}$ thermocouples, the magnitude of the decreases was less than 1°C .

A comparison was made of the measured surface temperature data and the assumed temperature profile for the non VIDA case of 5/21 (Figure 6-27). A distinct decrease was

noted in the temperature values, 23.35°C at the center, 23.19°C at the 1/3 position, and 23.06°C at the 2/3 position. However, the uncertainty in the measured temperature was 1.0°C, so these values were essentially equivalent and the model was accurate to within experimental uncertainty. Thus with the major assumption of the temperature profile prediction had been confirmed at a few points along the radius, for the non-VIDA case only.

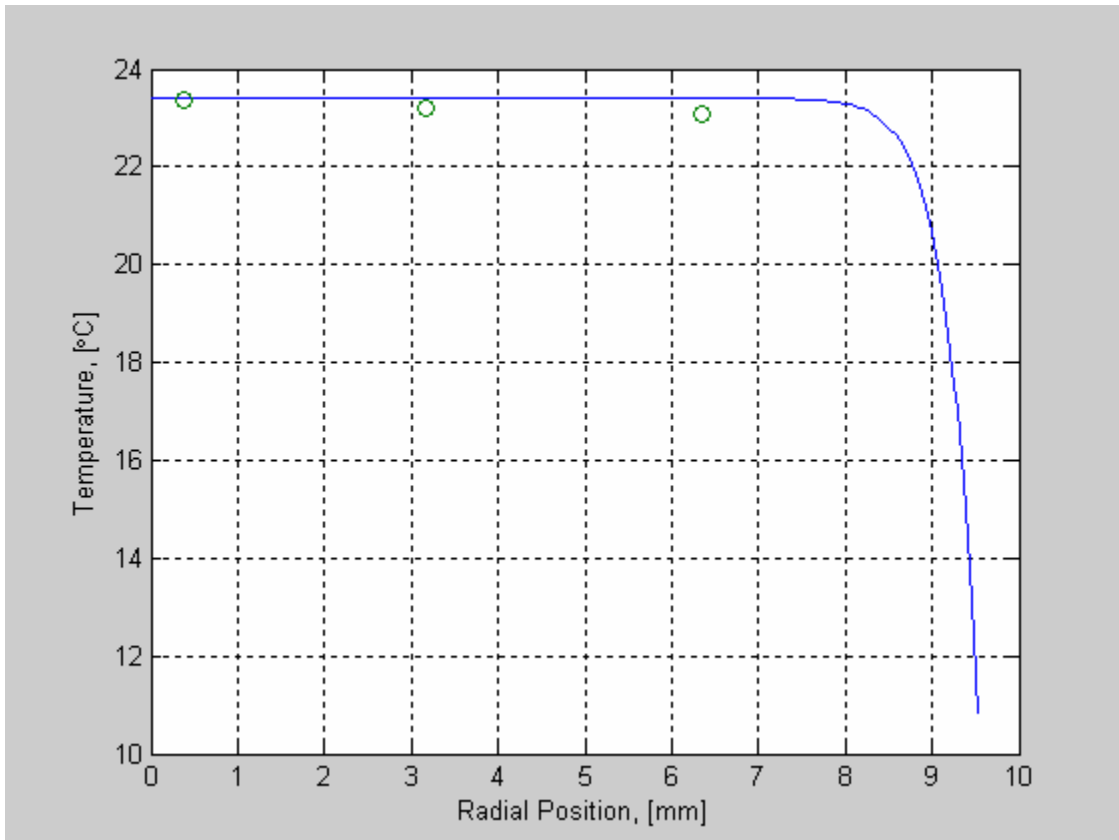


Figure 6-27. Comparison of 5/21 surface temperature data for experimental run C with the assumed temperature profile. The solid line represents the assumed profile and the circles the three surface temperature measurements, averaged over the given time period. The uncertainty in the measurements was 1.0°C, so the agreement was good within experimental uncertainty.

The next day of testing (5/24) attempted a more direct comparison of DWC with and without vibration. The non-vibrational data from this day looked essentially identical to the 5/21 results. This fact along with the large number of reasonable r_{\max} values

attained with this day of testing indicated much better control of NCG as compared to previous testing. A very important event was noted in the surface temperature readings after the application of VIDA. The two center temperature readings increased suddenly from their otherwise nominal grouping with the atmospheric reading (Figure 6-28). This jump indicated that the center and the 1/3 position temperatures read higher than the vapor temperature. This meant that no condensation at all was taking place on this portion of the diaphragm surface.

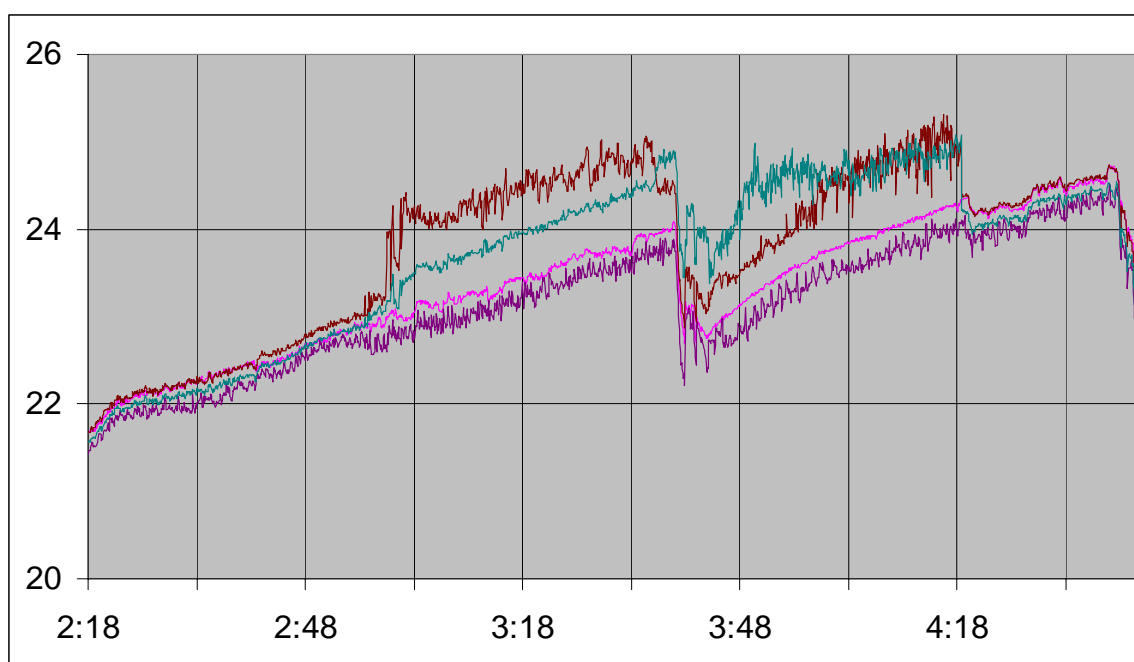


Figure 6-28. Comparison of 5/21 VIDA and non-VIDA temperature data for shim surface and atmospheric. Data is in °C. Data shows difference in vibration and non-vibration cases. The two higher values were the shim surface temperature at the center and at 1/3rd of the radius away from the center. The next highest value was the atmospheric temperature estimate and the lowest temperature was the shim surface temperature taken closest to the edge. Note that the center of the diaphragm was at a higher temperature than the vapor under application of vibration to the shim, indicating that condensation was not taking place over this center area at all, thus invalidating the surface temperature profile assumed in the theoretical model for the vibrational case. The drop in values at 3:40 corresponded to draining of the condensate from the pressure vessel.

This elevated center temperature explained the observation that a large dry patch appeared in the center portion of the diaphragm upon application of vibration. This phenomenon had been noted before, but it had been assumed that this region simply had a maximum droplet size that was too small to be visible to the naked eye. The most important implication of this finding was that the assumed temperature profile did not apply for the cases with vibration. This finding thereby invalidated the theoretical model used in the previous analysis for comparison of data points. Presumably, the increased surface temperature of the center portion of the diaphragm was due to resistance heating of the piezoelectric patch. A major implication of this discrepancy was that the active surface area of condensation was very different between the two fundamental cases, which made direct comparison somewhat dubious.

Table 6-2. Data summary from additional testing.

VIDA	THR, exp.	Std. Dev.	THR, theory	Std. Dev.	Effective Max Droplet Radius	Std. Dev.	Max Subcooling T _{atm} -T _o	Std. Dev.	T _{atm}	Std. Dev.
	W	W	W	W	mm	mm	°C	°C	°C	°C
N	32	2	24.1	0.9	0.21	0.10	12.4	0.3	23.06	0.13
N	31.0	1.0	24.5	0.5	0.27	0.06	12.5	0.2	22.96	0.10
N	30.3	1.0	24.5	0.6	0.32	0.07	12.5	0.2	23.29	0.11
N	29.7	0.7	25.0	0.9	0.40	0.06	12.7	0.3	23.5	0.2
N	28.8	0.8	25.4	0.8	0.53	0.10	12.8	0.3	24.11	0.17
N	33	2	24.9	0.6	0.20	0.10	12.6	0.2	23.90	0.09
N	28	3	25.2	0.4	0.6	0.6	12.7	0.10	23.70	0.05
N	25.7	1.2	26.8	0.8	1.4	0.4	13.4	0.2	24.40	0.15
				Avg.	0.49	0.19				
Y	28.7	1.4	25.6	0.8	0.6	0.2	13.1	0.2	23.6	0.2
Y	26.9	1.7	25.6	1.3	0.8	0.4	13.0	0.4	23.7	0.4
Y	38	3	26.3	0.7	0.12	0.08	13.1	0.2	24.7	0.12
Y	28.6	0.8	24.6	1.8	0.46	0.09	12.5	0.6	23.8	0.4
				Avg.	0.50	0.19				

The theoretical predictions of THR for the VIDA cases were included with the data summary for the Additional Testing (Table 6-2). This inclusion was made even though a base assumption of the model has been proven incorrect for the VIDA cases, simply as a

means for comparison with earlier data. All data points taken from 5/21 and 5/24 appeared to be effectively free of significant influence of NCG in the test vapor. This conclusion was based on the proximity of the non-vibration THR values to the theoretical prediction of THR.

Since the theoretical model for comparing the vibrational and non-vibrational cases had to be set aside, raw comparison of the THR values for similar cases of each had to be examined. No systematic advantage in HT was noted from the presence or absence of VIDA in DWC on a piezoelectric diaphragm from this comparison.

CHAPTER 7 UNCERTAINTY

Main Study

Uncertainty is always an important factor in experimental studies. The pressure readings of the vacuum gauge, in this study for example, were accompanied by such high uncertainty ($\pm 1\%$ of full-scale-vacuum) that they were of little use at the low vapor pressures of water used. Indeed, use of these readings to estimate the NCG partial pressure from temperature readings of the atmosphere in the test vessel often resulted in negative values, of course a physical impossibility. Thus values from the pressure readings were not referenced in this paper and were mainly used as an immediate measure of vacuum pump performance.

Thermocouple calibration was also a concern. Erroneously, the batch was not calibrated together prior to experiments, merely used straight out of the box. Also, there were several batches of thermocouples used, of both type J and type K. Whenever applicable, the settings of the DAQ were changed to accommodate the difference in thermocouple type. By the third stage of testing, the importance of these errors was realized and a step implemented to compensate, to the extent possible. After the conclusion of each day's experiments, everything was turned off, but the vessel not vented to atmosphere. The apparatus was then allowed to reach equilibrium over night. Thus, the next day, the temperature distribution in the vessel could be assumed relatively uniform and any systemic differences in the thermocouple readings noted. Typically 100 data capture cycles (5 seconds per cycle) were taken in the checks. Then all the averages

and standard deviations were calculated for the respective groups. For the two thermocouples external to the pressure vessel, the average of their difference was used instead of the average of each individual unit. The maximum standard deviation calculated in this manner over 9 checks was 0.15°F (0.13°C) at an average equilibrium temperature of 79°F (26.11°C). This of course represents only the relative error and not absolute error.

In all but a few cases, for those data with r_{eff} near or below the theoretical value, the variation in physical value was high enough that the experimental uncertainty made only a negligible contribution to the standard deviation of the reading (Table 7-1). In these calculations, it was the standard deviation which was used as uncertainty. The majority of the uncertainty for thermocouples (TC), was constituted by the absolute error reported by the manufacturer for the J and K type thermocouples used, 2.0°C. The relative error of these thermocouples was around 0.15°C. Flow rate was a very important quantity for these calculations, since the measured heat output was directly proportional to it. If a more precise way to measure the volumetric or mass flow rate were available, it would drastically improve the uncertainty in this quantity. The voltage, frequency, and pressure readings, however did not directly factor into any calculations.

Table 7-1. Uncertainty in measured values.

Quantity	Unc.	Units
Thermocouple	2	°F
Flow-rate	0.1	gph
Vp-p	0.3	V
Frequency	10	Hz
Pressure	0.3	in-Hg

Also, due to the steep gradient of the temperature function at the edge of the diaphragm, the numerical integration of the theoretical THR in the iterative process, was

very sensitive to the number of terms that the radial distribution was divided into. The number used in constructing the tables was 2000, chosen based on the highest precision with a reasonable computation time.

Since further increases in the number of terms continued to change the outcome of the calculations, another method had to be applied to estimate the bias error of this method of calculation. A geometric series was examined, based on the number of radial terms used to iterate the theoretical THR and the magnitude of the change in the result, for otherwise constant input. By projecting the change in calculation result to a high number of radial terms, it was determined that the iterations, at 2000 terms, systematically underestimated the actual value from 2.4% for the lowest THR, to 4.7% for the highest. Intuitively, it made sense that the error would be higher at higher THR, since these values would have higher gradients in the temperature function at the edge of the diaphragm and therefore be more sensitive to step size changes. This condition was exacerbated by the very high HTC for the high subcooling at the edge.

Additional Testing

In the new round of testing, all thermocouples used were type T. This change was made because T type was also active in the temperature range in question and the absolute uncertainty in temperature listed by the manufacturer, Omega Engineering, was half that of the type J and type K that were used in previous tests at 1.0°C. Calibration was conducted simultaneously with all thermocouples and two high-precision, ± 0.1 and $\pm 0.05^\circ\text{C}$, mercury thermometers. Data points in the calibration were taken every few degrees from 0 to 50°C. Linear calibration coefficients were then determined for each thermocouple reading. The readings offered by the data acquisition program, issued with the DAQ card, were only available as temperature readings not direct voltages, so this

given value was used as a raw reading for calibration and data collection. After the data was collected, the calibration equations were applied to each thermocouple data stream. The maximum root mean squared of the error for each calibrated thermocouple over the calibration data set was less than 0.2°C relative to the thermometer readings.

The maximum discretization error of the A/D conversion was $\pm 0.02^{\circ}\text{C}$. Therefore, the maximum uncertainty in the measured temperature values reported in the Additional Testing section, as determined by the square-root-of-the-sum-of-the-squares method was 1.0°C . However, steady state differences in the relative surface temperature and vapor temperature readings were noted to be as little as 0.1°C .

Special care was taken to insulate the bare wire lead sections of the surface thermocouples by covering them with the same silicone insulation used for adhesion. Insulating the wire leads was recommended to keep them from acting as fins to cool or heat the thermocouple bead [46]. Using an insulating adhesive for attaching the thermocouple beads to the diaphragm surface was recommended to again insulate the thermocouple bead from all its surroundings except the diaphragm surface [92]. After all, a thermocouple only reads the temperature of the bead, not that of the intended object.

CHAPTER 8 CONCLUSIONS

Main Study

Non-condensable gases were not sufficiently controlled in this test apparatus. This oversight was due to a lack of understanding of their very significant effects on DWC, at even small relative concentration to vapor, through the design, fabrication, early and intermediate experimental phases. Attempts were made in the third and final phase of testing to reduce the NCG presence as much as possible. However, in many cases, the reduction in overall condensation HT due to the added diffusive resistance of NCG to the net mass inflow to the condenser surface was still significant enough to deny comparison of the experimental and theoretical values. The greatest decrease in HT from theoretical to experimental found in the data used was 94%. This figure emphasizes the absolutely critical importance to DWC of minimizing the presence of NCG. Unfortunately, due to the availability of only a low precision pressure instrument, estimations of NCG partial pressure during the testing were impossible. An attempt was made to model the leak rate over several days and then extrapolate to the time of the experiment, but precision of the results was unsatisfactory.

Out of 104 data points considered, only 18 yielded favorable comparisons to theory. Six of these cases were with VIDA present, 12 without. All but one outlier from each category showed better HT than predicted by the Rose theory. Although the experimental non-vibration values were slightly higher than the theoretical prediction, they were still within one experimental uncertainty. Half of the ‘good’ VIDA, or those

runs with vibration present, measurements were an exception to this, showing 24, 34, and 52% more HT than predicted by theory. While these increases show potential, the overall HT rate was relatively small for the total area of the driver (2.9 cm^2), yielding a meager 20.5 W/cm^2 average HF for the absolute highest THR measured. In fact, the average HF for those tests yielding reasonable r_{eff} values was only 10.6 W/cm^2 . For all the measured data, THR ranged from 2.9 to 58.3 W for T_{sat} from 25.3 to 56.5°C and T_o from 24.2 to 46.7°C .

In light of the results, three experimental instances likely indicated a significant increase in HT (of a maximum 50%) due to the application of VIDA. The VIDA served to limit the maximum droplet diameter thereby increasing the HT. However, the majority of the data was rendered useless by the presence of NCG in the test vapor. The effect of NCG in the test vapor was to depress the HT. Because of these problems it was impossible to draw any solid conclusions, except to say that any increase in DWC HT due to the application of VIDA would likely be less than an order of magnitude for the overall THR.

Trend Explanation

The following points offer possible explanations of several trends encountered in the experimental data:

- THR increased significantly with increasing pressure, even despite the presence of NCG in unknown concentration. This follows directly from the prediction of the Rose theory.
- The application of VIDA had the immediate effect of lowering T_{atm} for a given set of conditions. This was most likely due to the spray of ejected droplets evaporating wholly or partially in the air, rather than flowing directly into the liquid reservoir. The ejected droplets may also have impacted the thermocouple beads directly, thereby cooling them.

- Once sufficient effort was focused on minimizing NCG, superheat was noted on the vapor over the liquid reservoir temperature, where most of the heat was coming in. This implied significant heating of the aluminum vessel body. This implication was confirmed by experimental notes that at times the metal vessel was nearly too hot to touch. Possible ramifications of this would be:
 - Inaccurate saturation pressure estimation from T_{atm} . In the cases where superheat was noted of magnitude greater than the uncertainty in T_{atm} , the T_{liq} measurement was substituted for T_{atm} in theoretical calculations. However, this situation affected only one data point used in r_{eff} comparisons.
 - Potential for significant HT to the cool side of the vessel through the Teflon insulation cylinder, though this potential was not quantified.
- A given increase in NCG concentration in the vessel during DWC would cause an increase in the liquid reservoir temperature (T_{liq}), a proportionately smaller decrease in atmospheric temperature (T_{atm}) and edge temperature (T_o), and also a decrease in the measured total heat rate (THR). These trends were totally in line with the literature survey findings under the heading Effect of Non-condensable Gases (NCG).
- Excellent DWC quality (droplet symmetry and size distribution) was noted throughout the testing despite no intentional application of a dropwise promoter, purportedly essential on a clean metal surface. An obvious conclusion was that the diaphragm was not sufficiently cleaned, especially since FWC was never satisfactorily induced on the surface of the diaphragm, except under VIDA conditions. In addition to potential surface contaminants remaining through the driver cleaning process, an oily film was noted on the inside of the vessel and on the top of the liquid after every test run was allowed to sit over night. This film may have been from the significant amount of silicone sealant used. It may have been a remnant from the oil used for machining the largely polymer components of the apparatus. A contribution may have also been made by the Dow Corning High Vacuum Grease used on the seals.

Additional Testing

Further efforts at testing, which eliminated possible parasitic heat transfer from the pressure vessel wall, directly measured surface temperature data for the brass shim, and improved control of NCG in the apparatus showed illuminating results. The surface temperature readings showed that the theoretical model, which assumed a substantial portion of the center of the condenser surface was very close to the vapor temperature,

applied well for the non-vibrational case but poorly for the case with vibration. This finding invalidated a potentially useful tool of comparison for the two cases. Also, the elevated center temperatures, relative to the vapor condition, indicated that the surface area of the diaphragm active in condensation was significantly smaller in the vibrational case than the non-vibrational case, preventing precise comparison even of the measured THR values.

Noting, however, that the active HT area on the diaphragm was smaller with applied VIDA, the fact that those data points judged acceptable showed comparable to slightly better overall THR values with applied VIDA says that applied vibration does serve to increase the effectiveness of DWC HT for a given area. Unfortunately, due to the unknown active HT area change, it was not possible to offer a quantitative estimation of this increase.

Of positive note was that the adjustments to the apparatus when combined with established procedures appeared effective at minimizing NCG in the test atmosphere, thereby increasing confidence in the accuracy of the measured results.

Improvements

The results of this study were so flawed by the presence of NCG, that, if it were to be undertaken again, the apparatus would likely be completely different. Some primary suggestions for improvement of the apparatus are as follows:

Apparatus

- Design seals with large flanges and gaskets specifically designated for steam use, likely Teflon. Minimize potential places for leaks in the design. This study had sought to use a pre-existing pressure vessel, and the outcome ultimately suffered because of this.
- Provide ample windows for both lighting and cameras. Make them electrically heated, to prevent fogging [31]. The windows must also be sufficiently far away

from the driver surface that it does not get sprayed with ejected droplets. Six to eight inches should be sufficient. An alternative would be to angle the window surface down and coat it with a substance such as Rain-X® to encourage the drops to run off, or provide a wiping system on the interior, though the latter option would likely be prohibitively complex when sealing is considered.

- Provide for a heater to be directly immersed in the liquid reservoir, so that all heat entering the system may do so through the liquid, thereby cutting down on superheating of the vapor. External heating may also be used, provided that the reservoir is effectively thermally isolated from the test section.
- Thermally isolate the liquid reservoir and heating apparatus from the test section of the apparatus. This will also significantly cut down on superheating, which when combined with the heater changes above would make saturation temperature measurement more accurate, since the test area atmosphere should be within a very small margin of the liquid reservoir temperature. This method was used in nearly every experimental study cited.
- Make the heater output power constant. Furthermore, design the heater capacity for at least 60% excess vapor, based on the maximum expected HT rate, to be supplied to the condenser surface so that supply would never be the limiting factor.
- Make the vapor system closed loop for sub-atmospheric pressure tests. Accomplish this by using a cold trap on the vapor exit line, often cooled by main water for steam tests at 1 atm, but would need significantly cooler than T_{sat} temperatures to condense as much vapor as possible. Ice or liquid nitrogen would work sufficiently in a 'jacket' around the vapor line. The flow would then enter a phase separator hooked to a vacuum pump, of continuous duty, to remove any NCG. Then condensate would collect in a holding area and be metered to estimate the venting rate, by time average.
- Use a close venting scheme for removing the excess vapor, where the nozzle is located near the condenser surface. An excellent description is provided in Le Fevre and Rose, 1965 [31], and an in-depth analysis of the method provided for a specific geometry in Citakoglu and Rose, 1968 [32].
- Take care from the fabrication and assembly through pre-test run cleaning to prevent the addition of unwanted organic fluids to the chamber such as cutting oil, or vacuum grease.
- Develop a mechanism for driving a solid block of copper in the frequency and displacement range necessary to produce VIDA so that, 1) the condenser surface may be considered effectively isothermal, 2) the temperature gradient in the block may be directly measured and extrapolated to the surface value, and 3) the mechanism does not produce significant heating of the condenser block. These precautions will allow for direct comparison to theory and greatly simplify the analysis.

- Find an instrument to measure displacement with sufficient resolution to capture 10 to 40 μm amplitude oscillations within a reasonable uncertainty. It may prove quite difficult to find an instrument which has both capability and geometric requirements that work well with the pressure vessel. Attention also must be paid that sufficient surface reflectance of the back of the driver can be obtained without having to resort to reflective tape, as this will preclude measurements during low pressure tests, as was the case in this study. Such an instrument will likely be prohibitively expensive as well. Only two instruments were found to be acceptable for the present study, one being a Polytech Laser Vibrometer, which had excellent accuracy, range, surface finish, and geometric parameters, but cost almost \$50,000, the other was less robust, the MTI-2000, used in this study, but still cost \$8,000, with possibility of rental as an option. However, this instrument required reflective tape on the back of the diaphragm which would necessarily ‘bubble’ under evacuation of the cylinder and consequently lose signal, so that displacement measurements during experiments were impossible. Other means of increasing the reflectivity of the driver backing may be determined which are viable under vacuum conditions. As yet, none have been determined.
- Provide for different regimes of coolant flow rate [31], based on the level of HT predicted and the expected temperature drop across the cooler, which should be minimized to approach a constant temperature sink. The delta T across the cooler may be monitored for an energy balance, but precision is not required due to the measurement of HF in the condenser block.

Procedure

- At the beginning of every testing session, have a 3 to 4 hour ‘blow-down’ of the apparatus, venting to atmosphere or through the vacuum pump with the heater on full power, if it is capable of handling large amounts of condensate. The current oil lubricated vacuum pump was not, and thus the oil had to be replaced almost every day.
- Do a FWC comparison run, requiring a completely clean metal surface, which was not achieved in this study. Extensive cleaning regimens that may be used or adapted were described in Le Fevre and Rose, 1965 [31], Finnicum and Westwater, 1989 [62], and Vukasinovic, 2002 [10].
- Allow ample time for steady state conditions to be reached for measurements. This may be as long as several hours in some cases.
- There are many potential surface promotion techniques, several of which are cataloged in the Surface Promotion section of Chapter 2. The best base case, for comparability with the Rose theory would be polished copper with an oleic acid coating. Further promoters might then be tested for comparison, such as the L-B film discussed in Zhao et al., 1996 [58]; the diamond like coating (DLC) tested in Koch et al., 1998 [14]; or bulk addition of promoter [37,53,65]. Though proven an

effective promoter, the PTFE coating with ion-implantation of Ma et al., 1999 [68] would likely impede the performance of the driver too much for feasibility.

APPENDIX A MATLAB CODES

DWC_HTC.m

```
function [h,heat_flux]=DWC_HTC(Tsat,Ts,r_max)

%      [h]=DWC_HTC(Tsat,Ts,r_max)
%      Tsat,  [K],          a constant value for the far-field vapor
% temperature of the steam
%      Ts,    [K],          a vector of surface temperature values
%      r_max, [m],          a vector of artificial maximum drop radius, for
%                          theoretical maximum radius, input r_max as zero
%      h,     [W/m2-K],     a scalar of the Heat Transfer Coefficient for a
% given subcooling and saturated vapor temperature, for dropwise
% condensation of pure water vapor on an iso-thermal surface. Theory
% offered by Le Fevre & Rose, 1966, and in modified form by Rose, 2002.
%
% units are m-g-s, except where noted otherwise

% This file represents the theoretical model from dropwise condensation
% of pure water vapor on an isothermal surface presented by Rose, 2002
% in a review of dropwise condensation. The original theory was
% offered by Le Fevre & Rose, 1966, and various adjustments to
% experimental constants were gathered in the review address by Rose in
% 2002.

% Check if Tsat is in K or not
if Tsat < 273

    Tsat = Tsat + 273;
    Ts    = Ts    + 273;

end

% Constants

g = 9.81; % acceleration of gravity, [m/s^2]
K1 = 2/3; % shape factor for steam, p.151, (Rose, 1998)
K2 = 1/2; % shape factor for steam, p.151, (Rose, 1998)
K3 = 0.4; % empirical constant, p.151, (Rose, 1998)
R = 461.5; % gas constant for water, RGAS.exe, [J/kg-K]
gamma=1.33; % specific heat ratio for steam, [ ]

% Properties - call PROPS function to interpolate thermophysical
% properties from steam tables

[rho_f,rho_g,hfg,k,k_g,sigma,Psat,mu_f,mu_g,Cp_f,Cp_g,Beta,alpha_f,...
alpha_g,nu_f,nu_g]=PROPS(Tsat);
```

```

% Variables

deltaT=Tssat-Ts;      % vector of surface subcooling values

if r_max==0

    r_max = K3 * (sigma/rhof/g)^0.5;      % Equation (8), maximum drop
    % radius prior to departure from original nucleation site end

% variables which do not involve either r_max, deltaT, or Ts

B=( 2*sigma*Tssat )/( rhof*hfg );
C=K1/k;
D=K2*0.627/0.664*Tssat*(gamma+1)/(hfg^2*rhog*(gamma1))*...
(R*Tssat/2/pi)^0.5;

% Initialize h
h=zeros(length(r_max),length(Ts));
heat_flux=zeros(length(r_max),length(Ts));

% dummy variables to save computations
dummy1=2*sigma/rhof/hfg*Tssat;

% Put separate loop out here for r_max variable so it is not
recalculated for every Ts value

% Define variables which involve r_max
for j=1:length(r_max)

    E(j)=(3*r_max(j)^(1/3))^(-1);

end

% Loop for Ts values
for i=1:length(deltaT)

    if deltaT(i) > 0

        % Define variables which involve deltaT, but not r_max

        % Equation (7), smallest thermodynamically viable drop radius
        r_min(i) = dummy1/deltaT(i);

        % Algebraic Intermediate Variables
        A=deltaT(i);

        % Define argument function to work with quadrature (numerical
        % integration) function, quadl
        arg= @(r) (A.*r + B)./(C.*r + D)./r.^(5/3);

        % Loop for r_max values
        for j=1:length(r_max)

            % Call function to perform numerical integration of
            % argument by adaptive quadrature

            heat_flux(j,i) = E(j)*quadl(arg,r_min(i),r_max(j));

```



```

        if heat_flux(j,i) < 0
            heat_flux(j,i) = 0;
        elseif Tsat-deltaT(i) < 273
            heat_flux(j,i) = 0;
        end

        % Convert to Heat Transfer Coefficient, h, [W/m2-K]
        h(j,i)=heat_flux(j,i)/deltaT(i);

    end % end of for (j) loop

end % end of if statement to make sure

end % end of for (i) loop

```

Dropwise_Condensation_Model.m

```

function
[q_theoretical,number_of_iterations]=Dropwise_Condensation_Model...
(Tsat,To)
% The implementation of DWC_HTC has been modified for this program
% to be used as a function, and so arguments must be checked with
% current iteration of DWC_HTC and this program before implementation

alpha=0.0;

Tsat=50; % Vapor Saturation Temp, [degC]
To=4; % Edge Temp, [degC]
c=0.004*25.4/1000; % Shim thickness, [m]
b=.75/2*25.4/1000; % Exposed Radius of Shim, [m]
len=5000; % Desired number of steps in r-vector
factor=50;
dr=b/len;
err=0.01; % Desired error between steps in iteration
q=100; % Total Heat Rate, [W]
k=140;

% Get Properties based on Tsat

[rho_f,rho_g,hfg,k,k_g,sigma,Psat,mu_f,mu_g,Cp_f,Cp_g,Beta,alpha_f,alph
a_g,nu_f,nu_g]=PROPS(Tsat);

% Set r_max to command for theoretical value use
r_max=0;

r=0:dr:b; % radius of vector values, [m]
h=zeros(length(r));
q_dp_r=zeros(length(r));
Ts=zeros(length(r));

```

```

m=length(r)-1;           % length of r-vector adjusted for temp profile
routine

% Initialize dummy variables
i=0;
number=1;
q_theory(1)=q;

while i==0               % Execute these commands until the error is below
                        % desired value

    [Ts]=exp_profile(Tsat,To,b,c,q_theory(number),m); % Obtain radial
    % temp profile from function

    % from this point, determine where the subcooling rises above 1.0K, and
    % only treat the remainder of the radial vector with the smaller dr

    number=number+1 %Print out the iteration number each time through

    [h,q_dp_r]=DWC_HTC(Tsat,Ts,r_max);           % Normal implemenation

    % Argument for area integral
    arg=r.*q_dp_r;

    % Approximate Integral with Simpson's Rule function
    [ans,err_order]=simpsons_rule(arg,dr);

    q_theory(number)=2*pi*(ans);

    q_theory(number)=(q_theory(number) + q_theory(number-1))/2 + alpha...
        * ( q_theory(number) - q_theory(number-1) )/2;

    %error_order=err_order

    % Compare differential
    diff=abs(q_theory(number-1)-q_theory(number))

    if err > diff

        break

    end

end % end of while loop that iterates the theoretical heat flux
calculation

number_of_iterations=number-1
q_theoretical=q_theory(number)
q_measured=q
percent_difference=(q_theoretical-q_measured)/q_measured*100

figure(1)
subplot(3,1,1)
plot(r*1000,Ts),grid
ylabel('\circC')
title('Imposed Ts(r), HTC(r), & q"(r)')

```

```

subplot(3,1,2)
plot(r*1000,h),grid
ylabel(' [W/m2-K]')

subplot(3,1,3)
plot(r*1000,q_dp_r),grid
ylabel(' [W/m2]')
xlabel('r, [m]')

% figure(2)
% bar([q,q_theory(number),diff]),grid
% xlabel('q_measured, q_theory, difference last step')
% ylabel(' [W]')
% title('Total Heat Rate Comparison')

```

Theoretical_Heat_Rate_Grid.m

```

clear all

Tsat=22:40;

To=10:17;

for i=1:length(Tsat)

    for j=1:length(To)

        [q_theory(i,j),number(i,j)]=Dropwise_Condensation_Model(Tsat(i)...
        ,To(j));

    end

end

figure(1)
plot(To,q_th),grid
xlabel(' [\circ C]')
ylabel(' [W]')
title('Theoretical Total Heat Rate vs. Edge Temperature and Saturation
Temperature')

iterations=num

```

DWC_Behavior.m

```

clear all
%
*****
% This program examines the behavior of the Heat Transfer Coefficient
for
% Dropwise Condensation of pure water vapor as a function of
%         1) Saturation Temperature
%         2) Subcooling
%         3) Maximum Droplet Size
%
*****

```

```

% Saturation Temperatures to be argued, [K]
Tsats=280:10:500;

% Subcoolings, [K]
deltaT=[0.1:0.1:0.9,1:19,20:10:50];

K3=0.4;      % Constant, [-]
g=9.81;      % Acceleration of gravity, [m/s2]

for i=1:length(Tsats)

[rho_f,rho_g,hfg,k_f,k_g,sigma,Psat,mu_f,mu_g,Cp_f,Cp_g,Beta,alpha_f,alpha_g,nu_f,nu_g]=PROPS(Tsats(i));

    % Theoretical Maximum Drop Radius, Equation (8), (Rose, 2002)
    r_max_th(i) = K3 * (sigma/rho_f/g)^0.5;

    % Smallest thermodynamically viable drop radius, (Rose, 2004)
    % only for informational purpose, not fed to any subroutine in this
    % program
    r_min(:,i)=2*sigma*Tsats(i)/rho_f/hfg./deltaT;

    [h(:,i),HF(:,i)]=DWC_HTC(Tsats(i),Tsats(i)-deltaT,r_max_th(i));

end

%*****
% Now look at r-max dependance
%*****

% r_max in [m], Tsat & deltaT in [K]
r_max=[1e-8,5e-8,1e-7,5e-7,1e-6,5e-6,1e-5,5e-5,1e-4,5e-4,1e-3,5e-3,1e-2];
Tsats_r=[280,320,380,440,500];
deltaTr=[0.1,0.5,1,5,10,20,50];

for i=1:length(Tsats_r)

    [hr(:, :, i), HFr(:, :, i)]=DWC_HTC(Tsats_r(i),Tsats_r(i)-deltaTr,r_max);

end

% h vs. Tsat for 5 values of deltaT
figure(1)
semilogy(Tsats,h(1,:)/10^6,'b',Tsats,h(10,:)/10^6,'r',Tsats,h(19,:)/10^6,'g',Tsats,h(length(deltaT),:)/10^6,'k'),grid
title('DWC HTC vs. Tsat for \DeltaT = 0.1, 1.0, 10, 50K')
xlabel('Saturation Temperature, [K]')
ylabel('HTC, [MW/m^2K]')

% h vs. deltaT for 5 values of Tsat
figure(2)
loglog(deltaT,h(:,1)/10^6,'b',deltaT,h(:,5)/10^6,'r',deltaT,h(:,11)/10^6,'g',deltaT,h(:,16)/10^6,'m',deltaT,h(:,length(Tsats))/10^6,'k'),grid
title('DWC HTC vs. \DeltaT_s_u_b for Tsat = 280, 320, 380, 430, 500K')
xlabel('\DeltaT_s_u_b, [K]')

```

```

ylabel('HTC, [MW/m^2K]')

% HF vs. Tsat for 5 values of deltaT
figure(3)
semilogy(Tsat,HF(1,:)/10^6,'b',Tsat,HF(10,:)/10^6,'r',Tsat,HF(19,:)/10^
6,'c',Tsat,HF(length(deltaT),:)/10^6,'k'),grid
title('DWC Heat Flux vs. Tsat for \DeltaT = 0.1, 1.0, 10, 20, 50K')
xlabel('Saturation Temperature, [K]')
ylabel('HF, [MW/m^2]')

% HF vs. deltaT for 5 values of Tsat
figure(4)
loglog(deltaT,HF(:,1)/10^6,'b',deltaT,HF(:,5)/10^6,'r',deltaT,HF(:,11)/
10^6,'c',deltaT,HF(:,16)/10^6,'m',deltaT,HF(:,length(Tsat))/10^6,'k'),g
rid
title('DWC Heat Flux vs. \DeltaT_s_u_b for Tsat = 280, 320, 380, 430,
500K')
xlabel('\DeltaT_s_u_b, [K]')
ylabel('HF, [MW/m^2]')

% h vs. r_max all deltaT, representative Tsat = 380K, Psat ~1atm
figure(5)
loglog(r_max*1000,hr(:, :, 3)/10^6),grid
title('DWC HTC vs. r_m_a_x for \DeltaT = 0.1, 0.5, 1.0, 5.0, 10, 20,
50K at Tsat = 380K')
xlabel('Max Droplet Radius, [mm]')
ylabel('HTC, [MW/m^2K]')

n=length(r_max);
m=length(deltaT_r);
o=length(Tsat_r);

% Loop to reassign hr variable for easier plotting
for s=1:length(Tsat_r)

    for t=1:length(r_max)

        hr_DT1(t,s)=hr(t,3,s);
        HFr_DT1(t,s)=HFr(t,3,s);

    end

end

% h vs. r_max all Tsat, representative deltaT=1
figure(6)
loglog(r_max*1000,hr_DT1/10^6),grid
title('DWC HTC vs. r_m_a_x for Tsat = 280, 320, 380, 440, 500K at
\DeltaT = 1.0K')
xlabel('Max Droplet Radius, [mm]')
ylabel('HTC, [MW/m^2K]')

% Compare range of deltaT and Tsat effects with high and low deltaTs
for Hi
% mid and low Tsat values
figure(7)

```

```

loglog(r_max*1000,hr(:,1,1)/10^6,'b',r_max*1000,hr(:,4,1)/10^6,'b',r_max*1000,hr(:,1,3)/10^6,'r',r_max*1000,hr(:,m,3)/10^6,'r',r_max*1000,hr(:,1,o)/10^6,'k',r_max*1000,hr(:,m,o)/10^6,'k'),grid
title('DWC HTC vs. r_m_a_x for \DeltaT = 0.1 & 5K at Tsat = 280 and \DeltaT = 0.1 & 50K for 380 & 500K')
xlabel('Max Droplet Radius, [mm]')
ylabel('HTC, [MW/m^2K]')

% HF vs. r_max all deltaT, representative Tsat = 380K, Psat ~1atm
figure(8)
loglog(r_max*1000,HFr(:, :, 3)/10^6),grid
title('DWC Heat Flux vs. r_m_a_x for \DeltaT = 0.1, 0.5, 1.0, 5.0, 10, 20, 50K at Tsat = 380K')
xlabel('Max Droplet Radius, [mm]')
ylabel('HF, [MW/m^2]')

% HF vs. r_max all Tsat, representative deltaT=1
figure(9)
loglog(r_max*1000,HFr_DT1/10^6),grid
title('DWC Heat Flux vs. r_m_a_x for Tsat = 280, 320, 380, 440, 500K at \DeltaT = 1.0K')
xlabel('Max Droplet Radius, [mm]')
ylabel('HF, [MW/m^2]')

% Compare range of deltaT and Tsat effects with high and low deltaTs for Hi
% mid and low Tsat values
figure(10)
loglog(r_max*1000,HFr(:,1,1)/10^6,'b',r_max*1000,HFr(:,4,1)/10^6,'b',r_max*1000,HFr(:,1,3)/10^6,'r',r_max*1000,HFr(:,m,3)/10^6,'r',r_max*1000,HFr(:,1,o)/10^6,'k',r_max*1000,HFr(:,m,o)/10^6,'k'),grid
title('DWC Heat Flux vs. r_m_a_x for \DeltaT = 0.1 & 5K at Tsat = 280 and \DeltaT = 0.1 & 50K for 380 & 500K')
xlabel('Max Droplet Radius, [mm]')
ylabel('HF, [MW/m^2]')

figure(11)
plot(Tsat,r_max_th*1000),grid
title('Maximum theoretical droplet radius vs. Tsat')
xlabel('saturation temperature, [K]')
ylabel('[mm]')

figure(12)
semilogy(Tsat,r_min(1,:)*1e9,Tsat,r_min(10,:)*1e9,Tsat,r_min(19,:)*1e9,Tsat,r_min(length(deltaT),:)*1e9),grid
title('Smallest viable droplet radius vs. Tsat, \DeltaT = 0.1, 1.0, 10, & 50K ')
xlabel('saturation temperature, [K]')
ylabel('[nm]')

```

Get_Theoretical_THR_and_r_eff.m

```
clear all
```

```
% % Feb 21 through Mar 9 data streams - out of current range, need to improve
```

```

% % range of model before proceeding
% Ts = [33.6 27.4 28.3 29.6 29.8 31.2 32.3 30.7 30.2 33.1 35.3 35.7
36.5 37.9 36.9 30.9 31.2 31.1 29.6 29.4 29.7 30.0 30.2 30.3 30.8
30.9 30.7 31.5 29.0 29.3 37.8 36.9 36.2 36.3 35.2 34.8 26.1 25.6 24.9
25.1 26.2 24.2 25.3 24.7 26.8 27.2 26.4 26.1 26.2 24.7 25.2 ];
%
% sigma_Ts=[0.22 0.44 0.33 0.33 0.33 0.44 0.78 0.28 0.17 0.22 0.22
0.28 0.28 0.28 0.04 0.07 0.02 0.78 0.11 0.28 0.39 0.39 0.33 0.33
0.22 1.83 0.02 0.02 0.03 0.17 0.39 0.22 0.08 0.28 0.17 0.11 0.22
0.11 0.11 0.17 0.39 0.17 0.28 0.17 0.2 0.67 0.28 0.39 0.39 0.22 0.17
];
%
% Te = [16.1 15.2 15.9 14.7 12.7 11.3 11.1 18.9 12.0 12.3 11.6 11.2
10.3 9.9 14.3 12.8 12.8 8.9 14.5 9.6 8.7 8.3 8.7 8.7 8.7 8.7 13.6
7.8 8.2 7.5 10.8 9.7 8.3 6.1 14.8 14.6 13.2 13.3 11.9 12.2 13.8 13.6
8.3 13.8 13.9 13.8 13.0 12.4 12.4 12.2 12.8 ];
%
% sigma_Te=[0.17 0.06 0.11 0.17 0.11 0.17 0.22 0.11 0.07 0.50 0.11 0.11
0.11 0.08 0.09 0.09 0.17 0.09 0.17 0.28 0.28 0.22 0.22 0.17 0.17 0.17
0.03 0.11 0.17 0.02 0.44 0.39 0.11 0.11 0.11 0.17 0.08 0.11 0.07 0.11
0.22 0.11 0.11 0.11 0.17 0.07 0.07 0.09 0.09 0.08 0.11 ];
%
% q_exp=[12.2 25.6 24.3 16.6 13.3 12.7 8.7 23.9 22.7 20 19.3 15.9 14.5
13.2 11.9 9.3 9.1 2.9 9.6 9.9 8.2 7 8.5 8.6 8.6 8.7 9.6 6.9 7.3 6.9
13.5 12.8 12.2 8.9 25 26 30 29 20 21.9 30 26 36 33 36 33.3 31 29.1 29.7
26.1 27.5 ];
%
% sigma_q=[0.6 0.8 1.6 0.9 0.9 1.1 1.7 0.3 1.9 1.5 1.5 1.8 1.5 1.2 0.5
0.4 0.3 1.6 0.7 1.6 1.4 1.6 1.5 1.5 1.4 1.3 0.3 0.6 0.6 0.6 1.9 1.8 1.5
1.4 2 1.9 2 2 1.8 1.7 3 2 2 2 2 1.7 3 1.6 1.8 1.6 1.6 ];

for i=13:length(Ts)

[q_th,r_max,sigma,r_eff,sigma_r]=Heat_Rate_Archive(Ts(i),sigma_Ts(i),Te
(i),sigma_Te(i),q_exp(i),sigma_q(i));

    q_theory(i)=q_th(1);
    sigma_q_th(i)=sigma(1);
    r_effect(i)=r_eff;
    sigma_r_effect(i)=sigma_r;

end

q_theory=q_theory.'
sigma_q_theory=sigma_q_th.'
r_effective=r_effect.'
sigma_r_effective=sigma_r_effect.'

```

Heat_Rate_Archive.m

```

function
[q_th,r_max,sigma,r_eff,sigma_r]=Heat_Rate_Archive(Ts,sigma_Ts,Te,sigma
_Te,q_exp,sigma_q)
%
[q_th,r_max,sigma,r_eff,sigma_r]=Heat_Rate_Archive(Ts,sigma_Ts,Te,sigma
_T

```

```

% e,q_exp,sigma_q)
% This function uses arrays of theoretical total heat rate values
% calculated in another program and archived here, for 5 different
values
% of maximum drop radius in dropwise condensation mode of pure water
% vapor on one face of a vertically oriented, circular brass shim
% 0.75 in in diameter and 0.004 in thick, theory used for calculating
the
% heat flux given by Le Fevre and Rose, 1966
%
% given:
%
%     Ts      = measured saturation temperature, [C] between 22 and 40
%
%     sigma_Ts = uncertainty in Ts, [C]
%
%     Te      = measured edge temperature, [C] between 10 and 18
%
%     sigma_Te = uncertainty in Te, [C]
%
% return:
%
%     q_th [W]= 8 values for the theoretical heat corresponding to the
%                respective values of r_max, theoretical, 0.01, 0.1,
%                0.25, 0.5, 1, 2, & 4 mm
%
%     r_max [mm] = maximum droplet radii corresponding to the values
%                in q_th
%
%     sigma [W]  = uncertainty in theoretical total heat rate due to
%                argument uncertainty
%
%     r_eff [mm] = estimation of effective maximum droplet diameter
%                that would yield the experimental total heat rate
%                under the given conditions
%
%*****

% % Test inputs
% Ts=33.4;
% sigma_Ts=.2;
% Te=16.7;
% sigma_Te=.1;
% q_exp=22.35;
% sigma_q=1.5;

Ts=24:2:50;

To=4:4:20;

A=length(Ts);

B=length(To);

% Determine bin number (which arguments it is between) of saturation
temperature input
dummy=0;

```



```

k=0;
while dummy==0

    k=k+1;

    if Ts >= Tsat(k) & Ts < Tsat(k+1)

        Y=k;

        break

    end

end

% Determine bin number of edge temperature input
dummy=0;
k=0;
while dummy==0

    k=k+1;

    if Te >= To(k) & Te < To(k+1)

        X=k;

        break

    end

end

% 0 = theoretical maximum droplet radius, rest in mm
r_max=[0 .01 .1 .25 .5 1 2 4];

C=length(r_max);

% Initialize Q array,
% (theoretical Heat Rate values specific to this experiment)
Q=zeros(A,B,C);

% Q for theoretical r_max, which should vastly underestimate HT for
this exp.
Q(:, :, 1)=[ 40.19 31.91 23.67 15.51 7.48
              45.86 37.27 28.72 20.23 11.84
              51.78 42.89 34.03 25.23 16.51
              57.97 48.77 39.61 30.51 21.47
              64.71 55.17 45.67 36.22 26.83
              71.40 61.57 51.78 42.04 32.35
              78.67 68.51 58.40 48.32 38.30
              86.16 75.69 65.26 54.86 44.51
              93.93 83.15 72.40 61.68 51.02
              102.34 91.21 80.10 69.03 58.01
              110.63 99.18 87.77 76.40 65.07
              119.60 107.81 96.06 84.34 72.66
              128.78 116.66 104.57 92.52 80.50
              138.23 125.78 113.36 100.98 88.63    ];

```

% Q for r_max of 0.01mm which should overestimate HT for this exp.

```
Q(:, :, 2) = [ 84.58  67.09  49.72  32.52  15.62
               96.73  78.55  60.47  42.54  24.84
               109.42 90.56  71.80  53.17  34.74
               122.69 103.17 83.74  64.43  45.28
               137.17 116.90 96.72  76.64  56.71
               151.52 130.62 109.80 89.08  68.49
               167.14 145.52 123.98 102.53 81.20
               183.25 160.94 138.70 116.54 94.51
               199.95 176.95 154.02 131.17 108.43
               218.05 194.27 170.57 146.95 123.43
               235.83 211.39 187.03 162.74 138.55
               255.11 229.92 204.81 179.77 154.82
               274.83 248.92 223.08 197.32 171.64
               295.13 268.50 241.94 215.46 189.07 ];
```

% Q for r_max of 0.1mm which should overestimate HT for this exp.

```
Q(:, :, 3) = [ 59.89  47.54  35.26  23.10  11.14
               68.32  55.51  42.77  30.12  17.63
               77.12  63.86  50.67  37.56  24.57
               86.31  72.61  58.97  45.41  31.95
               96.31  82.11  67.97  53.89  39.91
               106.23 91.61  77.04  62.53  48.12
               117.00 101.90 86.84  71.85  56.94
               128.11 112.54 97.02  81.55  66.17
               139.61 123.58 107.59 91.66  75.81
               152.06 135.50 119.00 102.55 86.17
               164.29 147.30 130.35 113.45 96.62
               177.54 160.04 142.59 125.18 107.84
               191.10 173.11 155.16 137.27 119.44
               205.03 186.57 168.14 149.77 131.45 ];
```

% Q for r_max of 0.25mm which should overestimate HT for this exp.

```
Q(:, :, 4) = [ 51.51  40.89  30.34  19.88   9.59
               58.75  47.74  36.79  25.91  15.17
               66.31  54.91  43.57  32.30  21.14
               74.21  62.43  50.70  39.04  27.48
               82.79  70.59  58.43  46.33  34.32
               91.31  78.74  66.22  53.76  41.37
               100.56 87.58  74.65  61.76  48.95
               110.10 96.72  83.38  70.10  56.87
               119.98 106.20 92.47  78.78  65.16
               130.66 116.44 102.26 88.13  74.05
               141.17 126.57 112.01 97.49  83.03
               152.55 137.52 122.52 107.57 92.67
               164.19 148.74 133.32 117.95 102.63
               176.16 160.30 144.47 128.68 112.95 ];
```

% Q for r_max of 0.5mm

```
Q(:, :, 5) = [ 45.86  36.41  27.01  17.70   8.54
               52.30  42.50  32.75  23.07  13.51
               59.03  48.89  38.79  28.76  18.82
               66.06  55.58  45.14  34.76  24.46
               73.71  62.84  52.02  41.25  30.56
               81.29  70.10  58.96  47.86  36.83
               89.53  77.97  66.46  54.99  43.58
```

```

98.02  86.11  74.24  62.41  50.64
106.82  94.55  82.32  70.14  58.01
116.33 103.67  91.05  78.47  65.94
125.69 112.69  99.73  86.80  73.93
135.83 122.44 109.09  95.78  82.52
146.19 132.44 118.71 105.03  91.39
156.86 142.73 128.64 114.58 100.57 ];

% Q for r_max of 1mm
Q(:, :, 6) = [ 40.76  32.36  24.01  15.73   7.59
46.50  37.79  29.12  20.51  12.01
52.48  43.46  34.49  25.57  16.73
58.74  49.42  40.14  30.91  21.75
65.54  55.88  46.26  36.68  27.17
72.29  62.34  52.43  42.56  32.75
79.62  69.34  59.10  48.90  38.76
87.18  76.58  66.02  55.50  45.03
95.00  84.10  73.22  62.39  51.60
103.47  92.21  80.99  69.79  58.65
111.81 100.24  88.71  77.22  65.76
120.83 108.92  97.04  85.20  73.41
130.06 117.82 105.61  93.43  81.30
139.55 126.99 114.45 101.94  89.48 ];

% Q for r_max of 2mm
Q(:, :, 7) = [ 36.20  28.74  21.32  13.97   6.74
41.29  33.56  25.86  18.22  10.67
46.61  38.60  30.63  22.71  14.86
52.17  43.89  35.65  27.46  19.32
58.22  49.64  41.09  32.59  24.14
64.22  55.38  46.58  37.81  29.10
70.74  61.61  52.51  43.45  34.44
77.46  68.05  58.67  49.32  40.02
84.43  74.74  65.07  55.44  45.85
91.97  81.96  71.98  62.03  52.13
99.38  89.10  78.85  68.63  58.45
107.41  96.82  86.27  75.74  65.25
115.62 104.74  93.89  83.06  72.28
124.07 112.90 101.75  90.63  79.55 ];

% Q for r_max of 0.1mm which should overestimate HT for this exp.
Q(:, :, 8) = [ 32.11  25.49  18.92  12.40   5.98
36.64  29.77  22.94  16.16   9.46
41.36  34.26  27.18  20.15  13.19
46.30  38.96  31.64  24.37  17.15
51.68  44.06  36.47  28.92  21.43
57.01  49.17  41.35  33.57  25.83
62.81  54.70  46.62  38.58  30.58
68.78  60.43  52.09  43.79  35.53
74.98  66.37  57.79  49.23  40.72
81.68  72.79  63.93  55.09  46.30
88.27  79.14  70.04  60.96  51.92
95.41  86.01  76.63  67.28  57.97
102.72  93.05  83.41  73.80  64.21
110.24 100.31  90.41  80.53  70.68 ];

% Interpolation between the indexes determined for Ts and Te

```

```

% that is, determine five values of theoretical total heat rate, for
% one for each value of r_max

for p=1:C

    q1      = (Ts - Tsat(Y)) / (Tsat(Y+1) - Tsat(Y)) * ( Q(Y+1,X,p) -
Q(Y,X,p) ) + Q(Y,X,p) ;
    q2      = (Ts - Tsat(Y)) / (Tsat(Y+1) - Tsat(Y)) * (Q(Y+1,X+1,p) -
Q(Y,X+1,p)) + Q(Y,X+1,p);
    q_th(p) = (Te - To(X)) / ( To(X+1) - To(X) ) * (      q2      -
q1      ) +      q1      ;

end

% Now determine range of q from uncertainty, assumes within same index
% range as nominal value, an relatively inconsequential assumption,
given
% the linearity of the Q array

for p=1:C

    q1      = (Ts + sigma_Ts - Tsat(Y)) / (Tsat(Y+1) - Tsat(Y)) * (
Q(Y+1,X,p) - Q(Y,X,p) ) + Q(Y,X,p) ;
    q2      = (Ts + sigma_Ts - Tsat(Y)) / (Tsat(Y+1) - Tsat(Y)) *
(Q(Y+1,X+1,p) - Q(Y,X+1,p)) + Q(Y,X+1,p);
    q_th_hi(p) = (Te - sigma_Te - To(X)) / ( To(X+1) - To(X) ) * (
q2      -      q1      ) +      q1      ;

end

for p=1:C

    q1      = (Ts - sigma_Ts - Tsat(Y)) / (Tsat(Y+1) - Tsat(Y)) * (
Q(Y+1,X,p) - Q(Y,X,p) ) + Q(Y,X,p) ;
    q2      = (Ts - sigma_Ts - Tsat(Y)) / (Tsat(Y+1) - Tsat(Y)) *
(Q(Y+1,X+1,p) - Q(Y,X+1,p)) + Q(Y,X+1,p);
    q_th_lo(p) = (Te + sigma_Te - To(X)) / ( To(X+1) - To(X) ) * (
q2      -      q1      ) +      q1      ;

end

unc_lo=q_th-q_th_lo;
unc_hi=q_th_hi-q_th;

% determine higher uncertainty in q_th and assign to sigma
for p=1:C

    if unc_lo(p) > unc_hi(p)

        sigma(p)=unc_lo(p);

    else

        sigma(p)=unc_hi(p);

    end

end

```

```

end

% now determine the effective maximum droplet radius from exp. q
% use a Lagrange Interpolatoin Polynomial, cited at wolfram.com by Eric
% Weisstein
% exclude theoretical r_max from interpolation formula because of its
% varying value with saturation temperature

% attempt at least squares fit of  $q_{th}(r)=C/r^N+B$ 

% Drop theoretical max drop radius values from consideration for
finding
% r_eff
r=r_max(2:length(r_max));

qi=q_th(2:length(q_th));

b=(-100:10);
c=(0:100);
n=(1:100)*1e-2;
dummy=0;
counter=1

while counter < 5

    Ri=ones(length(b),length(c),length(n));
    i=[];
    j=[];
    k=[];

    for i=1:length(b)

        for j=1:length(c)

            for k=1:length(n)

                Ri(i,j,k)=sum( ( c(j)./r.^n(k) + b(i) - qi ).^2 );

            end

        end

    end

    [JKres,Iint]=min(Ri);

    [Kres,Jint]=min(JKres);

    [res,K]=min(Kres)

    J=Jint(:, :, K);
    I=Iint(:, J, K);

    B=b(I);
    C=c(J);
    N=n(K);

```

```

    if Ri(I,J,K) < .001*q_exp
        dummy=1;
        break
    end

    f=10^counter

    db=1/f;
    dc=1/f;
    dn=1/f;

    b=(B-20*db):db:(B+20*db);
    c=(C-20*db):dc:(C+20*db);
    n=(N-20*db):dn:(N+20*db);

    counter=counter+1

end

% establish data fit to theoretical total heat rate for given input
% temperature data
x=min(r)/10:min(r)/10:max(r)*10;
fit=C./x.^N+B;

% figure(1)
% semilogx(x,fit,r,qi,'o'),grid

% now determine r_effective from q_exp and q_th values

% avoid index finding of r_eff if q_exp out of range of fit
if q_exp + sigma_q > max(fit)

    r_eff=0;
    sigma_r = 0;
    return

elseif q_exp - sigma_q < min(fit)

    r_eff=0;
    sigma_r = 0;
    return

end

% determine index in fit the corresponds to r_eff
for i=1:length(x)-1

    if q_exp < fit(i) & q_exp >= fit(i+1)

        r_eff = x(i);
        break

    end
end

```

```

end

% Now determine uncertainty in r_eff

% lower limit for r_eff
for i=1:length(x)-1

    if q_exp+sigma_q < fit(i) & q_exp+sigma_q >= fit(i+1)

        r_eff_lo = x(i);
        break

    end

end

% upper limit for r_eff
for i=1:length(x)-1

    if q_exp - sigma_q < fit(i) & q_exp - sigma_q >= fit(i+1)

        r_eff_hi = x(i);
        break

    end

end

% test to see which error is higher and use that as the uncertainty
if r_eff_hi - r_eff > r_eff_lo - r_eff

    sigma_r = r_eff_hi - r_eff;

else

    sigma_r = r_eff_lo - r_eff

end

% % Test outputs
% q_theoretical=q_th
% uncertainty_in_q_theoretical=sigma
% r_max_values=r_max
% effective_max_drop_radius=r_eff
% uncertainty_in_r_eff = sigma_r
%
% figure(1)
% semilogx(r_max,q_th,'o',x,fit),grid
% title('Theoretical Total Heat Rate vs. Maximum Drop Radius')
% xlabel('[mm]')
% ylabel('[W]')

```

PROPS.m

```

function
[rho_f,rho_g,hfg,k_f,k_g,sigma,Psat,mu_f,mu_g,Cp_f,Cp_g,Beta,alpha_f,alpha_g,nu_f,nu_g]=PROPS(Tsat)
% [rho_f,rho_g,hfg,k_f,k_g,sigma,Psat,mu_f,mu_g,Cp_f,Cp_g,Beta,alpha_f,alpha_g,nu_f,nu_g]=PROPS(Tsat)
%
% Given Tsat in degrees Kelvin and pure water vapor, return:
%
% rho_f = density of liquid at Ts, [kg/m3]
% rho_g = density of vapor at Tsat, [kg/m3]
% hfg = enthalpy of vaporization, [J/kg]
% k_f = thermal conductivity, [W/m-K]
% k_g = thermal conductivity, [W/m-K]
% sigma = surface tension, [kg/s2]=[N/m]
% Psat = saturation pressure, [bars]
% mu_f = dynamic viscosity, [N*s/m2]=[kg/m-s]
% mu_g = dynamic viscosity, [N*s/m2]
% Cp_f = Constant Pressure Specific Heat, [J/kg-K]
% Cp_g = Constant Pressure Specific Heat, [J/kg-K]
% Beta = Coefficient of Thermal Expansion, [1/K]
% alpha_f = Thermal Diffusivity, [m2/s]
% alpha_g = Thermal Diffusivity, [m2/s]
% nu_f = Kinematic Viscosity, [m2/s]
% nu_g = Kinematic Viscosity, [m2/s]
%
% Program valid for Tsat = (275,500] K
%
% Data taken from Incropera and DeWitt, 1996, p.846

% Tsat, [K]
T = [ 275 , 280 , 285 , 290 , 295 , 300 , 305 ,
310 , 315 , 320 , 325 , 330 , 335 , 340 , 345 , 350 ,
355 , 360 , 365 , 370 , 375 , 380 , 385 , 390 , 400 ,
410 , 420 , 430 , 440 , 450 , 460 , 470 , 480 , 490 ,
500 ];

% specific volume of saturated liquid, [m3/g]
v_f = [ 1.000 , 1.000 , 1.000 , 1.001 , 1.002 , 1.003 , 1.005 ,
1.007 , 1.009 , 1.011 , 1.013 , 1.016 , 1.018 , 1.021 , 1.024 , 1.027 ,
1.030 , 1.034 , 1.038 , 1.041 , 1.045 , 1.049 , 1.053 , 1.058 , 1.067 ,
1.077 , 1.088 , 1.099 , 1.110 , 1.123 , 1.137 , 1.152 , 1.167 , 1.184 ,
1.203 ]*1e-3;

% specific volume of saturated vapor, [m3/g]
v_g = [ 181.7 , 130.4 , 99.4 , 69.7 , 51.94 , 39.13 , 29.74 ,
22.93 , 17.82 , 13.98 , 11.06 , 8.82 , 7.09 , 5.74 , 4.683 , 3.846 ,
3.180 , 2.645 , 2.212 , 1.861 , 1.574 , 1.337 , 1.142 , 0.980 , 0.731 ,
0.553 , 0.425 , 0.331 , 0.261 , 0.208 , 0.167 , 0.136 , 0.111 , .0922 ,
.0766 ];

% enthalpy of vaporization, [J/g]
hfg_d = [ 2497 , 2485 , 2473 , 2461 , 2449 , 2438 , 2426 ,
2414 , 2402 , 2390 , 2378 , 2366 , 2354 , 2342 , 2329 , 2317 ,
2304 , 2291 , 2278 , 2265 , 2252 , 2239 , 2225 , 2212 , 2183 ,

```



```
2153 , 2123 , 2091 , 2059 , 2024 , 1989 , 1951 , 1912 , 1870 ,
1825 ]*1e3;
```

```
% thermal conductivity of saturated liquid, [W/m-K]
```

```
k_fd = [ 574 , 582 , 590 , 598 , 606 , 613 , 620 ,
628 , 634 , 640 , 645 , 650 , 656 , 660 , 668 , 668 ,
671 , 674 , 677 , 679 , 681 , 683 , 685 , 686 , 688 ,
688 , 688 , 685 , 682 , 678 , 673 , 667 , 660 , 651 ,
642 ]*1e-3;
```

```
% thermal conductivity of saturated vapor, [W/m-K]
```

```
k_gd = [ 18.3 , 18.6 , 18.9 , 19.3 , 19.5 , 19.6 , 20.1 ,
20.4 , 20.7 , 21.0 , 21.3 , 21.7 , 22.0 , 22.3 , 22.6 , 23.0 ,
23.3 , 23.7 , 24.1 , 24.5 , 24.9 , 25.4 , 25.8 , 26.3 , 27.2 ,
28.2 , 29.8 , 30.4 , 31.7 , 33.1 , 34.6 , 36.3 , 38.1 , 40.1 ,
42.3 ]*1e-3;
```

```
% surface tension of saturated liquid, [kg/s2] = [N/m]
```

```
sigma_d = [ 75.3 , 74.8 , 74.3 , 73.7 , 72.7 , 71.7 , 70.9 ,
70.0 , 69.2 , 68.3 , 67.5 , 66.6 , 65.8 , 64.9 , 64.1 , 63.2 ,
62.3 , 61.4 , 60.5 , 59.5 , 58.6 , 57.6 , 56.6 , 55.6 , 53.6 ,
51.5 , 49.4 , 47.2 , 45.1 , 42.9 , 40.7 , 38.5 , 36.2 , 33.9 ,
31.6 ]*1e-3;
```

```
% saturation pressure, [bar]
```

```
Psat_d = [ .00697 , .00990 , .01387 , .01917 , .02617 , .03531 , .04712 ,
.06221 , .08132 , .1053 , .1351 , .1719 , .2167 , .2713 , .3372 , .4163 ,
.5100 , .6209 , .7514 , .9040 , 1.0815 , 1.2869 , 1.5233 , 1.794 , 2.455 ,
3.302 , 4.370 , 5.699 , 7.333 , 9.319 , 11.71 , 14.55 , 17.90 , 21.83 ,
26.40 ];
```

```
% dynamic viscosity of saturated liquid, [N*s/m2]
```

```
mu_fd = [ 1652 , 1422 , 1225 , 1080 , 959 , 855 , 769 ,
695 , 631 , 577 , 528 , 489 , 453 , 420 , 389 , 365 ,
343 , 324 , 306 , 289 , 274 , 260 , 248 , 237 , 217 ,
200 , 185 , 173 , 162 , 152 , 143 , 136 , 129 , 124 ,
118 ]*1e-6;
```

```
% dynamic viscosity of saturated vapor, [N*s/m2]
```

```
mu_gd = [ 8.09 , 8.29 , 8.49 , 8.69 , 8.89 , 9.09 , 9.29 ,
9.49 , 9.69 , 9.89 , 10.09 , 10.29 , 10.49 , 10.69 , 10.89 , 11.09 ,
11.29 , 11.49 , 11.69 , 11.89 , 12.09 , 12.29 , 12.49 , 12.69 , 13.05 ,
13.42 , 13.79 , 14.14 , 14.50 , 14.85 , 15.19 , 15.54 , 15.88 , 16.23 ,
16.59 ]*1e-6;
```

```
% Coefficient of Thermal Expansion, [1/K]
```

```
beta_f = [-32.74 , 46.04 , 114.1 , 174.0 , 227.5 , 276.1 , 320.6 ,
361.9 , 400.4 , 436.7 , 471.2 , 504.2 , 535.5 , 566.0 , 595.4 , 624.2 ,
652.3 , 697.9 , 707.1 , 728.7 , 761 , 788 , 814 , 841 , 896 ,
952 , 1010 , 0 , 0 , 0 , 0 , 0 , 0 , 0 ,
0 ]*1e-6;
```

```
% Constant Pressure Specific Heat of Saturated Liquid, [J/kg-K]
```

```
Cp_fd = [ 4.211 , 4.198 , 4.189 , 4.184 , 4.181 , 4.179 , 4.178 ,
4.178 , 4.179 , 4.180 , 4.182 , 4.184 , 4.186 , 4.188 , 4.191 , 4.195 ,
4.199 , 4.203 , 4.209 , 4.214 , 4.220 , 4.226 , 4.232 , 4.239 , 4.256 ,
```

```

4.278 , 4.302 , 4.331 , 4.36 , 4.40 , 4.44 , 4.48 , 4.53 , 4.59 ,
4.66 ]*1e3;

% Constant Pressure Specific Heat of Saturated Vapor, [J/kg-K]
Cp_gd = [ 1.855 , 1.858 , 1.861 , 1.864 , 1.868 , 1.872 , 1.877 ,
1.882 , 1.888 , 1.895 , 1.903 , 1.911 , 1.920 , 1.930 , 1.941 , 1.954 ,
1.968 , 1.983 , 1.999 , 2.017 , 2.036 , 2.057 , 2.080 , 2.104 , 2.158 ,
2.221 , 2.291 , 2.369 , 2.46 , 2.56 , 2.68 , 2.79 , 2.94 , 3.10 ,
3.27 ]*1e3;

% establish length of data record for reference
index=length(T);

% test Tsat input to see if in celius instead of kelvin
if Tsat < 230

    Tsat = Tsat + 273.15;          % Convert Tsat to Kelvin temp scale

elseif Tsat <= 275

    print('error = temperature input too low to PROPS subroutine, must
be between 275 and 400 K')

    return

elseif Tsat > 500

    print('error = temparature input too high to PROPS subroutine, must
be between 275 and 400K')

    return

end

for i=1:index-1

    if Tsat > T(i) & Tsat <= T(i+1)

        j=i; % sets the j index value to the LHS side of the interval
in the data table
        break

    end

end

% use linear interpolation to determine the property value
% more accurate method possible, but not warranted given the low
accuracy of
% the experimental results, unwarranted --- what are the error
estimates of
% each method? i.e. how do you know? I don't know, I'm lazy and can't
find an example of log interpolation.

rho_f = ( (Tsat-T(j))/(T(j+1)-T(j)) * (v_f(j+1)-v_f(j)) + v_f(j) )^(-
1);

```

```

rho_g    = ( (Tsat-T(j))/(T(j+1)-T(j)) * (v_g(j+1)-v_g(j)) + v_g(j) )^(-
1);

hfg      = (Tsat-T(j))/(T(j+1)-T(j)) * (hfg_d(j+1)-hfg_d(j)) +
hfg_d(j);

k_f      = (Tsat-T(j))/(T(j+1)-T(j)) * (k_fd(j+1)-k_fd(j)) + k_fd(j);

k_g      = (Tsat-T(j))/(T(j+1)-T(j)) * (k_gd(j+1)-k_gd(j)) + k_gd(j);

sigma    = (Tsat-T(j))/(T(j+1)-T(j)) * (sigma_d(j+1)-sigma_d(j)) +
sigma_d(j);

Psat     = (Tsat-T(j))/(T(j+1)-T(j)) * (Psat_d(j+1)-Psat_d(j)) +
Psat_d(j);

mu_f     = (Tsat-T(j))/(T(j+1)-T(j)) * (mu_fd(j+1)-mu_fd(j)) +
mu_fd(j);

mu_g     = (Tsat-T(j))/(T(j+1)-T(j)) * (mu_gd(j+1)-mu_gd(j)) +
mu_gd(j);

Cp_f     = (Tsat-T(j))/(T(j+1)-T(j)) * (Cp_fd(j+1)-Cp_fd(j)) +
Cp_fd(j);

Cp_g     = (Tsat-T(j))/(T(j+1)-T(j)) * (Cp_gd(j+1)-Cp_gd(j)) +
Cp_gd(j);

if Tsat <= 420

    Beta= (Tsat-T(j))/(T(j+1)-T(j)) * (beta_f(j+1)-beta_f(j)) +
beta_f(j);

else

    Beta= 0;

end

% Derived Properties

% Thermal Diffusivity, [m2/s]
alpha_f = k_f/rho_f/Cp_f;

alpha_g = k_g/rho_g/Cp_g;

% Kinematic Viscosity, [m2/s]
nu_f    = mu_f/rho_f;

nu_g    = mu_g/rho_g;

```

exp_profile.m

```
function [T]=exp_profile(Tmax,To,b,c,q,m)
```

```

%*****
%      [T]=exp_profile(Tmax,To,b,c,q,m)
% where,
%      Tmax = max surface temp of diaphragm, [deg C]
%      Td   = edge temp of diaphragm, [deg C]
%      b    = exposed shim radius, [m]
%      c    = shim thickness, [m]
%      q    = total heat rate, [W]
%      m    = length of r-vector in main program, so that T-vector matches
%
%      all inputs are scalars
%
%*****

k=140;                % Thermal Conductivity of brass shim, [W/m*K]

% Tmax=40;            % estimated vapor temp
% To=15.6;            % Measured temperature of shim edge, [degrees
C]
% b=0.755/2*25.4/1000; % Shim radius, [m]
% c=0.004*25.4/1000;  % Shim thickness, [m]
% q=20;               % Total Heat Rate, [W]
% m=100;              % length of r-vector, []

qdp=q./pi/b/c/2;     % Average Heat Flux through shim at edge, [W/m^2]

C=To-Tmax;
Q=-qdp/k;
n=Q*b/C;

dr=b/m;
r=0:dr:b;
T=C.*(r/b).^n+Tmax;

% figure(1)
% plot(r,T),grid
% title('Assumed exponential profile, (Td-Tatm)*(r/b)^n+Tatm')
% xlabel('radius, [m]')
% ylabel('Temp, [deg C]')

```

simpsons_rule.m

```

function [ans,err_order]=simpsons_rule(integrand,dx)
% [ans,err_order]=simpsons_rule(integrand,dx)
%
%      integrand = a vector of argument values for integral to be
evaluated
%      dx        = a scalar indicating the step size in the x-vector of
f(x)
%      ans       = a scalar indicating the approximate value of the
integral
%      err_order = a scalar indicating the order of magnitude of the error
%
%*****

```

```
n=(length(integrand)-1)/2;

for i=1:n
    A(i)=integrand(2*i);
end

for j=1:(n-1)
    B(j)=integrand(2*j-1);
end

ans=dx/3*(integrand(1)+4*sum(A)+2*sum(B)+integrand(2*n+1));

err_order=n*dx^5/90;
```

APPENDIX B

TOTAL HEAT RATE TABLES

The theoretical analysis of this investigation consisted of the following:

1. An assumed radial temperature profile for the circular brass shim used as the condensing surface
2. A theoretical estimation of the radial HF distribution, based on the Rose theory (Eq. 2-10)
3. Surface integration of the estimated radial HF distribution

The third step gave an estimate of the total overall HT rate, or THR, for the given experimental setup and conditions. Calculation of this quantity was for a given set of experimental conditions was time consuming. However, the function was very close to linear in the two main control parameters, edge temperature (T_o) and saturation temperature (T_{sat}). This linearity was used to dramatically cut down on processor demands by constructing tables of references values. Linear interpolation between the table values was then used to estimate the THR values from actual experimental conditions (Table B-1 to 8).

Chapter 7 discussed the uncertainty added from this estimation process, which was generally the same order of magnitude as that of the measured value. These tables were included in the MATLAB program `Heat_Rate_Archive.m` (Appendix A).

Table B-1. Theoretical THR with Theoretical Maximum Departing Droplet Size.

$r_{\max} =$		$T_o, ^\circ\text{F}$				
Saturation Temperature, $T_{\text{sat}}, ^\circ\text{F}$	Theory (Eq. 2-11)	4	8	12	16	20
	24	40.19	31.91	23.67	15.51	7.48
	26	45.86	37.27	28.72	20.23	11.84
	28	51.78	42.89	34.03	25.23	16.51
	30	57.97	48.77	39.61	30.51	21.47
	32	64.71	55.17	45.67	36.22	26.83
	34	71.40	61.57	51.78	42.04	32.35
	36	78.67	68.51	58.40	48.32	38.30
	38	86.16	75.69	65.26	54.86	44.51
	40	93.93	83.15	72.40	61.68	51.02
	42	102.34	91.21	80.10	69.03	58.01
	44	110.63	99.18	87.77	76.40	65.07
	46	119.60	107.81	96.06	84.34	72.66
	48	128.78	116.66	104.57	92.52	80.50
	50	138.23	125.78	113.36	100.98	88.63

Table B-2. Theoretical THR with 4 mm Maximum Departing Droplet Size.

$r_{\max} =$		$T_o, ^\circ\text{F}$				
Saturation Temperature, $T_{\text{sat}}, ^\circ\text{F}$	4 mm	4	8	12	16	20
	24	32.11	25.49	18.92	12.40	5.98
	26	36.64	29.77	22.94	16.16	9.46
	28	41.36	34.26	27.18	20.15	13.19
	30	46.30	38.96	31.64	24.37	17.15
	32	51.68	44.06	36.47	28.92	21.43
	34	57.01	49.17	41.35	33.57	25.83
	36	62.81	54.70	46.62	38.58	30.58
	38	68.78	60.43	52.09	43.79	35.53
	40	74.98	66.37	57.79	49.23	40.72
	42	81.68	72.79	63.93	55.09	46.30
	44	88.27	79.14	70.04	60.96	51.92
	46	95.41	86.01	76.63	67.28	57.97
	48	102.72	93.05	83.41	73.80	64.21
	50	110.24	100.31	90.41	80.53	70.68

Table B-3. Theoretical THR with 2 mm Maximum Departing Droplet Size.

	$r_{\max} =$	$T_o, ^\circ\text{F}$				
	2 mm	4	8	12	16	20
Saturation Temperature, $T_{\text{sat}}, ^\circ\text{F}$	24	36.20	28.74	21.32	13.97	6.74
	26	41.29	33.56	25.86	18.22	10.67
	28	46.61	38.60	30.63	22.71	14.86
	30	52.17	43.89	35.65	27.46	19.32
	32	58.22	49.64	41.09	32.59	24.14
	34	64.22	55.38	46.58	37.81	29.10
	36	70.74	61.61	52.51	43.45	34.44
	38	77.46	68.05	58.67	49.32	40.02
	40	84.43	74.74	65.07	55.44	45.85
	42	91.97	81.96	71.98	62.03	52.13
	44	99.38	89.10	78.85	68.63	58.45
	46	107.41	96.82	86.27	75.74	65.25
	48	115.62	104.74	93.89	83.06	72.28
	50	124.07	112.90	101.75	90.63	79.55

Table B-4. Theoretical THR with 1 mm Maximum Departing Droplet Size.

	$r_{\max} =$	$T_o, ^\circ\text{F}$				
	1 mm	4	8	12	16	20
Saturation Temperature, $T_{\text{sat}}, ^\circ\text{F}$	24	40.76	32.36	24.01	15.73	7.59
	26	46.50	37.79	29.12	20.51	12.01
	28	52.48	43.46	34.49	25.57	16.73
	30	58.74	49.42	40.14	30.91	21.75
	32	65.54	55.88	46.26	36.68	27.17
	34	72.29	62.34	52.43	42.56	32.75
	36	79.62	69.34	59.10	48.90	38.76
	38	87.18	76.58	66.02	55.50	45.03
	40	95.00	84.10	73.22	62.39	51.60
	42	103.47	92.21	80.99	69.79	58.65
	44	111.81	100.24	88.71	77.22	65.76
	46	120.83	108.92	97.04	85.20	73.41
	48	130.06	117.82	105.61	93.43	81.30
	50	139.55	126.99	114.45	101.94	89.48

Table B-5. Theoretical THR with 0.5 mm Maximum Departing Droplet Size.

	$r_{\max} =$		$T_o, ^\circ\text{F}$			
	0.5 mm	4	8	12	16	20
Saturation Temperature, $T_{\text{sat}}, ^\circ\text{F}$	24	45.86	36.41	27.01	17.70	8.54
	26	52.30	42.50	32.75	23.07	13.51
	28	59.03	48.89	38.79	28.76	18.82
	30	66.06	55.58	45.14	34.76	24.46
	32	73.71	62.84	52.02	41.25	30.56
	34	81.29	70.10	58.96	47.86	36.83
	36	89.53	77.97	66.46	54.99	43.58
	38	98.02	86.11	74.24	62.41	50.64
	40	106.82	94.55	82.32	70.14	58.01
	42	116.33	103.67	91.05	78.47	65.94
	44	125.69	112.69	99.73	86.80	73.93
	46	135.83	122.44	109.09	95.78	82.52
	48	146.19	132.44	118.71	105.03	91.39
	50	156.86	142.73	128.64	114.58	100.57

Table B-6. Theoretical THR with 0.25 mm Maximum Departing Droplet Size.

	$r_{\max} =$		$T_o, ^\circ\text{F}$			
	0.25 mm	4	8	12	16	20
Saturation Temperature, $T_{\text{sat}}, ^\circ\text{F}$	24	51.51	40.89	30.34	19.88	9.59
	26	58.75	47.74	36.79	25.91	15.17
	28	66.31	54.91	43.57	32.30	21.14
	30	74.21	62.43	50.70	39.04	27.48
	32	82.79	70.59	58.43	46.33	34.32
	34	91.31	78.74	66.22	53.76	41.37
	36	100.56	87.58	74.65	61.76	48.95
	38	110.10	96.72	83.38	70.10	56.87
	40	119.98	106.20	92.47	78.78	65.16
	42	130.66	116.44	102.26	88.13	74.05
	44	141.17	126.57	112.01	97.49	83.03
	46	152.55	137.52	122.52	107.57	92.67
	48	164.19	148.74	133.32	117.95	102.63
	50	176.16	160.30	144.47	128.68	112.95

Table B-7. Theoretical THR with 0.1 mm Maximum Departing Droplet Size.

	$r_{\max} =$		$T_o, ^\circ\text{F}$			
	0.1 mm	4	8	12	16	20
Saturation Temperature, $T_{\text{sat}}, ^\circ\text{F}$	24	59.89	47.54	35.26	23.10	11.14
	26	68.32	55.51	42.77	30.12	17.63
	28	77.12	63.86	50.67	37.56	24.57
	30	86.31	72.61	58.97	45.41	31.95
	32	96.31	82.11	67.97	53.89	39.91
	34	106.23	91.61	77.04	62.53	48.12
	36	117.00	101.90	86.84	71.85	56.94
	38	128.11	112.54	97.02	81.55	66.17
	40	139.61	123.58	107.59	91.66	75.81
	42	152.06	135.50	119.00	102.55	86.17
	44	164.29	147.30	130.35	113.45	96.62
	46	177.54	160.04	142.59	125.18	107.84
	48	191.10	173.11	155.16	137.27	119.44
	50	205.03	186.57	168.14	149.77	131.45

Table B-8. Theoretical THR with 0.01 mm Maximum Departing Droplet Size.

	$r_{\max} =$		$T_o, ^\circ\text{F}$			
	0.01 mm	4	8	12	16	20
Saturation Temperature, $T_{\text{sat}}, ^\circ\text{F}$	24	84.58	67.09	49.72	32.52	15.62
	26	96.73	78.55	60.47	42.54	24.84
	28	109.42	90.56	71.80	53.17	34.74
	30	122.69	103.17	83.74	64.43	45.28
	32	137.17	116.90	96.72	76.64	56.71
	34	151.52	130.62	109.80	89.08	68.49
	36	167.14	145.52	123.98	102.53	81.20
	38	183.25	160.94	138.70	116.54	94.51
	40	199.95	176.95	154.02	131.17	108.43
	42	218.05	194.27	170.57	146.95	123.43
	44	235.83	211.39	187.03	162.74	138.55
	46	255.11	229.92	204.81	179.77	154.82
	48	274.83	248.92	223.08	197.32	171.64
	50	295.13	268.50	241.94	215.46	189.07

APPENDIX C DETAIL DRAWINGS

The main, aluminum pressure vessel cylinder was originally produced for a different study. The rest of the pressure vessel components were manufactured in-house to mate with the available vessel body. Detail drawings for these components follow in this section.

The Cooler did not have a detail drawing included in this appendix. This component centered around a hollow copper cylinder, called the Cooler Barrel. A jacket was then made from two discs of copper and an outer tube. These components were then soldered together. Grooves were machined on the cylinder to aid the soldering. Two holes of appropriate diameter were drilled in opposite ends of the outer tube wall to accommodate the coolant tubes. The nylon coolant tubes were then attached to the Cooler with Copper Bond epoxy.

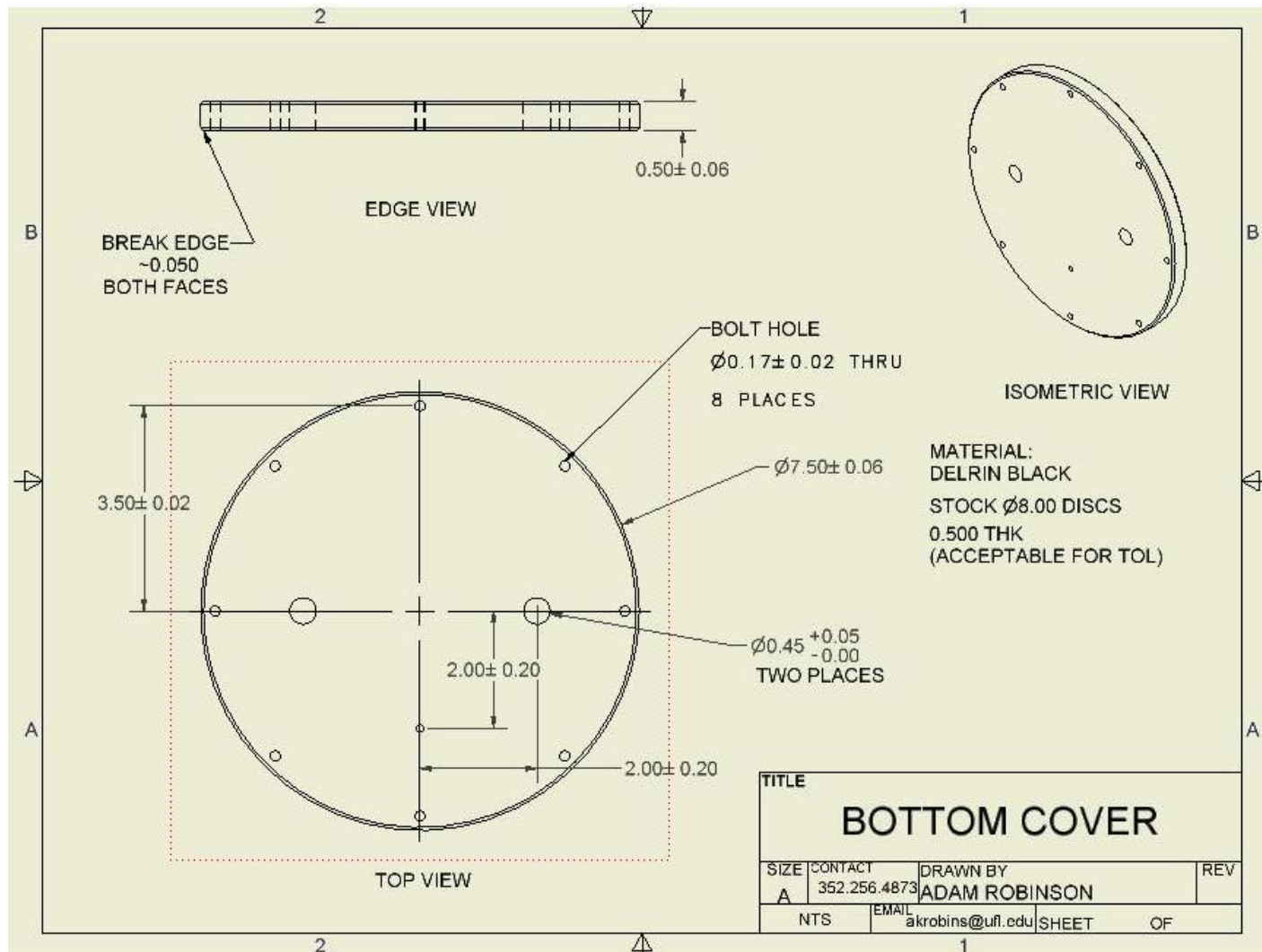


Figure C-1. Bottom Cover detail drawing.

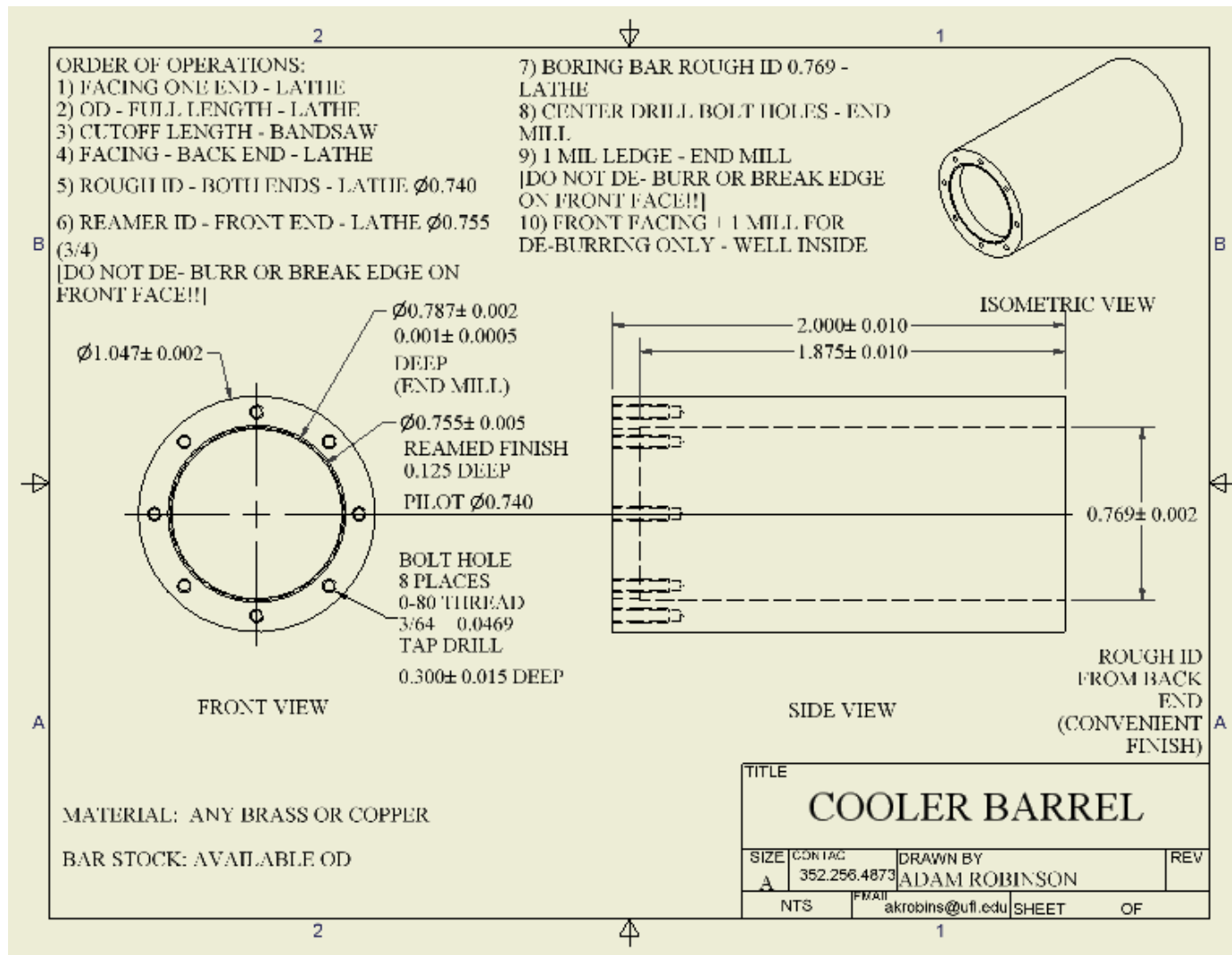


Figure C-2. Cooler Barrel detail drawing.

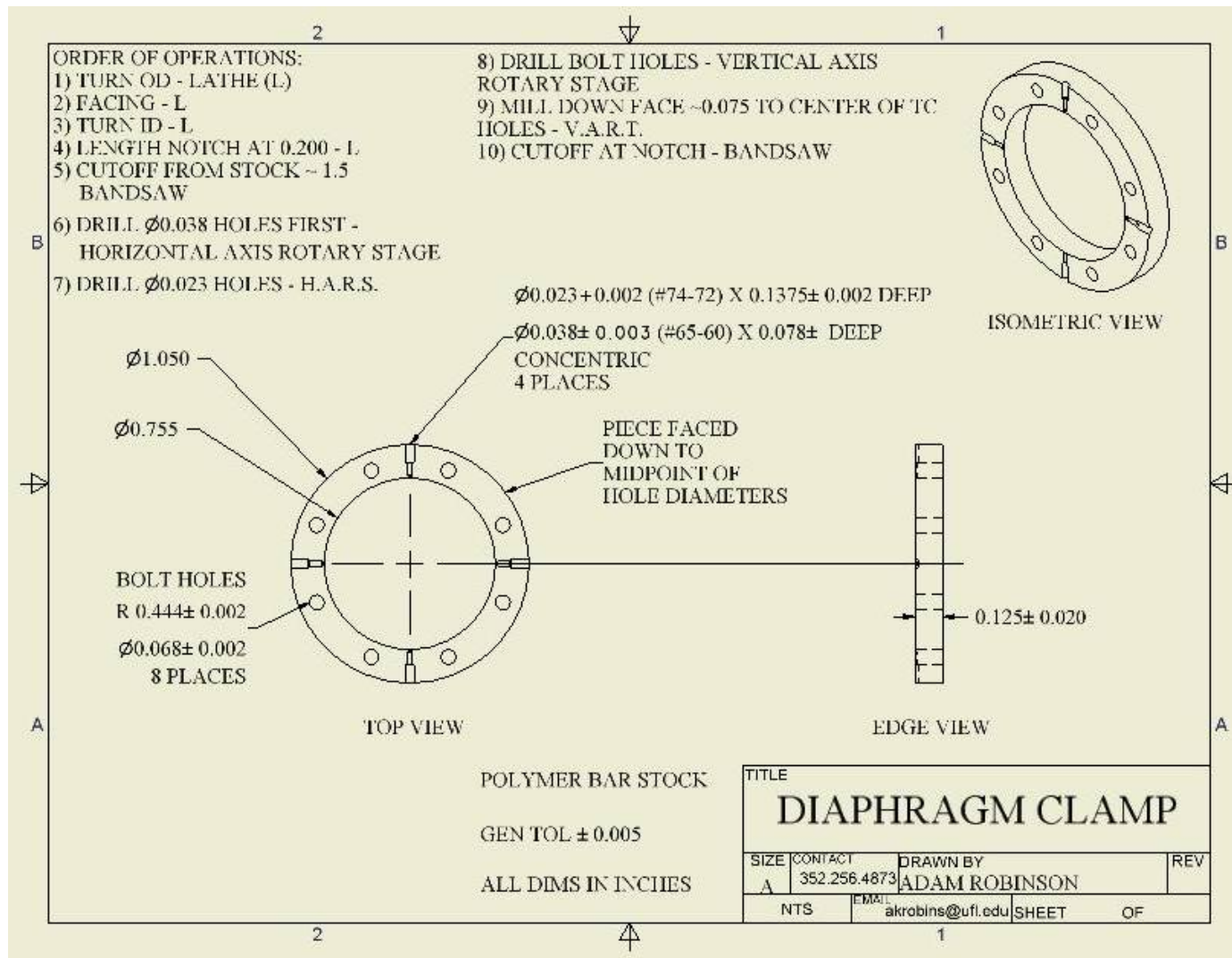


Figure C-3. Diaphragm Clamp detail drawing.

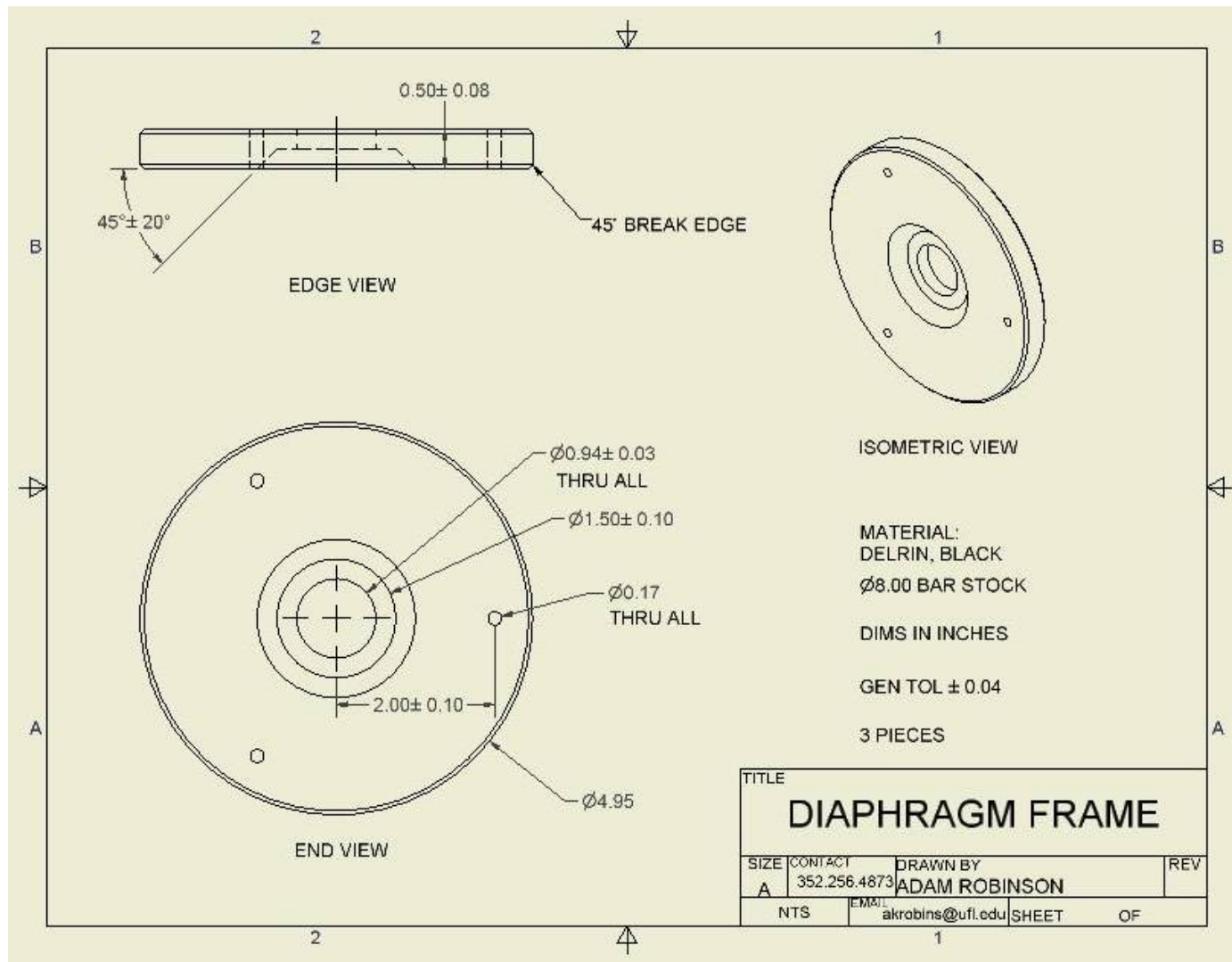


Figure C-4. Diaphragm Frame detail drawing.

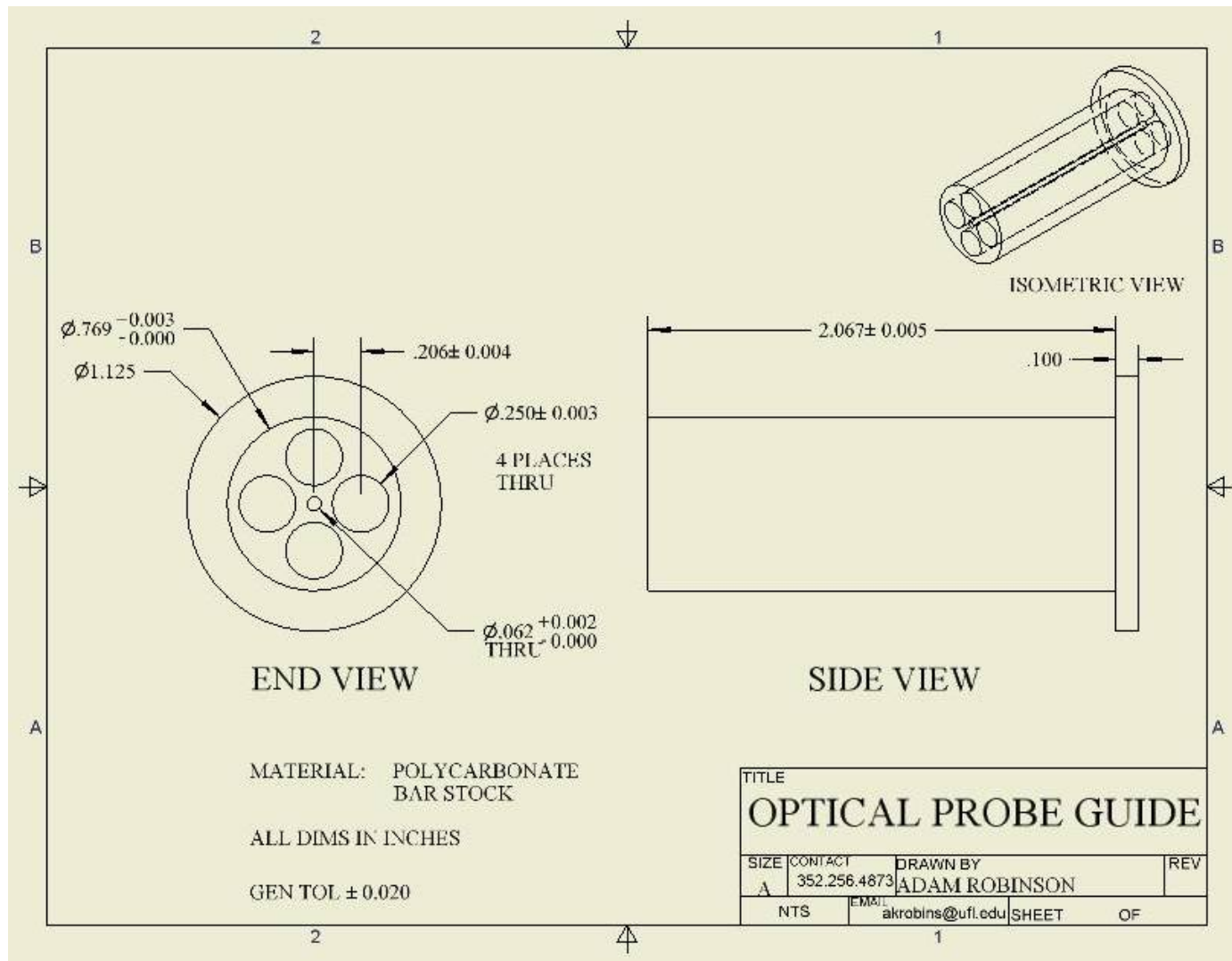


Figure C-5. Optical Probe Guide detail drawing.

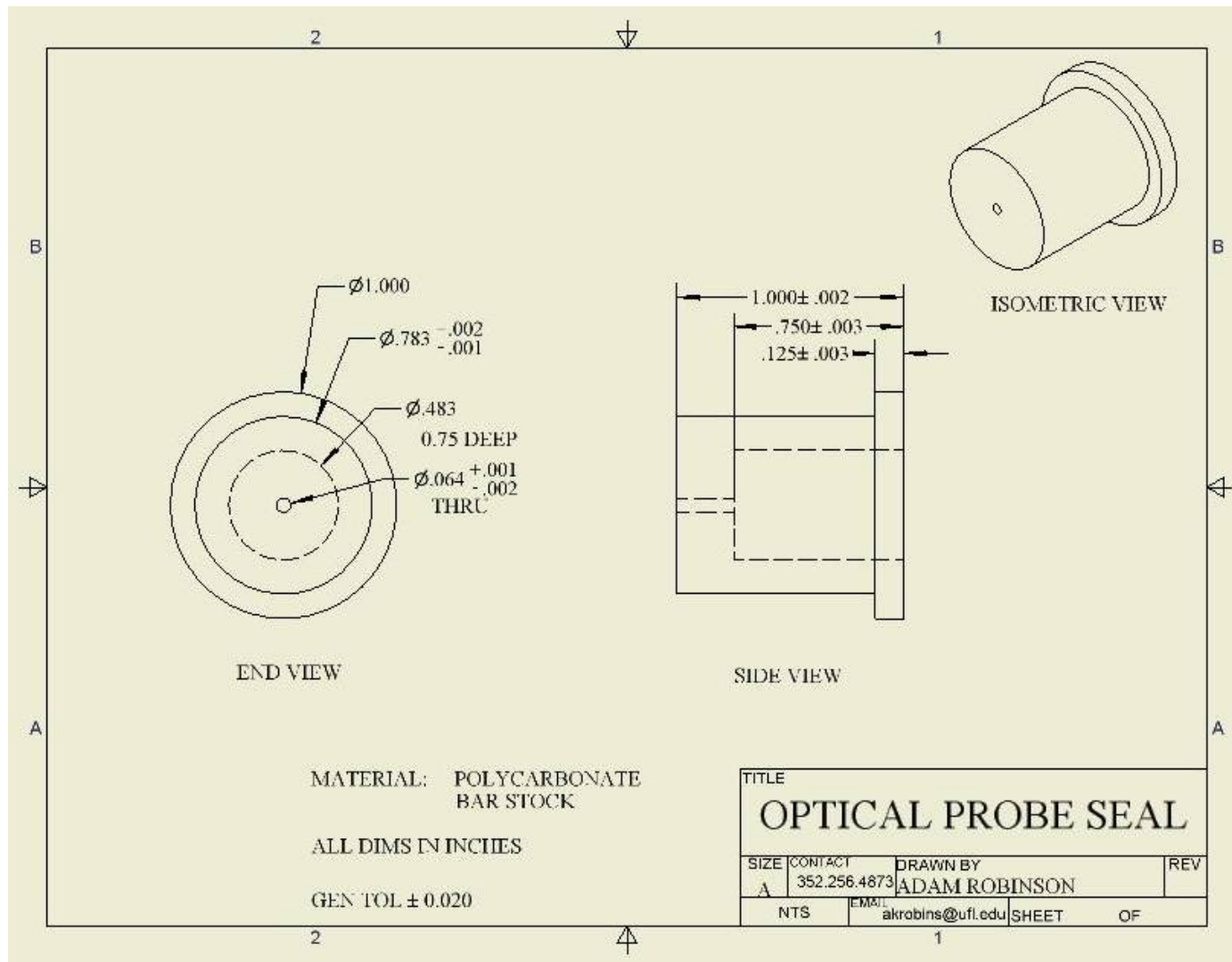


Figure C-6. Optical Probe Seal detail drawing.

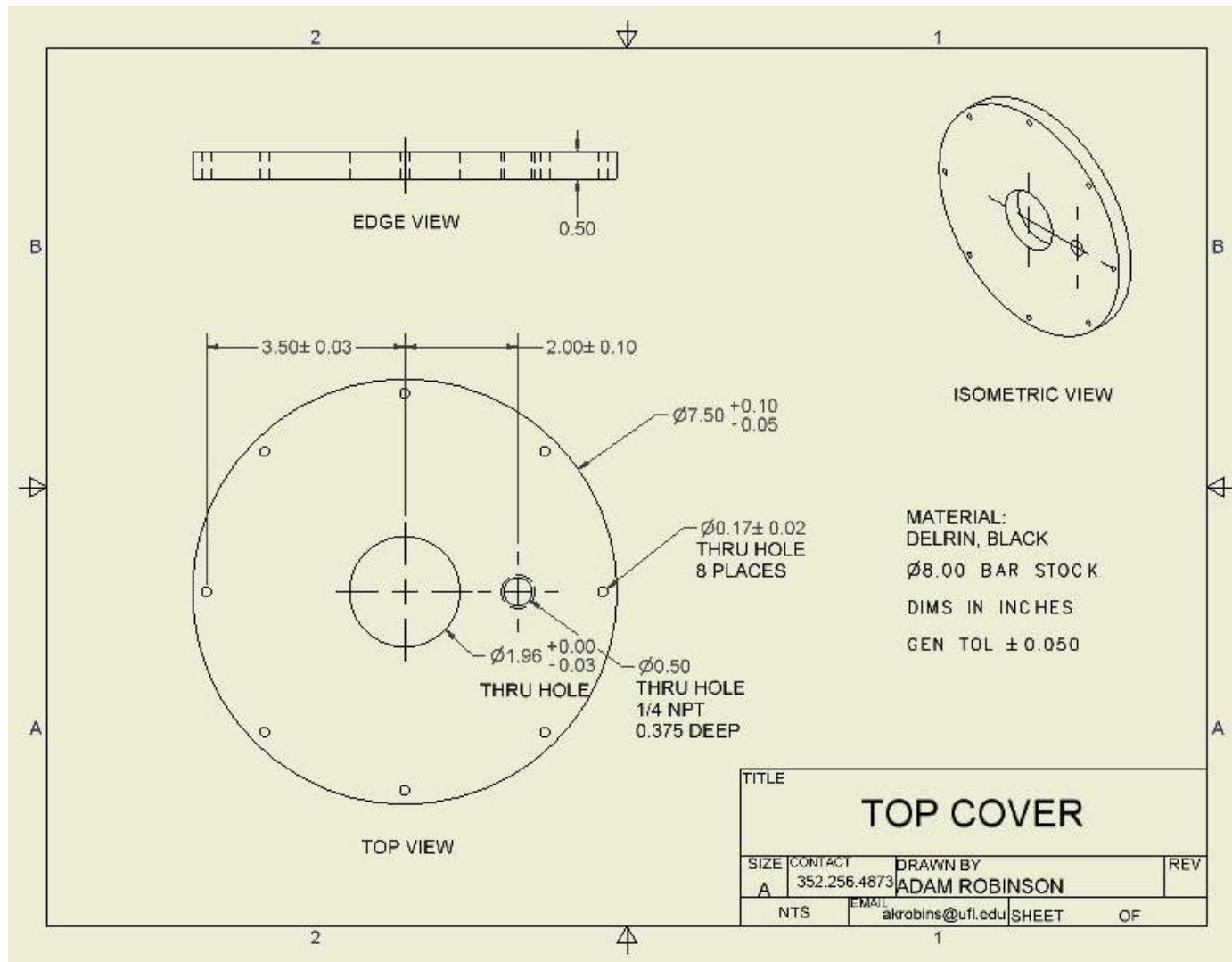


Figure C-7. Top Cover detail drawing.

LIST OF REFERENCES

- [1] SIA, Semiconductor Industry Association, International technology road map, Assembly and Packaging Section, Technology Requirements (2001) 4–8.
- [2] I. Mudawar, Assessment of high-heat-flux thermal management schemes, *IEEE Transactions on Components & Packaging Technologies* 24 (2001) 122–142.
- [3] M.M. François, W. Shyy, J.N. Chung, A micro-scale membrane-actuated condenser/evaporator for enhanced thermal management, *ASME Heat Transfer Division, International Mechanical Congress and Exposition, HDT, Orlando, FL, November (2000) 366-372.*
- [4] M.M. François, W. Shyy, Computations of drop dynamics with heat transfer, Doctoral Thesis, University of Florida, Department of Mechanical Engineering, Gainesville, FL (2002).
- [5] M. Friedman, J.N. Chung, Feasibility study on a piezoelectric droplet ejector, unpublished paper, University of Florida Department of Mechanical and Aerospace Engineering, Gainesville, FL, November (2001).
- [6] G. Perçin, L. Levin, B.T. Khuri-Yakub, Piezoelectrically actuated droplet ejector, *Review of Scientific Instruments* 68 (1997) 4561–4563.
- [7] X. Zhu, E.S. Kim, Microfluidic motion generation with acoustic waves, *Sensors and Actuators A* 66 (1998) 355–360.
- [8] D. Huang, E.S. Kim, Micromachined acoustic-wave liquid ejector, *Journal of Microelectromechanical Systems* 10 (2001) 442–449.
- [9] N. Szita, R. Sutter, J. Dual, R.A. Buser, A micropipettor with integrated sensors, *Sensors and Actuators A* 89 (2001) 112–118.
- [10] B. Vukasinovic, A. Glezer, Vibration-induced droplet atomization, Doctoral Thesis, Georgia Technical University, Department of Mechanical Engineering, Atlanta, GA, March (2002).
- [11] F.P. Incropera, D.P. DeWitt, Fundamentals of heat and mass transfer, Fourth Edition, John Wiley & Sons, New York (1996) 238-239.
- [12] J.W. Rose, Some aspects of condensation heat transfer theory, *International Communications in Heat and Mass Transfer* 15 (1988) 449–473.

- [13] E.J. Le Fevre, J.W. Rose, Heat-transfer measurements during dropwise condensation of steam, *International Journal of Heat and Mass Transfer* 7 (1964) 272–273.
- [14] G. Koch, K. Kraft, A. Leipertz, Parameter study on the performance of dropwise condensation, *Revue Générale de Thermique* 37 (1998) 539–548.
- [15] C. Yamali, H. Merte Jr., Influence of sweeping on dropwise condensation with varying body force and surface subcooling, *International Journal of Heat and Mass Transfer* 42 (1999) 2943–2953.
- [16] C. Yamali, H. Merte Jr., A theory of dropwise condensation at large subcooling including the effect of the sweeping, *Heat and Mass Transfer* 38 (2002) 191–202.
- [17] E.J. Le Fevre, J.W. Rose, A theory of heat transfer by dropwise condensation, *Proceedings of the 3rd International Heat Transfer Conference*, American Institute of Chemical Engineers, New York, NY 2 (1966) 362.
- [18] J.W. Rose, Dropwise condensation theory and experiment: a review, *Proceedings of the Institution of Mechanical Engineers, Part A (Journal of Power and Energy)* 216 A2 (2002) 115–128.
- [19] J.W. Rose, L.R. Glicksman, Dropwise condensation – The distribution of drop sizes, *International Journal of Heat and Mass Transfer* 16 (1973) 411–425.
- [20] J.W. Rose, Surface tension effects and enhancement of condensation heat transfer, *Chemical Engineering Research and Design* 82 A4 (2004) 419–429.
- [21] S.A. Stylianou, J.W. Rose, Dropwise condensation on surfaces having different thermal conductivities, *Transactions of the ASME. Journal of Heat Transfer* 102 (1980) 477–482.
- [22] S.A. Stylianou, J.W. Rose, Drop-to-filmwise condensation transition: Heat transfer measurements for ethanediol, *International Journal of Heat and Mass Transfer* 26 (1983) 747–760.
- [23] J.W. Rose, Dropwise condensation theory, *International Journal of Heat and Mass Transfer* 24 (1981) 191–194.
- [24] J.W. Rose, Condensation heat transfer fundamentals, *Chemical Engineering Research and Design* 76 A2 (1998) 143–152.
- [25] E. Citakoglu, J.W. Rose, Dropwise condensation – the effect of surface inclination, *International Journal of Heat and Mass Transfer* 12 (1969) 645–650.
- [26] I. Tanasawa, Y. Funawatashi, J. Ochiai, Experimental study on dropwise condensation-effect of maximum drop size upon the heat transfer coefficient, *Sixth International Heat Transfer Conference* (1978) 477–482.

- [27] I. Tanasawa, Y. Utaka, Measurement of condensation curves for dropwise condensation of steam at atmospheric pressure, *Transactions of the ASME Journal of Heat Transfer* 105 (1983) 633–638.
- [28] H. Tanaka, T. Tsuruta, A microscopic study of dropwise condensation, *International Journal of Heat and Mass Transfer* 27 (1984) 327–335.
- [29] B.B. Mikic, On mechanism of dropwise condensation, *International Journal of Heat and Mass Transfer* 12 (1969) 1311–1323.
- [30] D. Subba Rao, M.S. Murthy, Heat transfer during dropwise condensation, *Chemical Engineering Journal* 26 (1983) 1–12.
- [31] E.J. Le Fevre, J.W. Rose, An experimental study of heat transfer by dropwise condensation, *International Journal of Heat and Mass Transfer* 8 (1965) 1117–1133.
- [32] E. Citakoglu, J.W. Rose, Dropwise condensation – some factors influencing the validity of heat-transfer measurements, *International Journal of Heat and Mass Transfer* 11 (1968) 523–537.
- [33] T. Tsuruta, H. Tanaka, A theoretical study on the constriction resistance in dropwise condensation, *International Journal of Heat and Mass Transfer* 34 (1991) 2779–2786.
- [34] T. Tsuruta, H. Tanaka, S. Togashi, Experimental verification of constriction resistance theory in dropwise condensation heat transfer, *International Journal of Heat and Mass Transfer* 34 (1991) 2787–2796.
- [35] S. Hatamiya, H. Tanaka, Dropwise condensation of steam at low pressures, *International Journal of Heat and Mass Transfer* 30 (1987) 497–507.
- [36] Y. Song, D. Xu, J. Lin, S. Tsian, A study on the mechanism of dropwise condensation, *International Journal of Heat and Mass Transfer* 34 (1991) 2827–2831.
- [37] A.S. Gavrish, V.G. Rifert, A.I. Sardak, V.L. Podbereznyy, A new dropwise condensation promoter for desalination and power plants, *Heat Transfer Research* 25 (1993) 82–86.
- [38] L.R. Glicksman, A.W. Hunt, Jr., Numerical simulation of dropwise condensation, *International Journal of Heat and Mass Transfer* 15 (1972) 2251–2269.
- [39] B.M. Burnside, H.A. Hadi, Digital computer simulation of dropwise condensation from equilibrium droplet to detectable size, *International Journal of Heat and Mass Transfer* 42 (1999) 3137–3146.

- [40] Y.T. Wu, C.X. Yang, X.G. Yuan, A theoretical study of the effect of surface thermal conductivity on heat transfer coefficient in dropwise condensation, *Numerical Heat Transfer, Part A (Applications)* 40 (2001) 169–179.
- [41] N. Maiti, U.B. Desai, A.K. Ray, Application of mathematical morphology in measurement of droplet size distribution in dropwise condensation, *Thin Solid Films* 376 (2000) 16–25.
- [42] Y.T. Wu, C.X. Yang, X.G. Yuan, Drop distributions and numerical simulation of dropwise condensation heat transfer, *International Journal of Heat and Mass Transfer* 44 (2001) 4455–4464.
- [43] P. Griffith, M.S. Lee, The effect of surface thermal properties and finish on dropwise condensation, *International Journal of Heat and Mass Transfer* 10 (1967) 697–707.
- [44] J.W. Rose, Further aspects of dropwise condensation theory, *International Journal of Heat and Mass Transfer* 19 (1976) 1363–1370.
- [45] J.W. Rose, Condensation heat transfer, *Heat Mass Transfer* 35 (1999) 479–485.
- [46] J.W. Rose, Heat-transfer coefficients, Wilson plots and accuracy of thermal measurements, *Experimental Thermal and Fluid Science* 28 (2004) 77–86.
- [47] Y. Utaka, A. Saito, T. Tani, H. Shibuya, K. Katayama, Study on dropwise condensation curves (measurement of propylene glycol vapor on PTFE coated surfaces), *Bulletin Japan Society Mechanical Engineers* 28 (1985) 1150–1157.
- [48] J.J. Lorenz, B.B. Mikic, The effect of thermocapillary flow on heat transfer in dropwise condensation, *Transactions of the ASME. Series C, Journal of Heat Transfer* 92 (1970) 46–52.
- [49] M. Abu-Orabi, Modeling of heat transfer in dropwise condensation, *International Journal of Heat and Mass Transfer* 41(1998) 81–87.
- [50] D.W. Tanner, C.J. Potter, D. Pope, D. West, Heat transfer in dropwise condensation – part II surface chemistry, *International Journal of Heat and Mass Transfer* 8 (1965) 427–428.
- [51] A.F. Mills, R.A. Seban, The condensation coefficient of water, *International Journal of Heat and Mass Transfer* 10 (1967) 1815–1827.
- [52] J. Niknejad, J.W. Rose, Interphase matter transfer: an experimental study of condensation of mercury, *Proceedings of the Royal Society of London, Series A (Mathematical and Physical Sciences)* 378 (1981) 305–327.

- [53] J.W. Rose, On Interphase Matter Transfer, the Condensation Coefficient and Dropwise Condensation, *Proceedings of the Royal Society of London. Series A, Mathematical and Physical Sciences* 411 (1987) 305–311.
- [54] D.W. Tanner, C.J. Potter, D. Pope, D. West, Heat transfer in dropwise condensation – Part I The effects of heat flux, steam velocity and non-condensable gas concentration, *International Journal of Heat and Mass Transfer* 8 (1965) 419–420.
- [55] D.W. Tanner, D. Pope, C.J. Potter, D. West, Heat transfer in dropwise condensation at low steam pressures in the absence and presence of non-condensable gas, *International Journal of Heat and Mass Transfer* 11 (1968) 181–182.
- [56] S. Necmi, J.W. Rose, Heat-transfer measurements during dropwise condensation of mercury, *International Journal of Heat and Mass Transfer* 20 (1977) 877–881.
- [57] V.N. Bochagov, A.R. Dorokhov, Dropwise condensation on a polymer surface, *Heat Transfer - Soviet Research* 15 (1983) 73–80.
- [58] Q. Zhao, D. Zhang, J.F. Lin, Surface materials with dropwise condensation made by ion implantation technology, *International Journal of Heat and Mass Transfer* 34 (1991) 2833–2835.
- [59] Q. Zhao, G.M. Wang, D.C. Zhang, J.F. Lin, Dropwise condensation on L-B film surface, *Chemical Engineering Processing* 35 (1996) 473–477.
- [60] J.W. Rose, B.B. Mikic, R. Hannemann, The effect of surface thermal conductivity on dropwise condensation heat transfer, *International Journal of Heat and Mass Transfer* 21 (1978) 80–82.
- [61] R.J. Hannemann, B.B. Mikic, An experimental investigation into the effect of surface thermal conductivity on the rate of heat transfer in dropwise condensation, *International Journal of Heat and Mass Transfer* 19 (1976) 1308–1317.
- [62] R.J. Hannemann, B.B. Mikic, An analysis of the effect of surface thermal conductivity on the rate of heat transfer in dropwise condensation, *International Journal of Heat and Mass Transfer* 19 (1976) 1299–1307.
- [63] S.S. Finnicum, J.W. Westwater, Dropwise vs filmwise condensation of steam on chromium, *International Journal of Heat and Mass Transfer* 32 (1989) 1541–1549.
- [64] Y.L. Lee, The wettability of solid surfaces modified by vacuum deposition of stearic acid, *Colloids and Surfaces A: Physicochemical and Engineering Aspects* 155 (1999) 221–229.
- [65] G. Pang, J.D. Dale, D.Y. Kwok, An integrated study of dropwise condensation heat transfer on self-assembled organic surfaces through Fourier transform infra-red spectroscopy and ellipsometry, *International Journal of Heat and Mass Transfer* 48 (2005) 307–316.

- [66] K.J. Kim, A.M. Lefsafer, A. Razani, A. Stone, The effective use of heat transfer additives for steam condensation, *Applied Thermal Engineering* 21 (2001) 1863–1874.
- [67] G.A. O'Neill, J.W. Westwater, Dropwise condensation of steam on electroplated silver surfaces, *International Journal of Heat and Mass Transfer* 27 (1984) 1539–1549.
- [68] M. Izumi, S. Kumagai, R. Shimada, N. Yamakawa, Heat transfer enhancement of dropwise condensation on a vertical surface with round shaped grooves, *Exp. Thermal and Fluid Science* 28 (2004) 243–248.
- [69] X.H. Ma, B.X. Wang, D.Q. Xu, J.F. Lin, Lifetime test of dropwise condensation on polymer-coated surfaces, *Heat Transfer – Asian Research* 28 (1999) 551–558.
- [70] C. Ma, J. Chen, D. Xu, J. Lin, C. Ren, Z. Long, Influence of processing conditions of polymer film on dropwise condensation heat transfer, *International Journal of Heat and Mass Transfer* 45 (2002) 3405–3411.
- [71] X. Ma, J.W. Rose, D. Xu, J. Lin, B. Wang, Advances in dropwise condensation heat transfer: Chinese research, *Chemical Engineering Journal* 78 (2000) 87–93.
- [72] Q. Zhao, B.M. Burnside, Dropwise condensation of steam on ion implanted condenser surfaces, *Heat Recovery Systems and CHP* 14 (1994) 525–534.
- [73] S.B. Al-Shammari, D.R. Webb, P. Heggs, Condensation of steam with and without the presence of non-condensable gases in a vertical tube, *Desalination* 169 (2004) 151–160.
- [74] D.G. Kroger, W.M. Rohsenow, Condensation heat transfer in the presence of a non-condensable gas, *International Journal of Heat and Mass Transfer* 11 (1968) 15–26.
- [75] C.Y. Wang, C.J. Tu, Effects of non-condensable gas on laminar film condensation in a vertical tube, *International Journal of Heat and Mass Transfer* 31 (1988) 2339–2345.
- [76] R. Semiat, Y. Galperin, Effect of non-condensable gases on heat transfer in the tower MED seawater desalination plant, *Desalination* 140 (2001) 27–46.
- [77] W. Chaoyang, T. Chuanjing, The effect of non-condensable gas on forced convection condensation along a horizontal plate in a porous medium, *International Journal of Heat and Mass Transfer* 32 (1989) 1847–1852.
- [78] A. Tamir, Y. Taitel, Condensation of steam in a channel flow in the presence of noncondensable gases with surface resistance, *Desalination* 8 (1970) 293–306.
- [79] M.K. Zhong, K. Mizukami, Effect of non-condensable gas on condensation in a highly-rotating drum with a scraper, *Heat Mass Transfer* 34 (1998) 19–25.

- [80] J.C. Dent, Effect of vibration on condensation heat transfer to a horizontal tube, Proceedings of the Institute of Mechanical Engineering 184 Part 1 (1969) 99–105.
- [81] J.C. Dent, The calculation of heat transfer coefficient for condensation of steam on a vibrating vertical tube, International Journal of Heat and Mass Transfer 12 (1969) 991–996.
- [82] Yu.M. Brodov, R.Z. Savel'yev, V.A. Permyakov, V.K. Kuptsov, A.G. Gal'perin, The effect of vibration on heat transfer and flow of condensing steam on a single tube, Heat Transfer – Soviet Research 9 (1977) 152–156.
- [83] R.Z. Savel'yev, Yu.M. Brodov, L.G. Gal'perin, M.A. Nirenshteyn, A.Y. Ryabchikov, Heat transfer and flow in condensation on vibrating tubes, Heat Transfer - Soviet Research 12 (1980) 1–2.
- [84] K. Nishiyama, A. Murata, T. Kajikawa, The study of condensation heat transfer performance due to periodic motion of a vertical tube, Heat Transfer – Japanese Research 15 (1986) 32–43.
- [85] K. Nishiyama, Study of heat transfer performance of a periodic moving condenser, Heat Transfer – Japanese Research 17 (1988) 32–42.
- [86] Y.K. Oh, S.H. Park, Y.I. Cho, A study of the effect of ultrasonic vibrations on phase-change heat transfer, International Journal of Heat and Mass Transfer 45 (2002) 4631–4641.
- [87] H.Y. Kim, Y.G. Kim, B.H. Kang, Enhancement of natural convection and pool boiling heat transfer via ultrasonic vibration, International Journal of Heat and Mass Transfer 47 (2004) 2831–2840.
- [88] H. Shiraiwa, T. Hosokawa, T. Nakata, K. Itoh, Heat transfer characteristics on a horizontal(ly) vibrating plate under dropwise condensation, 5th International Conference on Multiphase Flow, Yokohama, Japan, May 30 – June 4 (2004) paper No. 283.
- [89] S.N. Heffington, W.Z. Black, A. Glezer, Vibration-induced droplet atomization heat transfer cell for high-heat flux dissipation, Doctoral Thesis, Georgia Institute of Technology, Department of Mechanical Engineering, Atlanta, December (2000).
- [90] S.N. Heffington, W.Z. Black, A. Glezer, Vibration-induced droplet atomization heat transfer cell for high-heat flux dissipation, Eighth Intersociety Conference on Thermal and Thermomechanical Phenomena in Electronic Systems (2002) 408–412.
- [91] C. Xia, Spray/jet cooling for heat flux high to 1 kW/cm^2 , 18th IEEE SEMI-THERM Symposium, San Jose, CA (2002) 159–163.

- [92] H. Shaukatullah, A. Claassen, Effect of thermocouple wire size and attachment method of measurement of thermal characteristics of electronic packages, 19th IEEE SEMI-THERM Symposium, San Jose, CA (2003) 97-105

BIOGRAPHICAL SKETCH

Adam Robinson was born in Wichita, KS on January 27, 1979. He received his Bachelors of Science in Mechanical Engineering from the University of Florida in May of 2002. He plans to focus his career on renewable energy development in the developed and the developing world.